Gravitational Lensing Studies of Galaxy Cluster Halos

Stefan Rau

München 2013

Gravitational Lensing Studies of Galaxy Cluster Halos

Stefan Rau

Dissertation
an der Fakultät für Physik
der Ludwig–Maximilians–Universität
München

vorgelegt von
Stefan Rau
aus Nürtingen

München, den 25. November 2013

Erstgutachter: Prof. Dr. Simon D. M. White
Zweitgutachter: Prof. Dr. Joseph Mohr
Tag der mündlichen Prüfung: 11. April 2014

Contents

List of Figures

Zusammenfassung

Um das derzeitige Standardmodell der Kosmologie, das ΛCDM-Modell auf die Probe zu stellen, ist es wichtig Vergleiche zwischen beobachteten Galaxien und Galaxienhaufen und den Vorhersagen numerischer Computermodelle von der Entwicklung des Universums und der Strukturbildung zu ziehen. In dieser Arbeit erstellen wir daher hochauflösende Simulationen des Gravitationslinseneffekts. Bei den Berechnungen dafür werden Bündel von Lichtstrahlen durch die Massendichteverteilung numerischer Vielteilchen-Simulationen geschickt. Will man nun den Einfluss kleinster Massestrukturen auf den Gravitationslinseneffekt untersuchen, so stellt man fest, dass die Auflösung der N-Körper Simulation einen limitierenden Faktor darstellt. Auf Grund der begrenzten Teilchenzahl in den N-Körper Simulationen, ahmen Schwankungen in der lokalen Anzahl der Teilchen den Effekt kleiner Massestrukturen nach und rufen dadurch künstlich erzeugte Effekte hervor.

Der erste Teil dieser Arbeit untersucht diese Effekte und ihre Auswirkungen auf verschiedene Kenngrößen der Gravitationslinsen Theorie. Wir legen dabei besonderen Wert auf die Fähigkeit in den Simulationen des Gravitationslinseneffekts sehr kleine, real existierende Strukturen aufzulösen. Diese Arbeit untersucht als Erste systematisch den Einfluss des Teilchenrauschens auf die wichtigsten Kenngrößen des Gravitationslinseneffekts und vergleicht die Auswirkungen des Teilchenrauschens mit kleinen physikalischen Massestrukturen der Simulation. Die mathematische Beschreibung des Teilchenrauschens in dieser Arbeit basiert auf der Anwendung der Bootstrap Methode auf die Teilchen der Simulation. Beginnend mit der Massendichte beschreiben wir den Effekt am Beispiel der derzeit größten Simulation von Galaxienhaufen, der Phoenix Simulation von Gao et al. (2012). Obwohl die Auswirkung des Teilchenrauschens auf die Massendichteverteilung klein ist (wenige Prozent), wird der Effekt durch die Nichtlinearität des Gravitationslinseneffektes verstärkt. Wir untersuchen unter Anderem die Unregelmäßigkeit derjenigen Linien, an denen die Vergrößerung durch den Linseneffekt formell gegen unendlich strebt. An diesen Orten entstehen bevorzugt die sehr stark vergrößerten Bilder der im Hintergrund befindlichen Quelle. Die korrekte Beschreibung der Auswirkungen des Teilchenrauschens auf die Mehrfachbilder erfordert eine Betrachtung unter bayesschen Gesichtspunkten. Um unphysikalische und nicht beobachtbare Einflüsse wie die Position der Lichtquelle im Hintergrund herauszurechnen, rekonstruieren wir die Quelle in jedem Schritt der Berechnung des Effekts des Teilchenrauschens. Im Weiteren vergleichen wir das Teilchenrauschen mit dem Einfluss von echten sehr kleinen Massestrukturen. Für jede der Kenngrößen des Gravitationslinseneffekts untersuchen wir das untere Limit, ab dem der Einfluss kleiner Masseverteilungen nicht mehr zuverlässig simuliert werden kann. Wir untersuchen ebenfalls die Abhängigkeit dieses Limits von der

Struktur in der Lichtquelle. Außerdem leiten wir analytische Formeln her, mit denen die Größe abgeschätzt werden kann, die eine numerische Simulation haben muss, damit Massestrukturen einer geforderten Größe in Simulationen des Gravitationslinseneffekts aufgelöst werden können.

Im Zweiten Teil dieser Arbeit rekonstruieren wir die bayonische und dunkle Massenverteilung des Galaxienhaufens MACS J1149+2223, der als Teil des 'Cluster Lensing and Supernova Survey with Hubble' (CLASH) Programms beobachtet wurde. Die mehrfachen Bilder einer großen Quell-Spiralgalaxie, erstrecken sich über das Zentrum des Galaxienhaufens. Für die Rekonstruktion der Masse verwenden wir zwei verschiedene Ansätze. Der erste Ansatz basiert auf den Positionen der mehrfachen Bilder. Dafür identifizieren wir doppelt so viele Positionen wie bisher publiziert waren. Diese neuen Punkte beschreiben insbesondere die nähere Umgebung zweier Galaxien im Haufen, jeweils im Zentrum eines Einstein Rings, sowie den innersten Bereich des Galaxienhaufens. Auf Grund der radius-abhängigen Elliptizität der Massenverteilung präsentieren wir in der Arbeit zwei analytische Modelle für den Galaxienhaufen. Als zweiten Ansatz zeigen wir als erste Arbeit eine komplette Rekonstruktion der detaillierten Helligkeitsverteilung der mehrfachen Bilder der Spiralgalaxie. Dieser erheblich aufwändigere Ansatz zur Rekonstruktion reproduziert alle Details der Bilder, wie zum Beispiel die Details der zwei Einstein Ringe. Die Restungenauigkeit dabei ist vergleichbar mit dem Rauschen der HST Beobachtungen. Die Steigung der kompletten Massenverteilung des Galaxienhaufens ist vergleichbar mit früheren Beobachtungen. In MACS J1149+2223 ist der Anteil derjenigen Galaxien die nahe am Zentrum des Galaxienhaufens liegen an der Gesamtmassenverteilung wichtig für die Messung der Steigung der Masseverteilung. Die Steigung des Anteils der Dunklen Materie ist flacher als in numerischen Simulationen der Strukturbildung Dunkler Materie vorhergesagt. Dies könnte darauf hindeuten, dass Baryonische Prozesse, die eine Abflachung des Dunklen Materie Profils bewirken in der Entstehungsphase der zentralen Bereiche von Galaxienhaufen eine wichtige Rolle spielen.

Zuletzt untersuchen wir zwei Galaxien im Galaxienhaufen MACS J1149+2223 genauer. Mit Hilfe des zuvor erstellten Massenmodells können wir nun die Massenverteilung beider Galaxien genau messen. Wir testen je drei analytische Modelle für die Massenverteilung beider Galaxien und bewerten sie mit Hilfe Bayes Theorems. Alle drei Modelle für beide Galaxien beschreiben die Massenverteilung im Rahmen der Genauigkeit der Methode ähnlich gut. Damit erhalten wir nicht nur robuste Vorhersagen für die Details der Massenverteilung, sondern auch eine Abschätzung für den systematischen Fehler. Beide Galaxien zeigen deutlich schneller abfallende Massenverteilungen im Vergleich zu isolierten Galaxien. Dies zeigt deutlich, dass Galaxien in der Nähe eines Galaxienhaufens durch die Gravitationswirkung an Masse verlieren. Dies geschieht von außen nach innen, weswegen die "Größe" der Galaxie von ihrer Umgebung abhängig ist, so zum Beispiel von der Entfernung der Galaxie zum Zentrum in einem Galaxienhaufen. Dies wird dadurch untermauert, dass die zweite Galaxie die wir betrachten diesen Effekt sehr stark zeigt. Auf Grund der vorteilhaften Lage beider Galaxien inmitten der Mehrfachbilder in MACS J1149+2223 sind wir in der Lage, die Massenverteilung der Galaxien über einen großen radialen Bereich zu messen.

Chapter 1

Introduction

1.1 Galaxies and Galaxy Clusters

The standard cosmological model to date is the so-called Cold Dark Matter model with a nonzero dark energy term ($\Lambda\mathrm{CDM}$). In this model the universe is dominated by a form of matter that is yet of unknown nature, but whose particles have a thermal velocity that is thought to be negligible thus 'cold'. In the last few decades increasingly detailed numerical N-body simulations (Frenk et al. (1985); Navarro et al. (1997); Reed et al. (2005); Diemand et al. (2004); Springel et al. (2001, 2005); Merritt et al. (2006); Gao et al. (2012)) have established an understanding of cosmological structure formation in the $\Lambda\mathrm{CDM}$ universe. In this picture structures form in a hierarchical fashion where more massive objects form via the progressive merging of smaller structures.

High resolution Dark Matter-only (DM-only) N-body simulations to date follow structures over a large range of mass scales in the context of cosmological relevant simulation box sizes. Those simulations predict self-similar mass profiles for the DM halos of all mass scales, that are well fit by either an Einasto profile or a Navarro, Frenk and White profile (Navarro et al. (1997)). This mass density profile features a central DM cusp with a 3D slope of $\gamma_{\mathrm{DM}} = \partial \log(\rho) / \partial \log r \approx -1.0$ and a steeper decline at larger radii ($\gamma_{\mathrm{DM}} = -3$). In galaxy cluster simulations, the central density is found to be related to the background density at the formation time, therefore massive clusters are less dense due to the later formation times. Due to the hierarchical build up of structures, on average $11(7)\%$ of the halo mass of clusters (galaxies) is associated with gravitationally bound subhalos (Gao et al. (2012)). The abundance of substructures with a particular mass, $N \propto \mu^{\beta}$ where $\mu = M_{\mathrm{sub}}/M_{200}$ [1], on galaxy scales (Springel et al. (2008)) and on cluster scales (Gao et al. (2012)) are remarkably similar ($\beta = -0.94$ and $\beta = -0.98$ respectively). The subhalo distribution independently of subhalo mass tends to avoid the central regions and thus is only as biased tracer of the total mass distribution of clusters or galaxies.

On galaxy scale, there is an apparent discrepancy between the number of simulated and the number of observed satellites, the so-called 'missing satellites' (Klypin et al. (1999)). The

[1] M_{200} is the mass within a sphere with radius r_{200} and a mean density 200 times the critical density

discovery of ultra-faint satellites in the SDSS survey (e.g. Belokurov et al. (2007)) and several detections of satellites with very high mass-to-light ratio via gravitational lensing (Vegetti et al. (2010, 2012) now alleviate the problem and indicate that low-mass satellites indeed exist but that somehow their star formation is suppressed (Kaufmann et al. (2007); Kravtsov (2010)). The second discrepancy between observations and simulations is titled the 'too big to fail' problem. Simulations predict a central density cusp and therefore too much mass in the central regions of dwarf galaxies compared to observations. Recent observations of Milky Way Satellites show that the central regions are indeed cored (Walker & Peñarrubia (2011); Amorisco et al. (2013)). A solution to both problems might be found in a better understanding of the baryon interaction with the DM during formation and merging of galaxies. Governato et al. (2012) and Pontzen & Governato (2012) for example show that repeated, bursty gas outflows driven by supernova can flatten the DM profile by transferring energy form the gas to the DM particles.

The latter problem also persists in *galaxy cluster* scale objects, the main focus of this thesis. Galaxy clusters provide a powerful tool to compare the predictions from numerical simulations with observations. In the outer regions, clusters are expected to be DM dominated. And indeed, in this regions, DM-only simulations and observations agree very well on the mass profile (e.g. Sand et al. (2004, 2008); Okabe et al. (2010); Newman et al. (2013)). The centres of clusters are, however, very nonlinear and systems of different scales interact. At very small scales, the baryons in the Brightest Cluster Galaxy play a very important role in shaping the total mass distribution. To date simulations including different baryonic physics do not agree on the role of baryons in the transition region of a few up to tens of kpc from the cluster centre. The gravitational pull from baryons at the centre of the cluster causes the DM profile to steepen compared to purely DM simulations (Gnedin et al. (2004); Sellwood & McGaugh (2005); Sommer-Larsen & Limousin (2010)), an effect called adiabatic contraction. Active Galactic Nuclei (AGN) feedback can repeatedly heat and eject gas that returns after cooling and thus irreversibly shaping a centrally cored DM profile (e.g. Martizzi et al. (2013)). Galaxies orbiting in a cluster profile might also transfer some of their energy to the halo, heating and thereby flattening the central cusp (El-Zant et al. (2001, 2004)).

This thesis will focus on the the *gravitational lensing analysis of galaxy clusters*. On large scales there are, however independent constraints on the mass distribution of galaxy clusters from the Sunyaev-Zel'dovich (SZ) effect (Williamson et al. (2011); Marriage et al. (2011); Planck Collaboration et al. (2013)) and from X-ray temperature and luminosity measurements (see e.g. Ettori et al. (2013) and references therein). At very small scales there is essential information from the velocity dispersion measurements of the stars in cluster galaxies. There has been considerable effort to combine the different scales and methods in order to get a coherent picture of the cluster mass distribution on a large range of scales (Sand et al. (2004, 2008); Newman et al. (2013, 13b); On scales $> 100\ \mathrm{kpc}$ the distortion of background galaxies constrains the mass with the weak lensing. On very small scales stellar kinematics of the BCG $< 10\ \mathrm{kpc}$ constraints the inner part while the multiple images from strong lensing bridge the range in between.

By investigating a sample of 12 X-ray luminous clusters in the MACS survey, Zitrin et al. (2011) compare properties of the *cluster population* such as the concentration of the cluster mass distribution and the distribution of Einstein radii with theoretical predictions from simulations. They find that the observed Einstein radii are by a factor of 1.4 larger than predicted from

ΛCDM. Lensing bias, the preferred selection of strong lensing clusters, might explain some of this discrepancy along with the problem that cluster mass concentrations inferred from lensing are usually also too big (Comerford & Natarajan (2007); Oguri et al. (2009); Meneghetti et al. (2011)).

For the study of small scale cluster substructure such as cluster galaxies or even DM subhalos, a detailed high resolution modelling is needed on a cluster-by-cluster basis. If a high resolution model is found, the smallest details of clusters can be studied: The mass distribution of member galaxies in a dense environment, the DM content of the galaxies, the truncation and stripping of matter from galaxies or misalignment of the surface light distribution compared to the total galaxy mass distribution. The high magnification of galaxy clusters opens the possibility to use them as natural telescopes allowing to probe high redshift galaxies with gravitational lensing. This has been done for example for MACS J1149+2223 by Zheng et al. (2012) who report the discovery of a background galaxy at redshift $z = 9.6$. Using a larger sample of galaxy clusters, this can be used to probe the properties of high-redshift sources in order to study the morphology and the evolution of galaxies.

If the gravitationally lensed images are delensed, the properties of individual source galaxies can be studied. For example Yuan et al. (2011) studied the metallicity gradient of the spiral source galaxy using an early lens model for MACS J1149+2223 . If the data quality is good enough, one could even search for low mass-to light or even dark substructure as has been done on galaxy scales by Vegetti et al. (2010, 2012).

1.2 Gravitational Lensing

Gravitational lensing provides an independent means of measuring the total matter distribution in galaxies and galaxy clusters. The effect is independent of the nature of the mass and therefore allows to constrain the effects of baryonic matter and dark matter without any assumptions that mass follows light.

Although the idea dates back to the late 17th century to Cavendish and Laplace, the systematic description of the light deflection by massive objects began in the late 1910's. Einsteins theory of General Relativity (GR) provided an adequate foundation for the theoretical description. In 1937, Zwicky considered lensing by more distant objects such as galaxies and the thereby increased image separation which is more easily observable by telescopes. Only in the 1980's the technical developments such as CCD and modern telescopes such as the Very Large Array enabled the astronomers to observe for the first time multiply lensed quasars (Walsh et al. 1979).

Today the field is divided into three regimes:

1. Strong gravitational lensing (SL) describes the regime where a background source is multiply lensed by a foreground object. This includes high-magnification objects such as giant arcs in galaxy clusters (for two prominent examples see for example MACS J1206 (Ebeling et al. (2009) or Abell 1689 (Broadhurst et al. (2005)) and Einstein rings in the case that the source is precisely aligned behind a lens galaxy (see for example SDSS J0946+1006 (Gavazzi et al. (2008)) for an especially nice double Einstein ring).

2. Weak Gravitational Lensing (WL) describes the distortion of the shapes of background galaxies by massive objects. A first theoretical basis of weak lensing mass reconstruction is found by Kaiser & Squires (1993). Depending on the scale of the lens one can distinguish cluster weak lensing (Okabe et al. (2010); von der Linden et al. (2012); Newman et al. (2013)), galaxy-galaxy lensing, or weak lensing by large-scale structure (e.g. Heymans et al. (2012)). Due to the intrinsic ellipticity of the background galaxies and the small weak lensing effect, weak lensing methods are intrinsically statistic.

3. Microlensing describes the change in the apparent brightness due to the relative motion of a background source relative to a small lensing mass such as a star. The source gets briefly multiply imaged, however the multiple images are too close to be resolved. The characteristic change in the light curves can be used to detect faint objects such as extrasolar planets (e.g. Paczynski (1996), or Gaudi (2012) and references therein).

In this thesis we focus on strong lensing on scales of galaxy clusters. In the following we give a short overview of the lensing geometry and summarise the important equations.

Theory, Geometry and Equations

The theory of gravitational lensing describes the deflection of light rays from a 'source' at distance D_s by a 'lens' at distance D_d before they are observed by an observer at present date. The distance from the lens to the source is denoted D_{ds}. Distances here are angular diameter distances. The full treatment is done by solving the equations of General Relativity where light travels along null geodesics. However, we consider the simpler case with two approximations. In the case of weak gravitational fields the GR equations can be linearised. If we additionally assume that the extend of the mass can be approximated as a thin sheet compared to the distance to the source, the so called 'thin lens approximation' is valid. In this approximation the rays are deflected instantaneously at the lens plane.

Figure 1.1 shows a schematic overview of a typical gravitational lensing geometry. The physical coordinate vectors are $\boldsymbol{\eta}$ on the source plane and $\boldsymbol{\xi}$ on the lens plane. These transform to angular coordinates $\boldsymbol{\beta}$ and $\boldsymbol{\theta}$ by scaling with the appropriate angular diameter distances

$$\beta = \eta / D_s \qquad\qquad \theta = \xi / D_d. \tag{1.1}$$

For convenience, we define a 'critical density' that depends on the relative distances of observer, lens and source,

$$\Sigma_{\mathrm{crit}} = \frac{c^2 D_s}{4\pi G D_d D_{ds}}. \tag{1.2}$$

In the thin lens approximation, we project the mass distribution $\rho\left(\boldsymbol{r}\right)$ that acts as the lens on a 2D plane and obtain the surface mass density,

$$\Sigma(\boldsymbol{R}) = \int_0^{D_s} \mathrm{d}z \, \rho\left(z, \boldsymbol{R}\right), \tag{1.3}$$

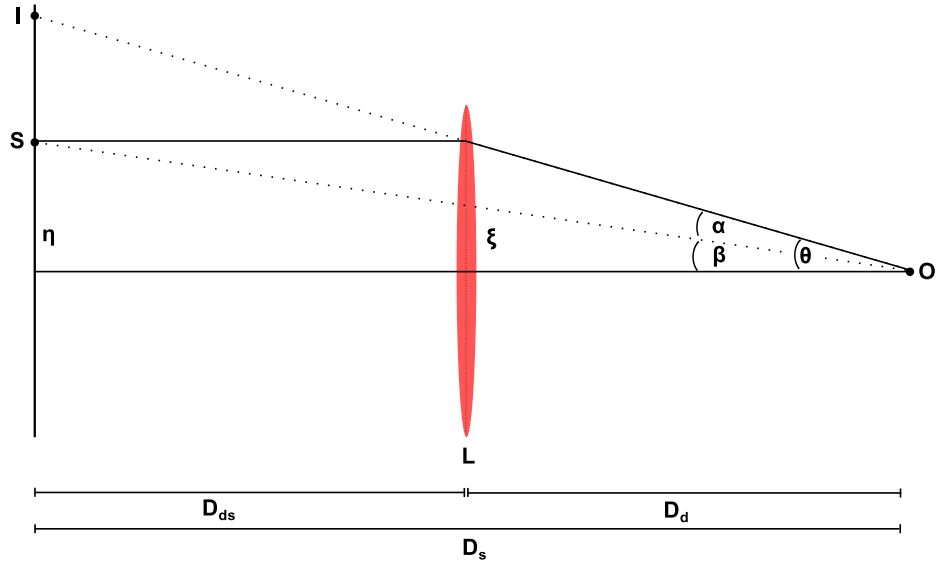

Figure 1.1: Gravitational lensing diagram. Source at source plane coordinates $\boldsymbol{\eta}$ is at position angle $\boldsymbol{\beta}$ and a angular diameter distance D_s from the observer O. The lens is at a distance D_d, the image position I is shifted by the deflection angles $\boldsymbol{\alpha}$ to the apparent position angle $\boldsymbol{\theta}$.

or the scaled surface mass density, the *convergence* in scaled and in angular units,

$$\kappa\left(\boldsymbol{\theta}\right) = \frac{\Sigma\left(\boldsymbol{\theta}\right)}{\Sigma_{\mathrm{crit}}}. \tag{1.4}$$

The *deflection* of light rays due to a mass distribution is calculated from the GR equations, by applying Fermat's principle (for detailed derivation see for example Schneider et al. (1992) p. 100 ff. or Petters et al. (2001) p. 66 ff.). The difference in direction between incoming and exiting light ray is the 'deflection angle' in angular coordinates,

$$\boldsymbol{\alpha}\left(\theta\right) = \frac{1}{\pi}\int_{\mathbb{R}^2} \mathrm{d}\theta'^2\, \kappa\left(\boldsymbol{\theta}'\right) \frac{\boldsymbol{\theta} - \boldsymbol{\theta}'}{\left|\boldsymbol{\theta} - \boldsymbol{\theta}'\right|^2}. \tag{1.5}$$

With these deflection angles we can describe the light deflection from the lens plane to the source plane using the 'lens equation',

$$\boldsymbol{\beta} = \boldsymbol{\theta} - \boldsymbol{\alpha}\left(\boldsymbol{\theta}\right). \tag{1.6}$$

From Eq. (1.5) we get with the vector relation $\nabla \ln\left|\boldsymbol{\theta} - \boldsymbol{\theta}'\right| = \left(\boldsymbol{\theta} - \boldsymbol{\theta}'\right)/\left|\boldsymbol{\theta} - \boldsymbol{\theta}'\right|^2$ that the deflection angle $\boldsymbol{\alpha}\left(\boldsymbol{\theta}\right)$ can be written as the gradient

$$\boldsymbol{\alpha}\left(\boldsymbol{\theta}\right) = \nabla\psi\left(\boldsymbol{\theta}\right) \tag{1.7}$$

of a lensing potential

$$\psi\left(\boldsymbol{\theta}\right) = \frac{1}{\pi}\int_{\mathbb{R}^2} \mathrm{d}\theta'^2\, \kappa\left(\boldsymbol{\theta}'\right) \ln\left|\boldsymbol{\theta} - \boldsymbol{\theta}'\right|. \tag{1.8}$$

From Eqs. (1.5) and (1.8) we find that the lensing potential is the solution of the 2D Poisson equation

$$2\kappa = \nabla_\theta^2 \Psi\left(\boldsymbol{\theta}\right). \tag{1.9}$$

From the lensing potential Eq. 1.8 we obtain the derivatives, which are the important quantities for gravitational lensing. The Jacobian Matrix of the lens mapping $\boldsymbol{\beta} = \boldsymbol{\theta} - \boldsymbol{\alpha}$ contains the second derivatives of the lensing potential Eq. (1.8),

$$\boldsymbol{A} = \frac{\partial \boldsymbol{\beta}}{\partial \boldsymbol{\theta}} = \left(\delta_{i,j} - \frac{\partial^2 \psi(\boldsymbol{\theta})}{\partial\theta_i \partial\theta_j} = \right) \begin{pmatrix} 1-\kappa-\gamma_1 & -\gamma 2 \\ -\gamma_2 & 1-\kappa+\gamma_1 \end{pmatrix}, \tag{1.10}$$

namely the shear $\boldsymbol{\gamma} = (\gamma_1, \gamma_2)$ where

$$\gamma_1 = 1/2\left(\psi_{,11} - \psi_{,22}\right) \quad \text{and} \quad \gamma_2 = \psi_{,12} \tag{1.11}$$

and the convergence

$$\boldsymbol{\kappa} = 1/2\left(\psi_{,11} + \psi_{,22}\right). \tag{1.12}$$

The inverse of the determinant of the Jacobian is the magnification,

$$\mu = \frac{1}{\det \boldsymbol{A}} = \frac{1}{(1-\kappa)^2 - |\boldsymbol{\gamma}|^2}, \tag{1.13}$$

only if there is a point where $\det \boldsymbol{A} < 0$, the lens mapping is capable of producing multiple images. The points $\boldsymbol{\theta}$ on the lens plane with infinite magnification, $\det \boldsymbol{A} \to 0$, form the 'critical lines', the corresponding points on the source plane are called 'caustics'. A source outside the caustic on the source plane only gets distorted. If the source is crossing the caustic from outside inwards, two new gravitationally lensed images appear close to the critical lines and vice versa. Therefore the total number of lensed images always is odd.

1.3 Gravitational Lensing Studies of Galaxy Clusters - Outline of the Thesis

We have seen that cosmological structure formation as well as baryonic physics play a crucial role in shaping the large scale structures in our universe. This thesis focuses on the scale of galaxy clusters. Due to the nonlinearity of the assembly of galaxy clusters, theoretical predictions from nonlinear $\Lambda\mathrm{CDM}$ structure formation can only be tested by comparing observations and observational methods with predictions from high resolution N-body simulations.

This thesis investigates both, high accuracy simulations of gravitational lensing using high-resolution DM-only simulations and the reconstruction of deep Hubble Space Telescope (HST) observations of strongly lensed gravitational images in galaxy clusters.

1.3.1 N-body Simulations of Gravitational Lensing

In recent years there have been several ultra-high resolution N-body simulations of galaxies and galaxy clusters. While the Aquarius suite of simulations (Springel et al. (2008)) simulate high resolution galaxies, we focus on the analogous simulations on cluster scale halos, the Phoenix Simulations by Gao et al. (2012).

These simulations re-simulate nine selected galaxy clusters from a bigger, but less resolved simulation, the Millennium Simulation (Springel et al. (2005)). While the parent simulation provides a cosmological representative volume, the increased resolution of the zoom-in Phoenix simulations allows to accurately re-simulate the innermost regions of each cluster. The increased resolution also allows to follow the abundance, structure and individual history of the members of the subhalo population. The simulations follow the structure formation of dark matter in the form of DM particles with fixed mass resolution. The Millennium simulation starts with the initial conditions set up at redshift $z = 127$ and follows the evolution to the present time. During the Phoenix resimulations, outputs were stored uniformly spaced in $\log a$ where a is the scale factor, the outputs are stored from redshift $z = 79$ to 0. Six of the nine clusters of the Phoenix simulations were randomly chosen from the Millennium simulation clusters in the mass range from $5 < M_{200}/10^{14}h/\mathrm{M}_{\odot} < 10$ and three more massive clusters were selected with $M_{200} > 10^{15}/h\mathrm{M}_{\odot}$. This ensures that the less frequent rich galaxy clusters at the high-mass end are also included in the sample. For details on the selection criteria, the set-up of the re-simulation initial conditions and other details of the simulations see Gao et al. (2012) (also Springel et al. (2005) and Springel et al. (2008)). All clusters are simulated at two resolution levels, one even at four levels in order to study the convergence of the simulations.

During the run of the N-body simulations, the 3D positions, velocities and other parameters of all N-body particles are stored. We use the 3D particle positions for our simulations of gravitational lensing. The gravitational lensing through a N-body simulated mass distribution is simulated by shooting light rays through the simulated mass distribution from the lens plane to the source plane, a technique called 'ray-tracing'. However, the particle nature of the simulation and the limited resolution introduces spurious effects due to the particle noise of the N-body simulation. Thus before one is able to compare simulated gravitationally lensed images generated by ray-tracing through N-body simulations with results from observations, one has to carefully investigate *the effect of particle noise in N-body simulations of gravitational lensing.*

This is done in the first part of this thesis in Chapter 2. This research was published in Monthly Notices of the Royal Astronomical Society, Volume 430, Issue 3, p.2232-2248 (Rau et al. (2013)). In this paper we explore the effect of particle noise on different simulated lensing quantities such as the mass distribution, the deflection angles, the magnification and the simulated images. The effect of the noise depends on the smoothing method, the number of particles and thus the resolution of the N-body simulation used. We investigate the effect of particle noise on gravitational lensing simulations for the example of a state-of-the-art simulation, the Phoenix simulation by Gao et al. (2012). We also compare this particle noise with the physical substructures in the simulation, thus giving a limit on resolved substructures. We finally give a scaling relation for the required size of a simulation in order to resolve a given substructure size.

1.3.2 Galaxy Cluster Mass Reconstruction from Hubble Space Telescope Observations

The second and third part of this thesis focus on the detailed mass reconstruction of Hubble Space Telescope (HST) observations of the gravitational lensing cluster MACS J1149+2223. The Advanced Camera for Surveys ACS on board the HST provides unique high-resolution observations of galaxy clusters and their strong gravitationally lensed images. We use images from the Cluster Lensing and Supernova Survey with Hubble (CLASH) program (Postman et al. (2012)), which has observed 25 (20 X-ray selected and 5 selected for their lensing strength) galaxy clusters in 25 filters from near-UV to near-IR. The selection criteria for the clusters based on X-ray strives to avoid lensing bias, the bias introduced by selecting strong lensing clusters that are more concentrated than the average. This might be a step towards solving a discrepancy between observations that predict higher cluster concentrations than simulations (e.g. Sereno et al. (2010)), and the Einstein Radius distribution found by Zitrin et al. (2011) which is $\sim 1.4\mathrm{x}$ bigger than those expected from simulations. CLASH data is available[2] in two resolutions, $65\mathrm{marcsec}$ and $30\mathrm{marcsec}$.

The major CLASH scientific goals are: a) the search for supernovae type Ia out to redshift 2.5, b) the detection of high-redshift galaxies due to the high magnification of the clusters, and *c) to study the cluster mass distribution and its components, the BCG, the DM in the cluster, cluster galaxies and possibly DM substructures in the clusters* (Postman et al. (2012)). The second and third part of this thesis will focus on c), the lensing reconstruction of one of the clusters observed by CLASH, MACS J1149+2223, and the reconstruction of the mass distribution of two cluster galaxies in detail.

In Chapter 3 we present a new analytic model for the mass distribution of MACS J1149+2223, a strong lensing cluster at redshift $z = 0.54$. We use two different techniques for the lensing reconstruction. The simpler approach is based on multiple image positions and we identify a huge number of new constraints for the main lensed image system. The full lensing reconstruction is done using the full surface brightness distribution of the large multiply lensed images of the main image system. We present our best lensing model and investigate the radial profile of the total cluster mass distribution.

Chapter 4 focuses on two galaxies in the cluster MACS J1149+2223. The detailed model in Chap. 3 allows us to compare three different analytic substructure profiles for the two cluster galaxies. We rank the modelling performance with a Bayesian argument, and analyse the mass distribution and the slope of both galaxies in detail.

[2]Data publicly available at http://archive.stsci.edu/prepds/clash/

Chapter 2

The Effect of Particle Noise in N-body Simulations of Gravitational Lensing

S. Rau,[1] S. Vegetti,[2] S. D. M. White[3]
published in MNRAS, Volume 430, Issue 3, p.2232-2248 on February 7, 2013

ABSTRACT

High resolution dark matter only simulations provide a realistic and fully general means to study the theoretical predictions of cosmological structure formation models for gravitational lensing. Due to the finite number of particles, the density field only becomes smooth on scales beyond a few times the local mean interparticle separation. This introduces noise on the gravitational lensing properties such as the surface mass density, the deflection angles and the magnification. At some small-scale mass limit, the noise due to the discreteness of the N-body simulation becomes comparable to the effects of physical substructures. We present analytic expressions to quantify the Poisson noise and study its scaling with the particle number of the simulation and the Lagrangian smoothing size. We use the Phoenix set of simulations, currently the largest available dark matter simulations of clusters to study the effect of limited numerical resolution and the gravitational strong lensing effects of substructure. We quantify the smallest resolved substructure, in the sense that the effect of the substructure on any strong lensing property is significant compared to the noise, and we find that the result is roughly independent of the strong lensing property. A simple scaling relates the smallest resolved substructures in a simulation with the resolution of the N-body simulation.

[1]Max-Planck Institute for Astrophysics, Karl-Schwarzschild Str. 1, D-85748, Garching, Germany
[2]Kavli Institute for Astrophysics and Space Research, MIT, Cambridge, MA 02139, USA
[3]Max-Planck Institute for Astrophysics, Karl-Schwarzschild Str. 1, D-85748, Garching, Germany

2.1 Introduction

The cold dark matter (CDM) paradigm makes two major predictions on the mass structure of dark matter haloes. Dark matter haloes at all scales are expected to have a universal mass density profile and to be populated by a large number of mass substructures (Gao et al. (2004); Diemand et al. (2004); Springel et al. (2005); Gao et al. (2012)). Gravitational lensing provides a unique tool to probe the mass distribution of galaxies and galaxy clusters and therefore to test this model. At galaxy cluster scale, a number of large gravitational lensing surveys (e.g. CLASH, Postman et al. (2012); SLOAN, Oguri et al. (2012)) have accurately determined the shape of the mean mass density profile. Using a combination of weak and strong lensing data for example Newman et al. (2009) and Umetsu et al. (2011) have measured the mass distribution of galaxy clusters from kpc to Mpc scales. In general, both in simulations and observations, the central profile of clusters shows a significant amount of scatter between different observations (Sand et al. (2002, 2004); Newman et al. (2011)) as well as between different simulations (Gao et al. (2012)); this scatter might be explained in the context of a hierarchical structure formation model where clusters form late and therefore are not fully relaxed objects.

Combining weak and strong lensing is especially important to measure the cluster concentration, defined as the ratio of the virial radius to the radius where the density profile has an isothermal slope. To date, there seems to be a discrepancy between observations and theoretical expectations, with observed lensing clusters being more centrally concentrated than predicted by CDM simulations. This might also be the reason for some unexpectedly large observed Einstein radii (Zitrin et al. (2011)). Strong lensing bias might explain these differences (Comerford & Natarajan (2007); Oguri et al. (2009); Meneghetti et al. (2011)) due to projection effects for triaxial halos, baryons, or of foreground or background objects.

At present, strong gravitational lensing is the only available tool to detect substructures within the lensing mass distribution beyond the Local Universe and independently of the luminous content. Faint and even dark substructures can be detected in lens galaxies either by observing multiply imaged lensed quasars with flux ratio anomalies (Mao & Schneider (1998); Dalal & Kochanek (2002); Metcalf & Zhao (2002); Kochanek & Dalal (2004); Bradač et al. (2002); Fadely & Keeton (2012).) or via the gravitational imaging technique on Einstein rings and multiply imaged arcs (Vegetti & Koopmans (2009); Vegetti et al. (2010, 2012)) While most of the observational and theoretical work that has been done to date is at the scale of galaxies, the current search for mass substructure can be extended to galaxy clusters using gravitationally lensed giant arcs. The large magnification of these arcs makes them sensitive to substructure masses as small as $\sim 10^8 - 10^9 M_\odot$ that can be detected using the gravitational imaging technique.

Constraining the fraction of mass substructure at the scale of galaxy clusters is also important for understanding the properties of high redshift galaxies. Many of the properties (e.g. stellar mass and star formation rate) of high redshift galaxies detected using clusters as cosmic telescopes, can be measured accurately only when the source magnification is known. However, mass substructure introduces significant fluctuations in the source magnification and needs to be properly accounted for. In principle, numerical simulations could be used to quantify the effect of undetected substructure on the source magnification. In practice, however, the resolution of the simulation could potentially lead to an underestimate of the substructure fraction in the in-

ner regions, while particle noise could mimic the effect of substructure and introduce spurious effects. In general, from a numerical point of view, when comparing theoretical prediction from numerical simulations and results from observations, one should carefully quantify the effect of the limited resolution of the simulation and in particular, the effect of the particle noise.

In this paper, we use the highest available resolution cluster simulations, the Phoenix simulations by Gao et al. (2012) to simulate gravitational lens clusters. Our main goal is to investigate the properties of the particle noise with a focus on multiple lensing properties and gravitationally lensed images. The first part of the paper is focused primarily on the quantification of the particle noise for numerical simulations of gravitational lensing, while the second part is focused on comparing the effects of particle noise with those of physical substructures. In particular, the paper is organised as follows. In Section 2.2 we briefly summarize the details of the Phoenix simulations. In Section 2.3 we will introduce the numerical lensing methods. We then quantify the effects of the particle noise on results from N-body simulations in Section 2.4. We consider major lensing quantities, such as the surface mass density, the deflection angles, and directly observable quantities such as the shear, the magnification, the critical lines and the lensed images. Section 2.5 investigates the scaling of the noise with number of particles and smoothing scale. In Section 2.6, we compare the effects of noise with those of physical substructures on each of the lensing properties. This comparison enables us to calculate a resolution limit for the smallest detectable substructures in a N-body simulation of gravitational lensing as a function of the particle number in the simulation.

2.2 Numerical Simulations

In this paper we use the Phoenix simulations by Gao et al. (2012) which are resimulations of 9 clusters from the Millennium Simulation (Springel et al. (2005)) . The simulations span masses from 7.5×10^{14} $\mathrm{M}_{\odot}$ for cluster C to 3.3×10^{15} $\mathrm{M}_{\odot}$ for cluster I within virial radii of 1.9 Mpc and 3 Mpc respectively. All Phoenix clusters are simulated at two resolution levels, Level-2 and Level-4, except for one cluster for which two additional resolution levels, Level-3 and Level-1, are available. The 3D profiles of the simulated N-body clusters from the Phoenix simulations can be reasonably well fit by two components, a smooth cluster component and additional small-scale substructures. The smooth component is triaxial and can be fit by either a NFW or an Einasto profile, although an Einasto profile seems to fit slightly better in most cases, with an average Einasto shape parameter of $< \alpha > \sim 0.175$. For a detailed description of the simulations and the parameters of all clusters we refer to Gao et al. (2012).

In this paper we focus, as an example, on the cluster E, its properties are listed in Table 2.1. Cluster E is simulated at two different resolutions and has a virial mass of $M_{200} \sim 8.1 \times 10^{14}\mathrm{M}_{\odot}$ inside $r_{200} \sim 1.9\ \mathrm{Mpc}$. Gao et al. (2012) quantify the performance of the NFW and the Einasto fit with a figure of merit function Q^2, defined as the squared logarithmic deviation $(\ln\rho - \ln\rho^{\mathrm{model}})^2$ averaged over logarithmic radial bins. For example for the E halo an Einasto profile with $Q = 0.067$ fits considerably better than a NFW profile with $Q = 0.135$. Gravitationally bound substructures (subhalos) in the simulation with more than ~ 20 particles are identified with the SUBFIND algorithm (for a recent comparison of different subhalo finders see Onions

Level	$m_{\rm p}[{\rm M}_\odot]$	N_{200}	$\epsilon[{\rm kpc}]$
4	1.39×10^8	5.8×10^6	3.84
2	6.06×10^6	1.3×10^8	0.44

Table 2.1: Properties of the cluster E of the Phoenix simulations.

et al. (2012)). Gao et al. (2012) describe the properties of the subhalo population in detail. In the mass range from $10^{-6} < M_{\rm sub}/M_{200} < 10^{-4}$ the number of substructures increases with decreasing subhalo mass as $dN/dM \propto M^{-0.98}$. The spatial subhalo distribution shows a distinct central core and the subhalos are found mainly at larger distances from the centre of the cluster.

For the lensing simulations throughout this paper we use the same cosmological parameters as in the simulations, $\Omega_{\rm M} = 0.25$, $\Omega_\Lambda = 0.75$ and $h = 0.73$. The N-body simulation stores outputs for redshifts uniformly spaced in $\log a$, where a is the scale factor. For the analysis presented in this paper, we consider the snapshot at redshift $z = 0.32$ and we place our simulated sources at redshift $z = 2.0$. These values are chosen such that the cluster is a relatively efficient lens, and the lensing configuration is comparable to observed strong lensing clusters, for example, the median cluster redshift for the CLASH survey is $z = 0.4$ (Postman et al. (2012)), while the mean source redshift distribution of the SLOAN giant arcs survey peaks at $z = 1.821$ (Bayliss et al. (2011)).

2.3 Lensing Theory

In this section, we describe how we process the simulation data to get a high resolution simulation of the gravitational light deflection by the N-body cluster.
During the N-body simulation, snapshots of the positions, velocities and other parameters of the particles were stored for multiple redshifts. We use these stored outputs of the N-body simulation for an accurate numerical simulation of the gravitational lensing effect. In particular, we use the 3D positions of the particles of the N-body simulation to calculate a smoothed 2D mass density distribution. We then use this smoothed particle distribution to calculate the main lensing properties such as the deflection angles $\boldsymbol{\alpha}$, the magnification μ, the shear γ and the lensed images.

We adopt the smoothing algorithm commonly used in smooth particle hydrodynamics (SPH) simulations (Monaghan (1992)) to get a smooth density distribution $\Sigma(\boldsymbol{x})$ from the $N_{\rm part}$ particles of the N-body simulation. We assign a different smoothing size l_p to each particle. This particle size is variable and adapted to the local mass density in 3D. More specifically, this smoothing size is chosen to be equal to the distance to the $N_{\rm ngb}$-th neighbour in 3D. By doing so, we use the full three dimensional density information to calculate the smoothing lengths of the particles. This is computationally more expensive than the equivalent 2D adaptive smoothing, but it results in a density map with an enhanced contrast (Li et al. (2006)). The exact choice for $N_{\rm ngb}$ depends on the form of the kernel. Increasing the number of particles in the kernel will increase the smoothing and will therefore reduce artificial particle noise, but it will also smooth physical substructures. In this paper, we use a fourth order polynomial and the distance to the

nearest 64 neighbours, for more details see Sec. 2.4.2. In Sec. 2.5, we will investigate the dependence of the noise on the number of neighbours. Once the smoothing length for each particle is calculated, we use two different methods to simulate the gravitational lensing by this smoothed N-body mass distribution.

The first method is based on a discretization on high resolution grids. In order to calculate the surface mass density $\Sigma(\boldsymbol{x})$, all particles are projected onto a 2D grid using a smoothing kernel, of smoothing length chosen as described above. The surface mass density is then scaled by the critical density $\Sigma_{\rm crit} = c^2 D_s/(4\pi G D_d D_{ds})$ to get the convergence $\kappa(\boldsymbol{x}) = \Sigma(\boldsymbol{x})/\Sigma_{\rm crit}$ where D_s, D_d and D_{ds} are the angular diameter distances from the observer to the source, to the lens and from lens to source respectively. Finally, the gravitational lensing potential $\Psi(\boldsymbol{x})$ (Bartelmann (2003)) is calculated by convolving the scaled surface mass density $\kappa(\boldsymbol{x})$ with a logarithmic kernel, $\Psi(\boldsymbol{x}) = \frac{1}{\pi}\int \mathrm{d}^2x' \kappa(\boldsymbol{x}') \ln|\boldsymbol{x} - \boldsymbol{x}'|$, using a Fast Fourier Transformation (FFT). Once the potential has been obtained, the lensing quantities $\boldsymbol{\alpha}, \boldsymbol{\gamma}$ and μ can be calculated by using derivatives of the 1st, the 2nd or combinations of the 2nd order, respectively. The derivatives can be done numerically via finite differencing, or in Fourier space directly. For the highest resolution simulations we project the particles onto two grids of 16384^2. Because of zero padding, the size of both grids is increased by a factor of two by the FFT. The coarse outer grid covers a large area of $(40 \cdot 230'')^2$ around the cluster and includes all external shear components. The fine inner grid covers an area of $(230'')^2$. This corresponds to a maximum resolution of $0.014''/\mathrm{pix}$ in the inner parts of the halo, which is a factor of 5 smaller than the softening length of the original simulations at Level-2. Both grids are centred on the cluster. In order to reduce the computational cost for the bootstrap resamplings described in Sec. 2.4, we reduce the grid size to 2048^2.

The second method for calculating the lensing quantities is the smooth particle lensing method (SPL) introduced by Aubert et al. (2007). This method uses Gaussian shaped particles with a smoothing length l_p and takes advantage of the linearity of the lensing quantities, $X(\boldsymbol{r}) = \sum_{p=1}^{N_{\rm part}} X_p(\boldsymbol{r})$, where $X \in \{\boldsymbol{\alpha}, \boldsymbol{\gamma}, \mu, \ldots\}$. As an example the deflection angle at any point on the lens plane is the sum of the contributions of the deflections of all particles of the N-body simulation. This second method is equivalent to convolving the 3D particle distribution with a specific kernel for each of the lensing properties (Aubert et al. (2007)); for the deflection angles in the r direction, for example, the kernel reads as follows,

$$W_\alpha(r) = \frac{m_p}{\pi \Sigma_{\rm crit}} \frac{\exp(\frac{-r^2}{2l_p^2}) - 1}{r}, \tag{2.1}$$

where r is the distance of each particle p to the evaluated point. The direct computation of the convolution is very expensive since it requires the evaluation of $N_{\rm part} \times N_{\rm ray}$ values. However, since the kernel depends on the distance as $1/r$, there exist methods in order to reduce the computational load. The most popular solution makes use of a tree code to sort and group all particles at large distance and approximate their contribution to any lensing property at a given point with a particle of bigger mass (Aubert et al. (2007)). In the rest of the paper, we will mostly use the FFT method, but we will also make use of the SPL formalism to quantify the particle noise analytically.

2.4 Particle Noise

The mass distribution of any N-body simulation is discretized by individual mass particles. This discrete numerical sampling of the underlying mass density distribution introduces shot noise, which will affect all the major gravitational lensing quantities.

In this section we first present the two methods that we use to quantify the particle noise in the simulation; we then discuss in more detail how the particle noise affects the individual lensing properties. The order follows the numerical procedure in the lensing simulations, based on the lensing potential obtained via FFT from the convergence. Therefore, we first focus on the projected surface mass density and discuss the properties of the particle noise and analytical approximations to them. The noise on the surface mass density is well described by local random fluctuations in the density. We derive all other lensing properties numerically from derivatives of the lensing potential. We therefore begin by discussing the noise on the first derivatives, the deflection angles. The Poisson equation introduces long-range correlations in the fluctuations of the lensing potential and the deflection angles. The deflection angles are used to solve the lensing equation, and are not directly observable. However, understanding their long-scale correlations will prove useful in understanding the noise properties of the strongly lensed images. We then focus on combinations of higher order derivatives of the lensing potential which are more severely affected by short-range noise correlations. These correspond to directly observable lensing properties such as the shear, the inverse of the magnification and the gravitationally lensed images.

In particular, the noise level on each lensing property will depend on parameters such as the N-body particle number, the particle size and the smoothing algorithm that is used to process the N-body particles. In this paper we calculate the noise for Poisson distributed particles. We are therefore assuming that each particle is sampled from a Poisson distribution with mean and variance one and that this sampling is equivalent to the Poisson sampling of an underlying true mass distribution.

The theoretical basis for the expectation value and the covariance analysis for the interpolation of irregular sampled measurements to a smooth map is covered in a series of three analytic papers by Lombardi & Schneider (2001, 2002, 2003). Focusing on gravitational lensing, Amara et al. (2006) study the effect of particle noise for an analytic singular isothermal ellipsoidal mass model and for a N-body cluster. They add artificial 2D Poisson noise to their simulated surface mass density and then visually compare the noise in the critical curve and caustic and the magnification of lensed images for several constant smoothing kernel sizes. Bradač et al. (2004) estimate the mean noise on the projected mass density within the critical lines by using 10 bootstrap resamplings (compare Sec. 2.4.1) of the particles of their numerically simulated cluster. They, however, use a smoothing algorithm based on a Delaunay tessellation of the N-body particles for their lensing simulation. For their analysis of the cusp relation, a relation between the magnification of multiply lensed images close to a cusp (Schneider & Weiss (1992)) they also compare the particle noise for the Delaunay tessellation smoothing with a more simple Gaussian kernel smoothing algorithm with fixed smoothing size.

Li et al. (2006) suggest adapting the size of the smoothing kernel in order to improve the contrast of the lensing simulation. They estimate the noise of their 3D density adaptive smoothing

algorithm for a uniform density field, for simulated isothermal ellipsoids and for a numerically simulated cluster and compare the results with the results from the simpler 2D adaptive smoothing. They simulate the particle noise by randomly populating fitted elliptical contours of the smooth halo with the same number of particles as the original simulation. They conclude that most of the wiggles in the critical line are not due to substructures in the simulation. Their simulations of the cusp-caustic relation for the N-body cluster and the Monte-Carlo re-sampled cluster show that the particle noise produces many high-order singularities. They also show that a more elliptical projected density is more sensitive to high-order singularities of the caustic. This is particularly important for simulating the anomalous flux-ratio problem with N-body simulations.

Although several authors have addressed the problem of the discreteness noise of a N-body simulation and have estimated the effect on some lensing properties, to our knowledge, to date no one has systematically investigated the implications for the simulation of gravitational lensing for very high resolution simulations. In this paper we use the smoothing algorithm from Li et al. (2006) and analytically and numerically investigate the magnitude of the effects of particle noise on the lensing properties. We extend the investigations of Li et al. (2006) on the particle noise with a focus on different lensing properties and multiply lensed images and compare the noise to the simulated substructures for a state-of-the-art N-body galaxy cluster simulation.

2.4.1 Bootstrap

In order to simulate the noise numerically, we create B bootstrapped resamplings of the particles from the N-body simulation. Each bootstrapped resampling is created by randomly choosing $N_{\rm part}$ particles with replacement from the $N_{\rm part}$ particles of the simulation. In this way, some particles will be included more than once, while others will not be included at all. We then project all particles on a grid and calculate the lensing potential, the deflection angles, the shear and the inverse of the magnification for each of the B resamplings. Because this calculation is very time consuming, we restrict our calculation to $B = 100$. This is sufficient to calculate statistically converged results for the lensing properties that we consider in Sec. 2.4.2 to 2.4.5.

To test whether the bootstrapping is a good estimator of the inherent particle noise, we test the bootstrapping method as follows. We randomly chose $0.01\ N_{\rm part}$ particles from the high resolution Level-2 simulation with replacement. This factor should be large enough to sample the total mass distribution randomly, independently of correlated phases, caused by the dynamical evolution during the N-body simulation. We repeat this 50 times, and then calculate the variance of those 50 randomly sub-sampled clusters. To test the validity of the bootstrap method, we then randomly choose one additional subset of $\tilde{N} = 0.01\ N_{\rm part}$ particles from the original $N_{\rm part}$ particles with replacement and multiply bootstrap it. We, therefore, randomly chose 50 times $\tilde{N}$ of those last $\tilde{N}$ particles with replacement. The two noise estimates for the subset of $0.01\ N_{\rm part}$ are identical. Therefore we can use the bootstrap method to estimate the particle noise of the original simulation.

For a high resolution lensing simulation, calculating the noise via the bootstrapping technique can be computationally very expensive. In particular, most of the computational effort is spent in projecting the simulation particles onto the two-dimensional grids. In the following, we present, therefore, a new way to calculate the noise analytically.

We will make use of the SPL method (Aubert et al. (2007)) to derive an analytic expression for the bootstrap noise. The SPL method evaluates the contribution of each particle separately, and it is, therefore, ideal to evaluate the noise caused by the discreteness of the N-body simulation. We assume uncorrelated and Poisson noise for the 3D particle distribution, that is, we assume for every particle a Poisson probability density distribution with a mean and variance of one of being included in the resampling. For a particle convolved with a kernel, the Poisson noise is smoothed out over the size of the kernel. The total variance at any point $\boldsymbol{x}$ on the lens plane is therefore a sum over all the uncorrelated variances of the individual N-body particles,

$$\sigma_Y^2(\boldsymbol{x}) = \sum_{i=1}^{N_{\rm part}} W_Y^2\left(|\boldsymbol{x} - \boldsymbol{x}_i'|, l_i\right), \tag{2.2}$$

where $Y \in \{\kappa, \boldsymbol{\alpha}, \boldsymbol{\gamma}\}$ and $W_Y(|\boldsymbol{x} - \boldsymbol{x}'|, l_p)$ is the appropriate SPL kernel listed in the following sections. This method calculates the noise directly without the need of numerical bootstrapping. However, evaluating Eq. (2.2) numerically for quantities like for example the deflection angles, is laborious. The kernel for the deflection angles is not compact and therefore for any point on the lens plane $\boldsymbol{x}$ one has to sum over the long-range contributions for *all* N-body particles. In order to effectively evaluate Eq. (2.2), one has to use some kind of approximation. Two possibilities are, either group distant particles and approximate the effect by a bigger particle in a tree code, or to use a two-dimensional approximation (see Sec. 2.5.2).

2.4.2 Surface Mass Density

The most basic quantity that can be derived from the discrete N-body particle distribution is the smoothed surface mass density. In the grid-based approach we derive all other lensing properties via FFT from the projected particle distribution, see Sec. 2.3. In this section, we describe therefore in detail, the smoothing algorithm and the noise properties of the projected mass density distribution. Simulations of gravitational lensing for a long time used fixed Gaussian kernels to smooth the particles of the N-body simulation (e.g. Bartelmann et al. (1998); Bradač et al. (2002); Macciò et al. (2006)), or adapted the smoothing size if too few particles fell into the kernel (e.g. Li et al. (2005)). A more sophisticated method was then proposed by Bradač et al. (2004) who used a Delaunay tessellation (Schaap & van de Weygaert (2000)) to obtain a smooth density distribution from the N-body particles of a numerical simulation. Li et al. (2006) suggested to adapt the size of the smoothing to the 3D density distribution in order to improve the contrast of the lensing simulation. They show that the smoothing size can be decreased significantly, if the size of the smoothing kernel is adapted to the distance to the nearest neighbours in 3D instead of 2D. Fewer physical substructures are smoothed out during the projection of the N-body particles, while retaining the same noise level. However, this relates the 2D distribution of the noise on the surface mass density to the line-of-sight integral of the 3D particle distribution and therefore results in a nontrivial signal-to-noise distribution on the lens plane as shown in sections 2.4.2 to 2.4.6 for the different lensing properties.

In this paper we will use the method from Li et al. (2006), and use the fully 3 dimensional particle distribution to determine the size of the smoothing kernel.

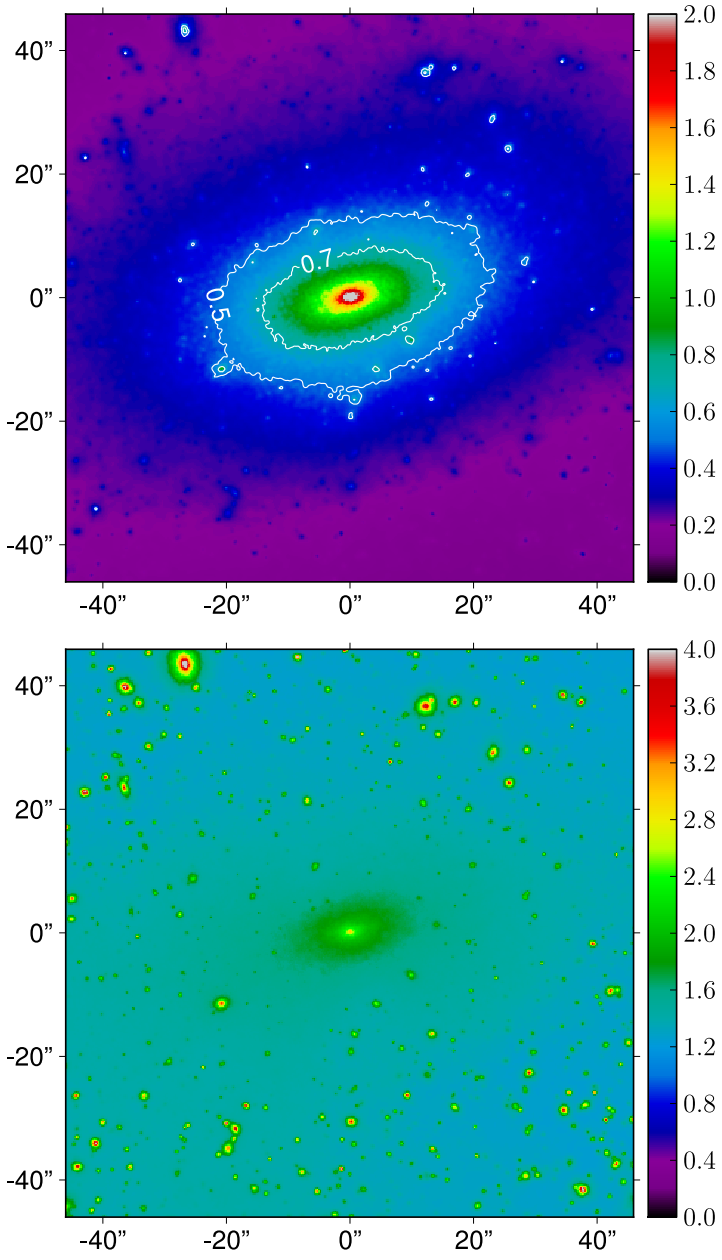

Figure 2.1: Top panel: Projected convergence of the N-body particle distribution at Level-2 resolution for cluster E. The smoothing is chosen to be equal to the 64th neighbour in 3D. Convergence κ for the central $(0.55\ \mathrm{Mpc})^2$, the critical lines are approximately the same size as the contours at $\kappa = 0.7$. The contours are irregular because of substructures and the effect of discreteness noise. Bottom panel: Particle noise of the convergence $\sigma_\kappa(\boldsymbol{x})$ in percent of the projected scaled surface mass density κ from 100 bootstrapped resamplings of the particle distribution

The 2D surface mass density $\Sigma(\boldsymbol{x})$ is calculated from the $N_{\rm part}$ particles of the N-body simulation. Each particle is projected with a normalized kernel, $\int \mathrm{d}^2\boldsymbol{x}' W_i(|\boldsymbol{x}-\boldsymbol{x}_i'|, l_i) = 1$ in order to obtain a smooth density distribution,

$$\Sigma(\boldsymbol{x}) = \frac{m_{\rm p}}{A} \sum_{i=1}^{N_{\rm part}} W_i\left(|\boldsymbol{x}-\boldsymbol{x}_i'|, l_i\right). \tag{2.3}$$

The size of the kernel, l_i, is different for each particle i and is calculated from the distance to the nearest $N_{\rm ngb}$ neighbours in 3D.

There are different forms of smoothing kernels, the most widely used 2D functions are Gaussian, $W_i(r) = 1/\left(2\pi\tilde{l}_i^2\right)\exp\left[-r^2/\left(2\tilde{l}_i^2\right)\right]$, a simple polynomial, $W_i(r) = 3/\left(\pi l_i^2\right)\left(1-r^2/l_i^2\right)^2$ for $r \le l_i$, or the more complicated polynomial (Li et al. (2006); Springel (2005)),

$$W_{\Sigma,i}(r) = \frac{80}{14\pi l_i^2}\begin{cases} 1-6(\frac{r}{l_i})^2+6(\frac{r}{l_i})^3, & 0\le r\le\frac{l_i}{2}, \\ 2(1-\frac{r}{l_i})^3, & \frac{l_i}{2}<r\le l_i, \\ 0, & \text{otherwise.}\end{cases} \tag{2.4}$$

For a Gaussian smoothing width $\tilde{l}_i = \sqrt{103/1120}\, l_i$, the effective area covered by a particle is equivalent to a particle smoothed by the two other kernels. The simulation of gravitational lensing does not strongly depend on the form of the kernel. Since the projection of the N-body particles on the lens plane is the most time consuming step, we choose the second kernel, which is the fastest to evaluate numerically.

The convergence, the surface mass density in units of the critical density, is shown in the top panel of Fig. 2.1 for the Phoenix cluster E at Level-2 resolution. The figure shows the central part of the halo, the side length is about three times the size of the critical lines. The extent of the critical line is comparable to the $\kappa = 0.7$ contours, the figure therefore covers the whole region where multiply lensed images occur. As an example, a second contour at $\kappa \sim 0.5$ is over plotted. Both contours are not smooth and show several irregularities. These 'wiggles' arise from two different effects. The first effect is due to the presence of physical mass substructure in the simulation. For example, in the central $(92'')^2$ region, shown in Fig. 2.1, there are 2597 subhalos identified by SUBFIND with $N_{\rm part} > 20$, of which 2131 have a $M_{\rm sub} < 10^9 \mathrm{M}_\odot$, 58 have a $M_{\rm sub} > 10^{10}\mathrm{M}_\odot$ and 408 have an intermediate mass. The second effect, which is clearly visible in the top panel of Fig. 2.1, is related instead to the presence of particle noise. Even for this very high-resolution simulation both effects are significant and comparable in the inner regions, $r < 20''$, of the halo. In the following, we will quantify the contribution to the surface mass density fluctuations due to particle noise.

By substituting one of the three smoothing kernels, for example Eq. (2.4), in the expression for the analytic variance, Eq. (2.2), we get an analytic expression for the particle noise on the surface mass density,

$$\sigma_\Sigma^2(\boldsymbol{x}) = \frac{m_{\rm p}^2}{A^2} \sum_{i=1}^{N_{\rm part}} W_{\Sigma,i}^2\left(|\boldsymbol{x}-\boldsymbol{x}_i'|, l_i\right). \tag{2.5}$$

The bottom panel of Fig. 2.1 shows the noise $\sigma_\kappa(\boldsymbol{x})$ on the surface mass density as a function of $\kappa(\boldsymbol{x})$. There is a significant difference to a calculation with 2D adaptive smoothing. In the

2D case, all line-of-sight N-body particles for a point on the lens plane are assigned the same smoothing length l. For this smoothing we expect the variance of the Poisson noise on the surface mass density to be proportional to the number of line-of-sight particles at each point. Since the number of particles can be estimated from the convergence κ via $A^2\Sigma_{\rm crit}\kappa\left(\boldsymbol{x}\right)/m_p$, we would expect the bottom panel of Fig. 2.1 to be roughly constant. In contrast, here, we adapt the smoothing to the local density in 3D, and therefore, the noise depends on the integrated particle density distribution along the line of sight and is more complicated than the simple 2D case. For the Level-2 resolution of the Phoenix simulations in Fig. 2.1 the mean noise on the surface mass density is about $1-2\%$ and $<5\%$ even in high density regions.

2.4.3 Deflection Angles

In the last section we quantified the noise on the surface mass density. This particle noise propagates through the Poisson equation, $2\kappa=\Delta\Psi$, to the lensing potential and to its derivatives. Although the first derivatives, the deflection angles, are not directly observable, understanding the noise on the deflection angles is essential to quantify and describe the noise on the lensed images. We calculate the noise on the deflection angles by projecting all particles with a modified kernel,

$$\boldsymbol{W}_{\sigma_\alpha^2}\left(\boldsymbol{x}\right)=\frac{c^2}{r_p^4}\left[\underbrace{G(r_p,l_p)^2-2G(r_p,l_p)}_{\rm A}+\underbrace{1}_{\rm B}\right]\begin{pmatrix}x^2\\y^2\end{pmatrix}. \tag{2.6}$$

Here $\boldsymbol{W}_{\sigma_\alpha^2}\left(\boldsymbol{x}\right)$ is a vector for the noise on the deflection angles in the x- and y directions, $c=m_p/(\pi\Sigma_c)$, r_p is the distance of particle p to the point $\boldsymbol{x}$, l_p is the smoothing length and $G(r_p,l_p)=\exp(\frac{-r_p^2}{2l_p^2})$. The first two terms in A can be easily calculated by direct numerical summation. This is necessary since the smoothing length l_p is different at each point. For the summation it is sufficient to consider points with $r_p\lessapprox 5l_p$, since at larger distances for both terms in A, the Gaussian kernel vanishes, $G(r_p,l_p)\to 0$. The second term, B, is easily evaluated by convolving the grid via FFT.

The noise on the deflection angles in x direction is shown in the right panel of Fig. 2.2 for the Level-2 version of cluster E. The side length of the figure is comparable to the size of a strongly lensed image. Over the size of a typical giant arc, the effect of shot noise on the deflection angles is a smooth function. The left panel of Fig. 2.2 shows a realisation of the particle noise on the deflection angles in the x direction. The marked region corresponds to the size of a typical multiply lensed image. Due to the $1/r$ dependence of the deflection angles, the particle noise is strongly correlated on long scales in the left panel of Fig. 2.2. These long-scale correlations will have a big effect on the calculation and the understanding of the noise on the lensed images presented in section 2.4.5.

2.4.4 Shear and Inverse of the Magnification

We will now study the noise on higher order, observable lensing quantities, namely the shear and the inverse of the magnification, before we will focus on the main strong lensing observables,

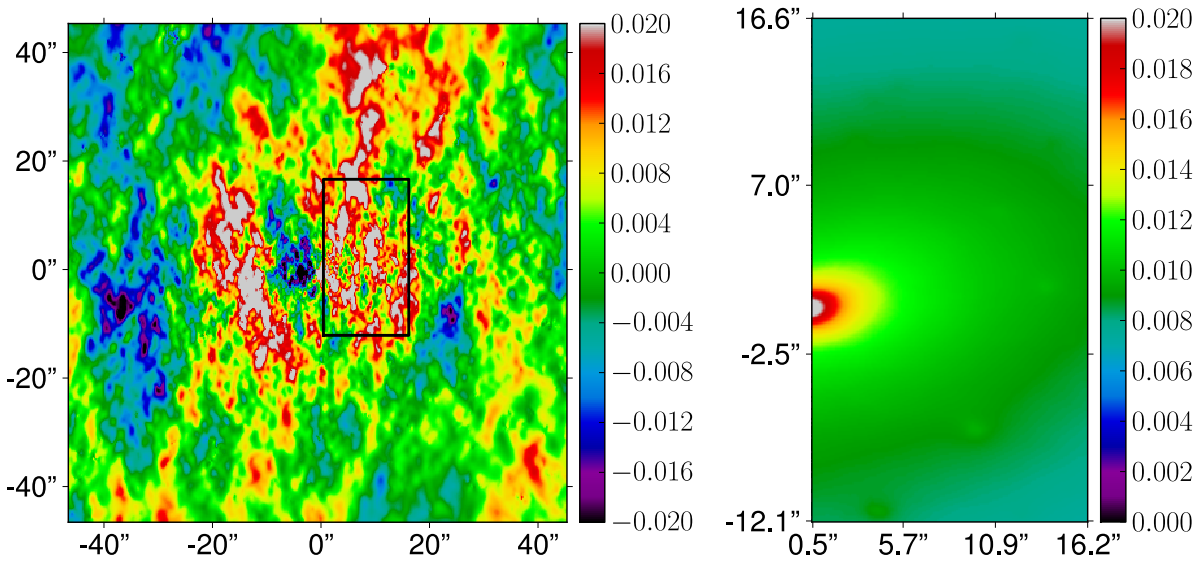

Figure 2.2: Difference between two random realisations of the particle noise of the deflection angles in x direction, $\alpha_x^1 - \alpha_x^2$ (left panel). The marked region shows the size of a typical image from Sec. 2.4.5. Standard deviation of the deflection angles in the marked region calculated with Eq. (2.6) (right panel). For both panels the colour scale is in arcseconds.

the lensed images in the next section. Since the magnification and both shear components are important for weak lensing studies, we will also discuss the analytic noise calculation from the particles of a N-body simulation. The shear and the scaled surface mass density are related to second derivatives of the lensing potential by $\gamma_1 = (\Psi_{,11} - \Psi_{,22})/2$, $\gamma_2 = \Psi_{,12}$ and $\kappa = (\Psi_{,11} + \Psi_{,22})/2$, where $\Psi_{,12} = \partial_x \partial_y \Psi$; from these the magnification can be calculated as $\mu = \left[(1-\kappa)^2 - \boldsymbol{\gamma}^2\right]^{-1}$.

Using the SPL kernel for the shear from Aubert et al. (2007) we get the kernel for the variance of the two components of the of the shear $\boldsymbol{\gamma} = (\gamma_1, \gamma_2)$,

$$\boldsymbol{W}_{\sigma_\gamma^2}(r, l_p) = \frac{m_p^2 G^2}{\Sigma_c^2 \pi^2 r^8} \left\{ \frac{r^2}{2l_p^2} + [1 - G(r_p, l_p)] \right\}^2 \begin{pmatrix} (x^2 - y^2)^2 \\ 4x^2 y^2 \end{pmatrix} \tag{2.7}$$

where $G(r_p, l_p) = \exp\left[-r^2/\left(2l_p^2\right)\right]$ and $r^2 = x^2 + y^2$. We use this kernel to calculate the variance of the two shear components, $\boldsymbol{\sigma}_\gamma^2 = \sum_{i=1}^{N_{\rm part}} \boldsymbol{W}_{\sigma_\gamma^2}(\boldsymbol{x}_i - \boldsymbol{x}, l_i)$. Due to the term G^2, the support of the kernel (2.7) is more compact than the Gaussian smoothing kernel. Therefore Eq. (2.7) can be easily evaluated by direct numerical summation. This provides a fast and easy way to calculate the particle noise on the two shear components.

Taylor expanding the inverse of the magnification allows us to derive the noise on the inverse of the magnification due to noise on $\boldsymbol{\gamma}$ and κ,

$$\sigma_{\mu^{-1}}^2 = 4(1-\kappa)^2 \sigma_\kappa^2 + 4\gamma_1^2 \sigma_{\gamma_1}^2 + 4\gamma_2^2 \sigma_{\gamma_2}^2 \tag{2.8}$$

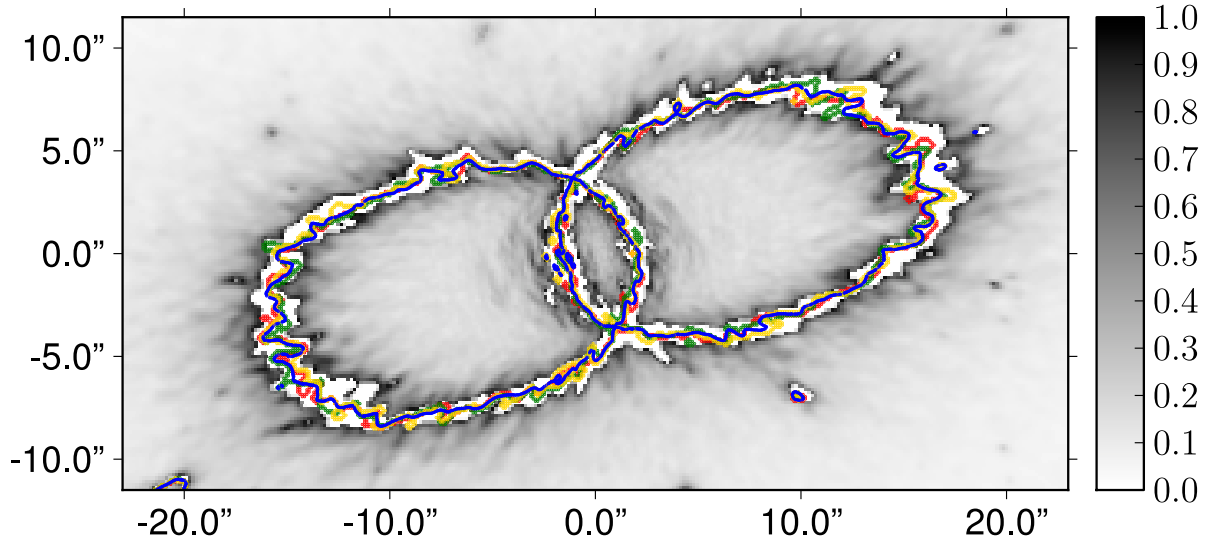

Figure 2.3: Critical lines for different particle noise realisations of the cluster. Background in grey scale is the particle noise of the inverse of the magnification $3\sigma_{\mu^{-1}}/|\mu^{-1}|$. The noise on the inverse of the magnification is cut-off at $3\sigma_{\mu^{-1}} \sim |\mu^{-1}|$ (white band following the critical curves), this indicates the noise on the critical line.

As an example, Figure 2.3 shows the 3σ particle noise on the inverse of the magnification $3\sigma_{\mu^{-1}}/|\mu^{-1}|$ as a grey scale background. In order to enhance the effect, the noise level is set to white for all pixels where $3\sigma_{\mu^{-1}} > |\mu^{-1}|$ close to the critical line. This indicates the width of the ‘wiggles’ of the critical line due to discreteness noise in the region close to the critical line where $\mu^{-1} \to 0$. The critical lines for four random particle noise realisations of the numerical cluster are over plotted with coloured lines. The blue line is for the original N-body cluster E from the Level-2 Phoenix simulations. The discreteness of the particles in the simulation is especially important in the strongly magnified and highly nonlinear regime of the critical lines. Figure 2.3 demonstrates the magnitude of the effect that significantly shapes the critical lines, even for this high-resolution simulation. Multiple imaging caused by strong lensing also takes place in this highly magnified region. Highly magnified giant arcs follow to zeroth order the tangential critical lines. Observations of these giant arcs often show significant effects of lens substructure, as for example, in the clusters MACS 1206, Abell 383 or 370 (for example Umetsu et al. (2012); Newman et al. (2011); Richard et al. (2010)). Especially in this highly magnified region, the particle noise in N-body simulations of strong lensing introduces small-scale perturbations that could mimic effects of cluster substructure. Small-scale perturbations in the lens also cause higher order singularities such as swallowtails in the caustic structure. Even if the perturbation is not strong enough to cause an actual ‘bump’ in the image, highly resolved images should reveal subtle changes in the position of small-scale structure in the arc. We will quantify the the effect of the particle noise on the image surface brightness distribution in the following section.

2.4.5 Lensed Images of a Gaussian Source

In order to understand the effect of particle noise on the strongly gravitationally lensed images of a background source, we simulate a gravitational lens system by placing a source galaxy at $z = 2.0$ behind cluster E at Level-2 resolution, $(4.4'', 4.1'')$ away from the cluster centre in projection. The source has a Gaussian surface brightness distribution with a FWHM size of $0.51''$ and a peak surface brightness of 100. The resulting gravitationally lensed images are shown in the top left panel of Fig. 2.4. Multiple images of a background source form in regions of high magnification, where the effect of the particle noise, due to the discreteness of the N-body simulations, is the largest. It is very important, therefore, to understand how the noise on the cluster surface mass density and deflection angles is propagated to the lensed images. In the following, we quantify this noise from the bootstrapped re-samplings of the N-body particles (compare with Sec. 2.4), as well as from analytical approximations.

For each bootstrapped particle distribution i of the cluster lens, we calculate the deflection angles $\boldsymbol{\alpha}_i$ and use them to lens an identical source surface brightness distribution $\boldsymbol{s}$ for each bootstrap resampling of the lens. The corresponding images, $\boldsymbol{d}_i$, differ from each other because of the particle noise.

The lower left panel of Fig. 2.4 shows the standard deviation of 100 lensed images of the same background source calculated in the same way from 100 different bootstrapped cluster resamplings; the noise on the image brightness is as large as $\sim 10\%$ of the image surface brightness. The origin of the image brightness fluctuations due to the particle noise and their distribution can be understood qualitatively by considering the lens equation $\boldsymbol{y} = \boldsymbol{x} - \boldsymbol{\alpha}(\boldsymbol{x})$. According to this equation, each point $\boldsymbol{x}$ on the lens plane is deflected by a deflection angle $\boldsymbol{\alpha}$ to a point $\boldsymbol{y}$ on the source plane. As shown in Sec. 2.4.3, the noise associated with the discrete particle distribution is responsible for local fluctuations on the gravitational potential $\psi(\boldsymbol{x})$ of the lensing cluster and therefore on the deflection angles $\boldsymbol{\alpha} = \nabla\psi(\boldsymbol{x})$. The noise on the lensed images is then just the effect of the particle noise on the cluster surface mass density propagated to the images via the deflection angles. From the left bottom panel of Fig. 2.4, it is clear that a large number of realisations is needed in order to reduce the statistical error of the bootstrap noise estimation. More quantitatively, we can extend the analytic noise analysis of the deflection angles in Sec. 2.4.3 to the noise on the simulated images, by linearizing the lens equation and approximating the difference in the surface brightness between two images $\delta\boldsymbol{d}$ by (Koopmans (2005)),

$$\delta\boldsymbol{d} \approx -(\delta\boldsymbol{\alpha}_x\, \partial_x \boldsymbol{s} + \delta\boldsymbol{\alpha}_y\, \partial_y \boldsymbol{s}). \tag{2.9}$$

For a given source surface brightness distribution, fluctuations in the image surface brightness are a linear combination of the fluctuations in the deflection angles. The bottom right panel of Fig. 2.4 shows this approximation for the noise on the images using the noise on the deflection angles. If we compare the two lower panels of Fig. 2.4, we see that this linearization overestimates the noise where the noise is high. From the above equation, we also expect the noise to follow the distribution of the gradient of the source surface brightness. In particular, small changes in the deflection angles can be strongly amplified if the gradient of the source surface brightness distribution is large. In Sec. 2.4.6, we discuss the effect of particle noise for a source surface brightness distribution with varying level of smoothness.

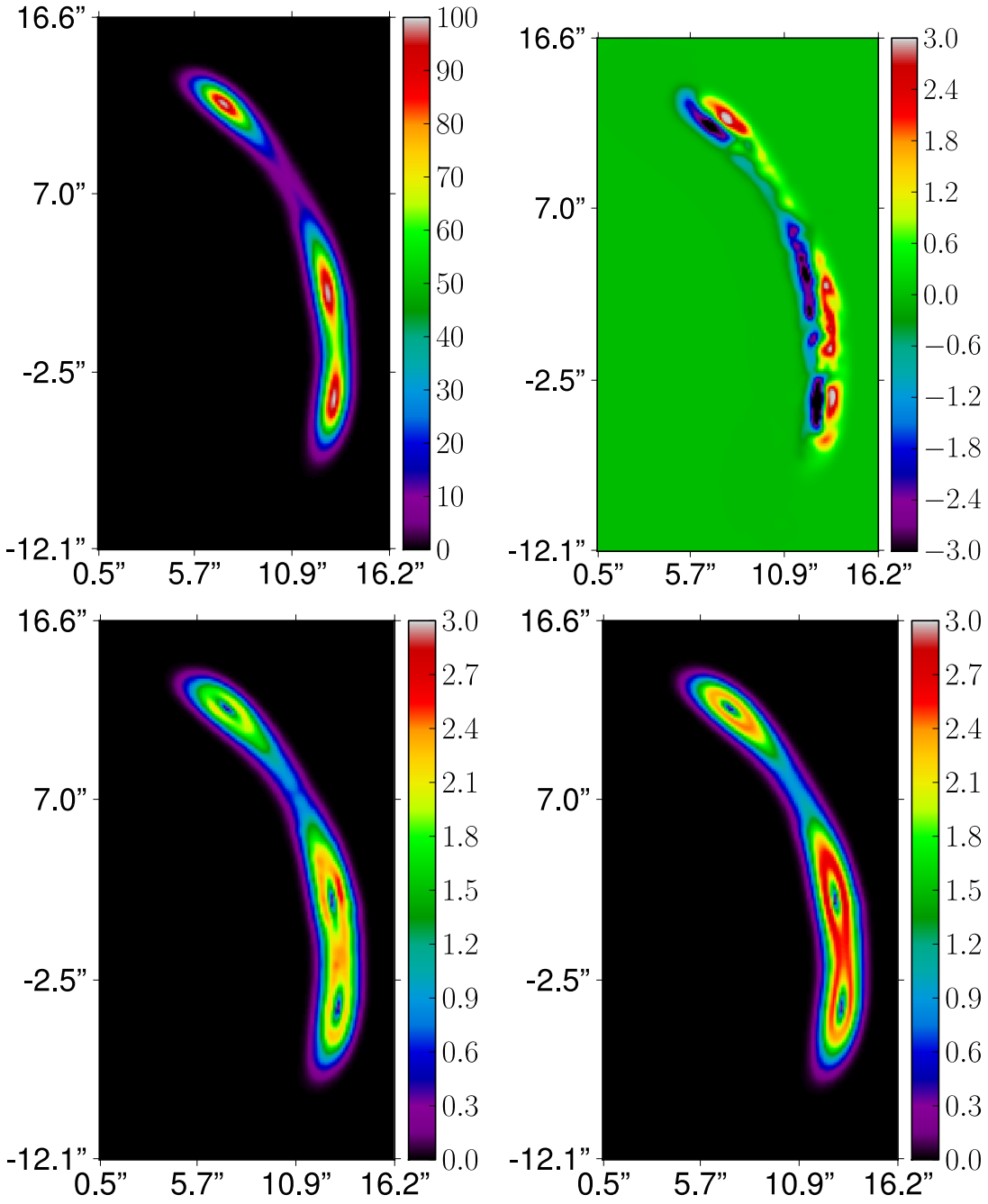

Figure 2.4: Image of a Gaussian source (top left) using the N-body cluster, brightness difference of two bootstrapped realisations (top right), standard deviation of 100 resamplings (bottom left) and analytic approximation using the noise of the deflection angles and a linearization of the lensing equation (bottom right).

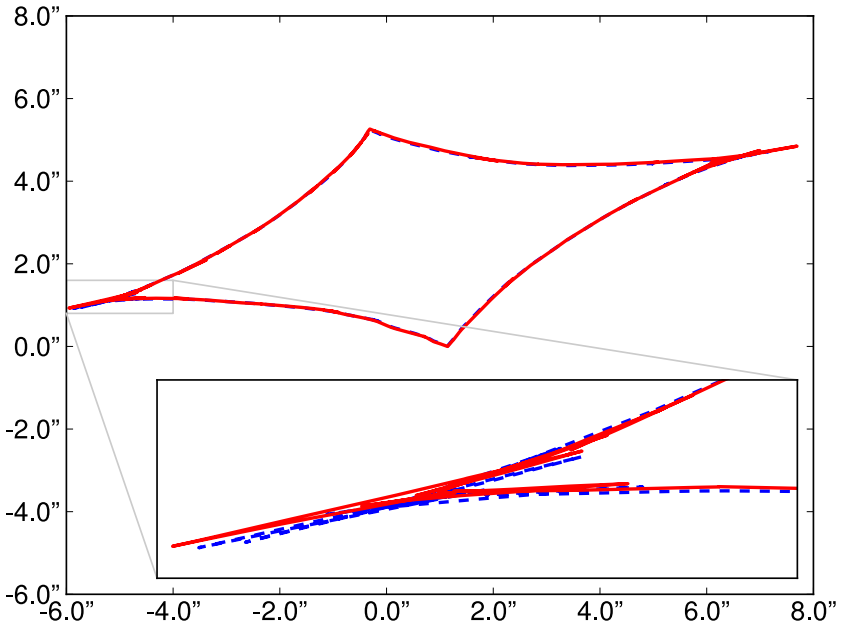

Figure 2.5: Caustics of two different particle noise realisations. Due to long-scale correlations of the deflection angles (cf. Fig. 2.2) and the finite size of the image, random particle noise will result in a shift of the caustic.

The top right panel of Fig. 2.4 shows the difference in brightness $\boldsymbol{d}_0 - \boldsymbol{d}_1$ for each pixel of the image plane, as an example, for two particular cluster re-samplings $i = 0$ and $i = 1$. The observed surface brightness difference can be attributed mainly to two effects: A global shift to the left by $< 0.1''$ of $\boldsymbol{d}_1$ relative to $\boldsymbol{d}_0$, and smaller scale differences. We start by discussing the origin of this global shift. We will see in the following that this shift is equivalent to an unobservable shift of the caustic relative to the source. We will therefore present a method to separate and subtract the contributions of this shift to the noise on the image brightness later on in this section.

2.4.5.1 Global shift of the lensed images

Although, small scale fluctuations of the lensed images can be significant, an overall shift in the image position also contributes significantly to the difference between two bootstrapped images. In the following, we shall discuss the differences in the deflection angles and the caustic structure between two re-samplings in more detail. This will help us to eliminate most of the brightness difference in the top right panel of Fig. 2.4 by a relative source - caustic shift, and will provide a more physical and observationally motivated measure for the noise on numerically lensed images.

In the left panel of Fig. 2.2, the difference between two deflection angle maps calculated from two bootstrapped clusters is shown. The size of a typical image, as for example in the top left

panel in Fig. 2.4 is marked as a rectangle. Because of the finite size of the area covered by an image on the lens plane and because of the long scale noise correlations on $\boldsymbol{\alpha}$, the mean of the noise realisation of the deflection angles within the area covered by the image is positive. This positive deviation of the deflection angles, also visible as a global shift of the caustic structure (see Fig. 2.5), will then result in a mean shift of the lensed images, or equivalently of the source on the source plane. Therefore, while a mean constant additional deflection angle does not change any of the physical parameters of the lens, it changes the relative position of the caustic and the (arbitrarily fixed) source.

2.4.5.2 Small scale surface brightness fluctuations

Any shift of the caustic position can be compensated by shifting the source position accordingly. Therefore, a simple shift in the source position eliminates most of the image brightness difference in the top right panel of Fig. 2.4. In the previous section we therefore made an assumption. We used an identical source for the shifted and the not-shifted caustic structure and we therefore compared two non-equivalent images.

Following a similar chain of argument, it is possible that the re-sampled cluster deflection angles will differ in higher order derivatives of the deflection angles as well, such as magnification, shear or flexion or more likely, a combination of all of those. Since none of the sources intrinsic properties such as position, size or morphology are known, we will assume in the following as little as possible about the source. The method described below is closer to an observational point of view and only constrains the source by its regularity. We therefore rephrase the problem of the comparison of two equivalent images as follows. Two deflection angle maps are given and the first of the two images is fixed as reference image. What is the most similar image we can find using the second deflection angle map, if we are only allowed to use a relatively regular source?

This question can be more easily answered within a Bayesian formulation of gravitational lensing. We try to find the closest image $\boldsymbol{d}_1$, to a reference image $\boldsymbol{d}_0$ under some regularity conditions. For a given, fixed smoothness of the source it is in general not possible to perfectly recreate the input image $\boldsymbol{d}_0$ exactly using the deflection angles $\boldsymbol{\alpha}_1$ and a smooth source $\boldsymbol{s}_1$. It is, however, possible to reconstruct a close image $\boldsymbol{d}_1$. We will try to find the best reconstructed image $\boldsymbol{d}_1$, which is as close as possible to the input image $\boldsymbol{d}_0$, and at the same time keeping its source $\boldsymbol{s}_1$ regular. Our source reconstruction is pixelized on a non-regular triangulation and the smoothness is only constrained by a curvature regularisation (Vegetti & Koopmans (2009)). For a given input image $\boldsymbol{d}_0$ we maximize the Bayesian posterior

$$\log P(\boldsymbol{s}_1|\boldsymbol{d}_0, \boldsymbol{\alpha}_1, \lambda, \boldsymbol{H}_s) = \chi^2 + \lambda_s^2 ||\boldsymbol{H}_s \boldsymbol{s}_1||_2^2 \tag{2.10}$$

where χ^2 is between both images, $\boldsymbol{H}_s$ is the form and λ_s the strength of the regularisation of the source. We assume a quadratic Gaussian prior for the regularisation which is centred at $\boldsymbol{s} = 0$. The regularisation strength λ_s is found self consistently from the data themselves by maximising

the posterior

$$P(\lambda_s|\boldsymbol{d}_0, \boldsymbol{\alpha}_1, \boldsymbol{H}_s) = \frac{P(\boldsymbol{d}_0|\lambda_s, \boldsymbol{\alpha}_1, \boldsymbol{H}_s)P(\lambda_s)}{P(\boldsymbol{d}_0|\boldsymbol{\alpha}_1, \boldsymbol{H}_s)}$$
$$\propto \int \mathrm{d}\boldsymbol{s}_1 \, P(\boldsymbol{d}_0|\boldsymbol{s}_1, \lambda_s, \boldsymbol{\alpha}_1, \boldsymbol{H}_s)P(\boldsymbol{s}_1|\boldsymbol{\alpha}_1, \boldsymbol{H}_s). \tag{2.11}$$

Here we assume a prior $P(\lambda_s)$ which is flat in $\log \lambda_s$. This method uses minimal assumptions about the source to find the best matching image for an input image. The pixelized brightness difference $\boldsymbol{d}_0(\boldsymbol{x}) - \boldsymbol{d}_1(\boldsymbol{x})$ of the reconstruction is shown in the top left panel of Fig. 2.6 for the same example as in the top right panel of Fig. 2.4. The image brightness fluctuations reflect the superposition of the effects of the individual random particle noise fluctuations on the surface mass density. This superposition is very nonlinear in the strong lensing regime. The top left panel of Fig. 2.6 shows the change in the morphology of the image surface brightness distribution due to a random field of small-scale noise substructures.

This method automatically corrects for the shift in the deflection angles or in the caustic in Fig. 2.5 and compares images produced by equivalent sources. The surface brightness difference between the two sources is shown in the top right panel of Fig. 2.6. As explained above, the reconstructed source is automatically shifted by the algorithm in order to find an equivalent source which now reproduces the reference image as well as possible. By applying this method to $N_\mathrm{b} = 100$ bootstrapped cluster resamplings we simulate the particle noise on the pixelized image brightness distribution, $\boldsymbol{\sigma}^2_{\boldsymbol{d}}(\boldsymbol{x}) = 1/(N_\mathrm{b}-1)\sum_{i=1}^{N_\mathrm{b}}(\boldsymbol{d}_0 - \boldsymbol{d}_i)^2$. The noise is shown in the bottom left panel of Fig. 2.6. By allowing the algorithm to automatically adapt the source, the noise on the images is reduced by a factor of two. In other words, half of the noise on the image brightness in the lower left panel of Fig. 2.4 can be attributed to a simple relative shift of the source to the caustic between different bootstrap realisations. The sharp cuts at the top and the bottom of the arc in the lower left panel of Fig. 2.6 are due to the caustic structure. The single imaged regions of the source are less noisy by a factor of ~ 100 than the threefold imaged parts. The reconstruction algorithm for the source can more easily fit the single-imaged regions than the threefold imaged parts of the brightness distribution. Therefore, the noise is not visible in these regions in Fig. 2.6. If we assume that the Bayesian source reconstruction mainly corrects for the source shift, we also can approximate this noise analytically. Shifting the source keeps the gradient of the source $\nabla \boldsymbol{s}$ constant on the image plane. But we have to correct the deflection angles by the mean source shift, effectively calculating $\delta\boldsymbol{d} \approx -(\delta\boldsymbol{\alpha} - \langle\delta\boldsymbol{\alpha}\rangle)\nabla\boldsymbol{s}$ where the mean $\langle\delta\boldsymbol{\alpha}\rangle$ is evaluated over the size of the images. The bottom right panel of Fig. 2.6 shows the corrected version of the linear noise approximation for the image brightness. Even though this is a very simplified and fast approximation to the noise, the result is very close to the accurately simulated noise.

2.4.6 Lensed Images of a Realistic Source

The noise on the surface brightness distribution of the lensed images only weakly depends on the image position, but it strongly depends on the source gradient. This can be understood from the

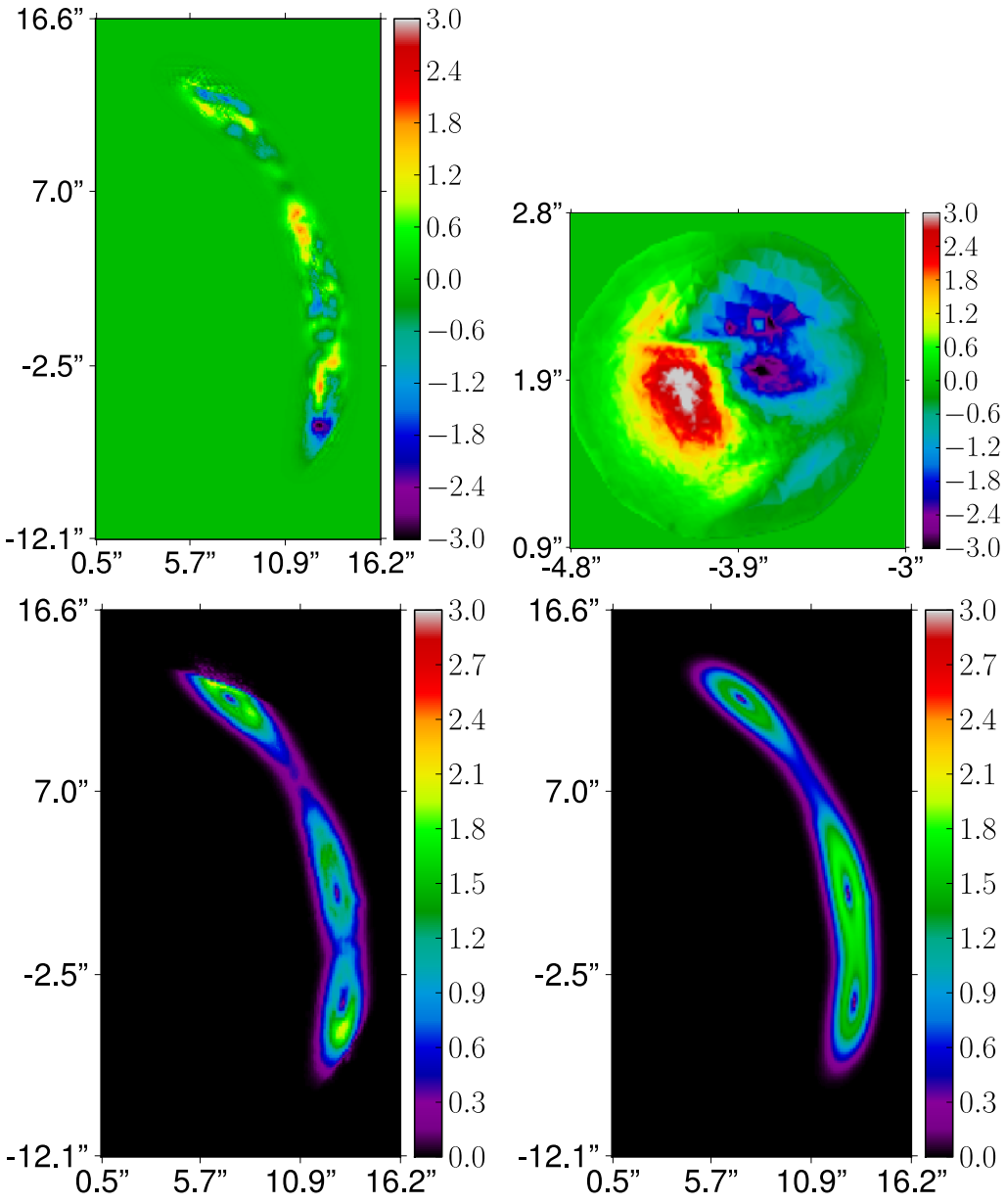

Figure 2.6: Difference in the image brightness using a Bayesian source reconstruction (top left panel), colorscale identical to Fig. 2.4 top right panel. Difference between original source and reconstructed source shows that the biggest effect is a shift in position (top right panel). Standard deviation of 100 bootstrapped realisations of the N-body cluster, for each cluster the best image matching an input image is found (bottom left panel). Standard deviation approximation with analytic formula using σ_α and a linearization of the lensing equation (bottom right panel).

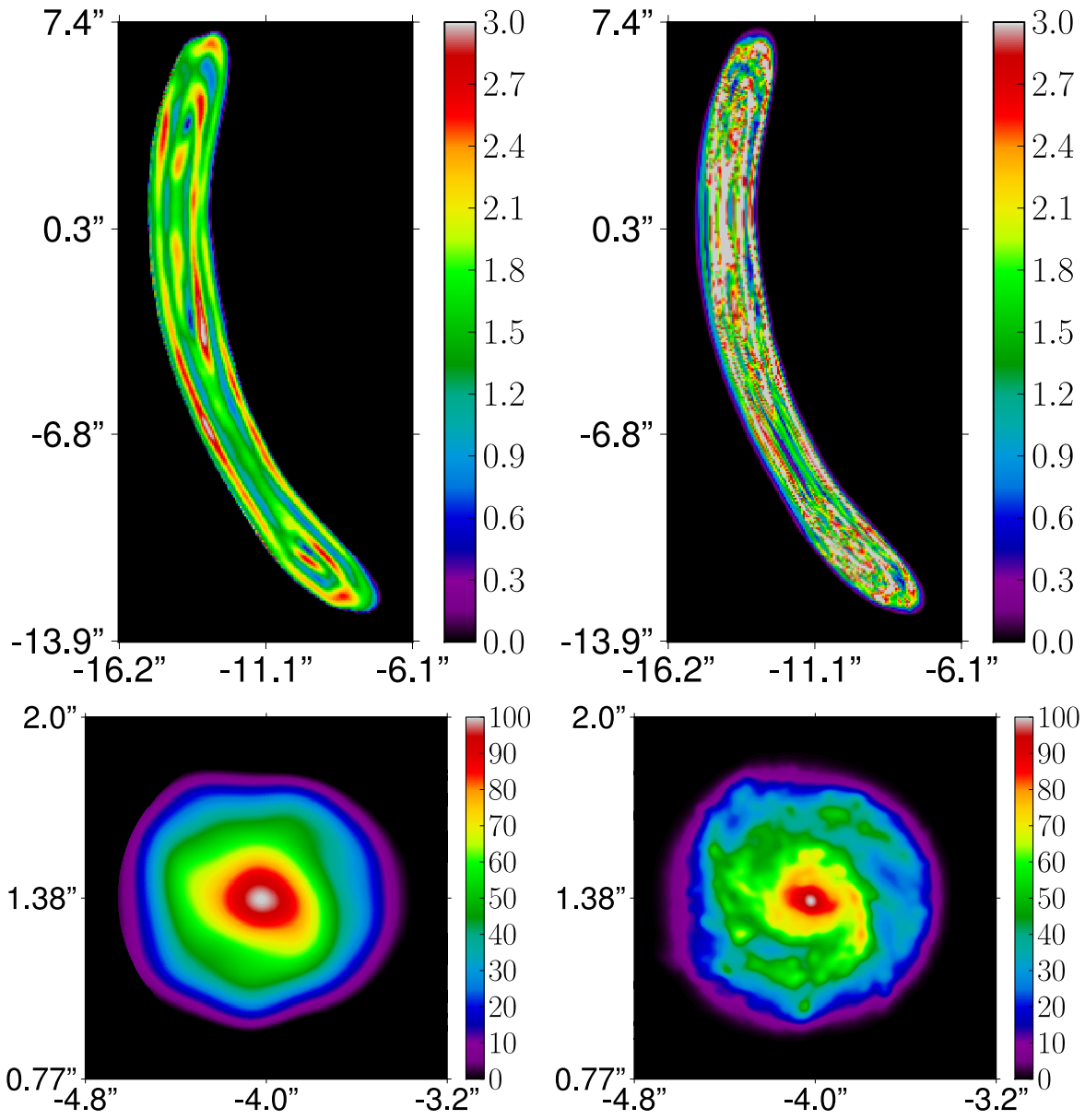

Figure 2.7: Same as the bottom left panel of Fig. 2.4 but for a different source position and the source brightness distributions in the bottom panels. An increased structure of the source and therefore an increased source gradient increases the noise on the image brightness.

analytical approximation in Eq. 2.9, since the noise on the deflection angles in the top right panel of Fig. 2.2 is very smooth in the region where strongly magnified images occur at $x \approx \pm 15''$. As an example we show the different noise maps of the image brightness in the top panels of Fig. 2.7 for two more structured sources. The respective sources are shown in the lower panels. Both sources are located at $(-4'', 1.38'')$, the FWHM size is the same as the Gaussian source in Fig. 2.4, $0.51''$, and the maximum brightness is scaled to 100. The source on the left is a smooth version of the right source. The magnitude of the noise in the top left panel is similar to the noise on the image for a Gaussian source. This can be seen by comparing Fig. 2.7 to the lower left panel of Fig. 2.4. The distribution of the noise follows that of the source gradient on the lens plane. The more irregular source in the right panel also shows a significantly increased noise. This dependence is easily understood from the linearization in Eq. 2.9.

2.5 Noise Scaling

In the previous sections, we have calculated the particle noise due to the discreteness of the N-body simulation on different lensing properties. The results were calculated for a simulation with $N_{\rm part}$ particles and a 3D adaptive smoothing algorithm that adapts the smoothing length for each particle to the distance of its $N_{\rm ngb}$-th neighbour in 3D. In this section, we will derive how the particle noise in the simulation of gravitational lensing changes as a function of particle number $N_{\rm part}$ and the number of smoothing neighbours $N_{\rm ngb}$. Increasing the number of particles inside the smoothing kernel, $N_{\rm ngb}$, will result in a more smoothed mass distribution and therefore reduced noise on all of the lensing properties. It will, however, also smooth out the physical substructures that were part of the simulation. Increasing the particle number while keeping the number of neighbours constant will increase the mass resolution of the simulation and therefore also reduce the noise, at the cost, however, of the computational load.

In principle, we could numerically simulate a change in $N_{\rm part}$ and $N_{\rm ngb}$ by resampling the mass density and then re-calculate the smoothing length for each particle and all of the lensing properties for each of the re-projections of the 3D particle distributions. In practice, we develop a method that allows us to convert the 3D adaptive smoothing lengths into 2D smoothing lengths and derive analytic expressions for the scaling of the noise in 2D, while preserving the information of the 3D particle density distribution.

2.5.1 Smoothing in 2D

Until now we calculated the noise on all of the lensing properties from the 3D particle distribution and we used a smoothing length that was adaptive with the 3D particle density distribution. We will now introduce an approximation that allows us to keep most of the 3D information, while performing the noise calculations in 2D. The 2D version obviously increases the speed of the calculations substantially, and it also allows us to derive the scaling properties of the noise on the surface mass density and the deflection angles with the particle number and the number of smoothing neighbours.

By comparing Eqs. (2.5) and (2.3), we find that on average, on scales larger than the smoothing length l_i of each particle, the contribution of each particle i to the variance of the surface mass density, σ^2_Σ, and to the surface mass density, Σ, differs by a factor of

$$f_i \propto \frac{\int W(l_i)\mathrm{d}^2\boldsymbol{x}}{\int W^2(l_i)\mathrm{d}^2\boldsymbol{x}} = \frac{9}{5\pi l_i^2}. \tag{2.12}$$

The constant factor $9/(5\pi)$ depends weakly on the form of the smoothing kernel. Here, we used the kernel $W \propto (1 - r^2/l^2)^2$ for $r \leq l$, for details and other kernels see also Appendix 2.9. Eq. (2.12) states that smaller particles from high-density regions contribute proportionally with a factor of $1/l^2$ to the variance of the surface mass density. We can use this information to derive a 2D approximation to the noise on the surface mass density. To this end, we define an effective smoothing length, $l_{\mathrm{eff}}\,(\boldsymbol{x})$ in 2D, which is a integrated average of all line of sight N-body particles,

$$l_{\mathrm{eff}}\,(\boldsymbol{x}) = \left(\frac{1}{N_z}\sum_{i=1}^{N_z}\frac{1}{l_i^2}\right)^{-1/2} \tag{2.13}$$

This allows us to assign a single smoothing length to a particular 2D position on the lens plane, and simultaneously taking into account the 3D density distribution. Note that, in the limit of an extremely high-resolution grid on the lens plane and a finite N-body particle number, not all positions will be occupied, and $l_{\mathrm{eff}} = l$. With this simplification we are able to approximate the variance of the surface mass density of Eq. (2.5), in terms of the 2D surface mass density Σ,

$$\sigma^2_\Sigma\,(\boldsymbol{x}) \approx \frac{9}{5\pi}\frac{m_p}{l^2_{\mathrm{eff}}\,(\boldsymbol{x})\,A}\Sigma\,(\boldsymbol{x})\,. \tag{2.14}$$

2.5.2 Noise in 2D

In this section, we introduce some useful expressions for the noise on the lensing properties using the 2D smoothing approximation derived above. This will simplify the derivation in the next section and will allow us to calculate the noise on a high-resolution grid in a fast and easy way, by eliminating the need for a tree-based evaluation of the long-range terms of the deflection angles (e.g. the $1/r^2$ dependence of the variance).

We start by considering the definition of the effective smoothing length for each point on the lens plane $l_{\mathrm{eff}}\,(\boldsymbol{x})$ as presented in Eq. (2.13). This smoothing length defines the correlation length of the noise for each point in 2D. All we need for the first order covariance matrix is the amplitude of the uncorrelated noise $\tilde{\sigma}_\Sigma$ at each point on the lens plane, which can be calculated from the correlated noise in Eq. (2.5). In other words, the correlation introduced by smoothing the original N-body particles with a smoothing kernel of size l_{eff} has decreased the uncorrelated noise to the expression given in Eq. (2.5). By deconvolving each point on the lens plane with a smoothing kernel of size l_{eff}, the correlated noise, σ^2_Σ, is increased again by

$$\tilde{\sigma}^2_\Sigma\,(\boldsymbol{x}) = \frac{5\pi l^2_{\mathrm{eff}}}{9}\sigma^2_\Sigma\,(\boldsymbol{x})\,, \tag{2.15}$$

as demonstrated in the Appendix 2.9. In order to obtain the uncorrelated noise amplitude, $\tilde{\sigma}_\Sigma$, we therefore have to increase the noise from Eq. (2.5).

These considerations allow us to simulate the effect of the particle noise on the lensing properties with a 2D convolution. For the variance we obtain the following expression,

$$\sigma_Y^2(\boldsymbol{x}) = \int \mathrm{d}^2\boldsymbol{x}' \tilde{\sigma}_\Sigma^2(\boldsymbol{x}')\, W_{\sigma_Y^2}(|\boldsymbol{x}-\boldsymbol{x}'|, l_{\mathrm{eff}}) \tag{2.16}$$

and for a single particle noise realisation,

$$\Delta Y(\boldsymbol{x}) = \int \mathrm{d}^2\boldsymbol{x}' R(\boldsymbol{x}', \tilde{\sigma}_\Sigma)\, W_Y(|\boldsymbol{x}-\boldsymbol{x}'|, l_{\mathrm{eff}}), \tag{2.17}$$

where $Y \in \{\kappa, \boldsymbol{\alpha}, \boldsymbol{\gamma}\}$, $W_Y(|\boldsymbol{x}-\boldsymbol{x}'|, l_{\mathrm{eff}})$ is the appropriate kernel and $R(\boldsymbol{x}', \tilde{\sigma}_\Sigma)$ is a random number drawn from a Gaussian distribution with standard deviation $\tilde{\sigma}_\Sigma$. Eq. (2.17) can be understood as placing uncorrelated particles of size l_{eff} with random mass $R(\boldsymbol{x}', \tilde{\sigma}_\Sigma)$ at the 2D positions $\boldsymbol{x}'$.

2.5.3 Scaling with N_{part} and N_{ngb}

With this effective 2D formulation of the adaptive 3D smoothing we can study the scaling of the noise. An increased resolution of a N-body simulation samples the density with more particles of smaller masses. This increase in particle number also decreases the particle noise due to the finer discrete sampling. With an increased particle number, the number density of particles in 3D is also increased. Therefore the size of the smoothing kernel, which here is the distance to the N_{ngb}-th neighbour, also changes. From Eq. (2.14) we calculate the scaling of the noise on the surface mass density between different resolutions k and j of a N-body simulation as

$$\left(\frac{\sigma_\Sigma^j(\boldsymbol{x})}{\sigma_\Sigma^k(\boldsymbol{x})}\right)^2 = \frac{m^j}{m^k}\left(\frac{l^k(\boldsymbol{x})}{l^j(\boldsymbol{x})}\right)^2. \tag{2.18}$$

If all particles have the same mass, then the fractional change in particle mass is equal to the inverse change in particle number, $m^j/m^k = N_{\mathrm{part}}^k/N_{\mathrm{part}}^j$. The change in the smoothing of the particles, l, can be estimated from the change in particle number and the change in the number of neighbours by

$$\frac{l^k(\boldsymbol{x})}{l^j(\boldsymbol{x})} = \frac{l^k}{l^j} \approx \sqrt[3]{\frac{N_{\mathrm{ngb}}^k N_{\mathrm{part}}^j}{N_{\mathrm{ngb}}^j N_{\mathrm{part}}^k}} \tag{2.19}$$

With these two scalings, the fractional change in the noise of the surface mass density in Eq. (2.18) simplifies to

$$\left(\frac{\sigma_\Sigma^j}{\sigma_\Sigma^k}\right)^2 = \left(\frac{N_{\mathrm{part}}^k}{N_{\mathrm{part}}^j}\right)^{1/3}\left(\frac{N_{\mathrm{ngb}}^k}{N_{\mathrm{ngb}}^j}\right)^{2/3} \tag{2.20}$$

This first result allows us to estimate the change in the variance of the surface mass density with changing particle number of the simulation and a changed smoothing length to convert the N-body particles into lensing properties.

We can transform Eq. (2.14) to

$$\frac{\sigma_\Sigma^2(\boldsymbol{x})}{\Sigma^2(\boldsymbol{x})} \approx \frac{9}{5\pi}\frac{m_p}{l^2(\boldsymbol{x})\,A}\frac{1}{\Sigma(\boldsymbol{x})}. \tag{2.21}$$

For the special case of a uniform density field in 3D with equally distributed particles, the mean projected 2D surface mass density is $\bar{\Sigma} = m_p N_{\rm part} A/L^2$, where L is the side length of the cube of equally distributed particles. For this configuration, the distance l to the $N_{\rm ngb}$-th neighbour can be calculated from

$$\frac{l}{L} = \left(\frac{N_{\rm ngb}}{N_{\rm part}}\right)^{1/3}. \tag{2.22}$$

Substituting these two relations into Eq. (2.21) we obtain in units of the critical density $\Sigma_{\rm crit}$, the following relation

$$\frac{\sigma_\kappa(\boldsymbol{x})}{\bar{\kappa}(\boldsymbol{x})} = \sqrt{\frac{9}{5}}\frac{1}{N_{\rm ngb}^{1/3} N_{\rm part}^{1/6}} \tag{2.23}$$

which is similar to what (Li et al. (2006)) found by numerical fitting (their Eq. (4)). The exact value of the proportionality constant depends on the exact form of the kernel.

2.6 Comparison of the Particle Noise with Substructure

In this second part of the paper we compare the small-scale fluctuations due to two competing effects, the particle noise and physical mass substructures (subhalos). In particular, we are interested in quantifying the limit at which the effect of physical mass substructure becomes comparable to that of particle noise, and the substructure is considered too 'small' to be 'visible' above the noise level. To this end, we need quantitative measures of the effect of a substructure on the lensing properties. Mainly, we need a metric to answer the following questions: which lensing property is best to look at in order to compare the substructure to the noise? Which property of the substructure is the best one to quantify how 'small' a substructure is? When can a substructure be considered 'visible' above the noise level?

Substructures in our N-body simulation are identified as gravitationally bound objects consisting of more than $N_{\rm min} \sim 20$ particles. For each substructure we can measure, among other parameters, its mass, size, ellipticity, density profile and circular velocity. For a simplified substructure model such as a singular isothermal sphere (SIS), the lens strength b is proportional to the Einstein radius which is proportional to the one-dimensional velocity dispersion σ_v^2. The mass within R on the other hand is proportional to $\sigma_v^2 R$. Therefore we choose the quotient of the mass of the substructure and its half-mass radius in units of the critical density, $\beta = M_{\rm ss}/R_{\rm HMR}/\Sigma_{\rm crit}$ as a measure of the strength of each substructure. We will confirm in Sec. 2.6.2 that this measure derived from a simplified SIS model is a good parameter to quantify the effect of the numerically simulated substructures.

For the convenience of the reader we will also introduce a second x-axis on the top of Figs. 2.9 to 2.13. This second axis converts the lens strength on the bottom x-axis to a typical substructure

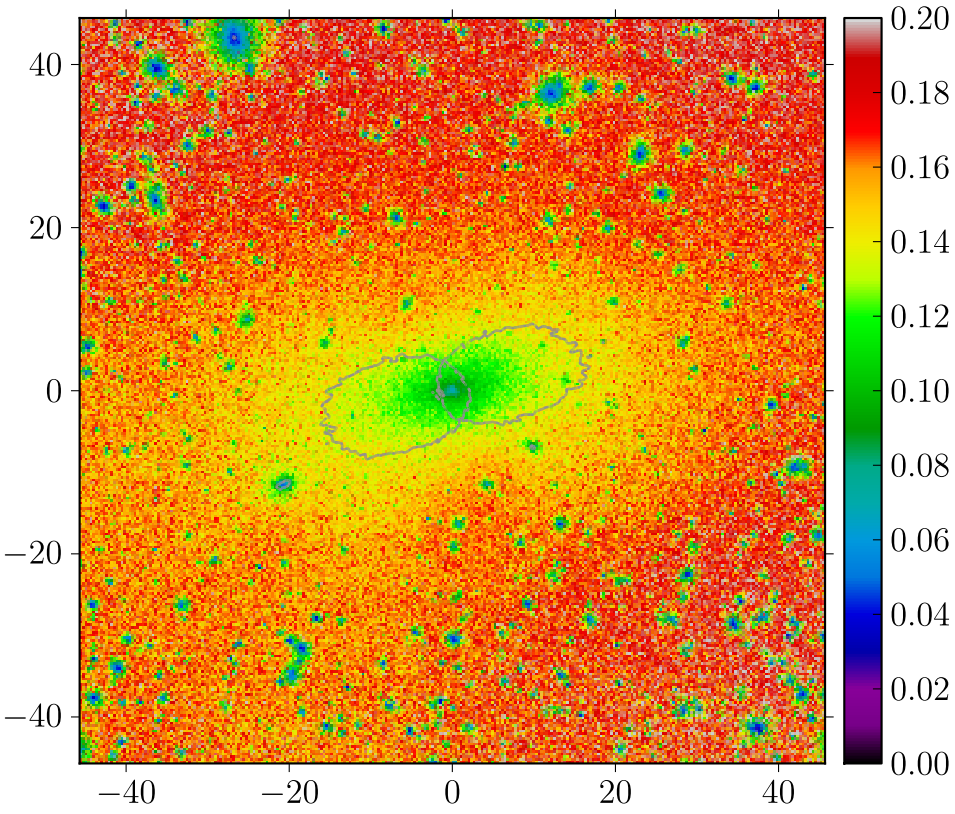

Figure 2.8: Approximation of the lens strength β of Gaussian noise with the same parameters as the noise on the surface mass density for the Level-2 version of cluster E. At the critical lines the lens strength of the 3σ noise is $\beta \sim 0.14$.

mass, $M_{\rm ss}$. The conversion is a linear fit to all numerically simulated substructures as identified by SUBFIND within the Level-2 simulation of cluster E in $\log(M_{\rm ss})$-$\log(\beta)$ space within $-2 < \log_{10}\beta_{\rm ss} < 0$. This corresponds roughly to $0.03 < M_{\rm ss}/(10^{10}{\rm M}_\odot) < 7$. The linear fit, $\log(M_{\rm ss}/(10^{10}{\rm M}_\odot/h)) = 1.21^{\pm 0.01}\log_{10}(\beta_{\rm ss}/'') + 0.71^{\pm 0.02}$, averages different substructure profiles, sizes and concentrations and therefore yields a typical substructure mass for a given substructure lens strength. All calculations, however, are performed in terms of the substructure lens strength β in order to fully take into account the different 2D profiles of the simulated substructures.

2.6.1 Substructure Surface Mass Density

As a first, although very simple step, one might compare the projected scaled surface mass density of each substructure, κ_i, to the amplitude of the noise fluctuations of the surface mass density due to the particle noise, σ_κ. We approximate the noise by a Gaussian fluctuation field with amplitude σ_κ and a correlation length equivalent to the 2D smoothing length, $l_{\rm eff}$, at each point on

the lens plane. We can then calculate the equivalent lens strength for the noise fluctuations. The size of the Gaussian is $l_{\rm eff} = l$, the total mass of a $n\sigma$ noise substructure is therefore $\pi l^2 n \sigma_\Sigma$ for $n \in \{1, 2, 3\}$. The half mass radius is $R_{\rm HMR} = l\sqrt{2\ln 2}$. Therefore the equivalent lens strength is $\beta = M_{\rm ss}/(R_{\rm HMR}\Sigma_{\rm crit}) = \pi l \sigma_\kappa/(2\ln 2)$. Figure 2.8 shows the lens strength of the noise on the scaled surface mass density at each point on the lens plane. At the critical line, we therefore identify the substructures that will have a smaller influence than the 3σ noise as those substructures which are smaller than $\beta \sim 0.14$, this corresponds to an average subhalo mass smaller than $\mathrm{M_{ss}} \sim 6.5 \times 10^9 \mathrm{M}_\odot$.

By comparing the surface mass density, we are essentially comparing a single substructure with a random field of positive and negative substructures for the noise. Since the lensing equation is highly nonlinear, especially in the strong lensing regime, the noise also propagates nonlinearly through the lensing properties as we will show in the following sections. We can therefore not assume that the limits derived here based on the surface mass density are the true resolution limits of the simulation, in the sense that every lensing property yields identical limits.

2.6.2 Substructure Deflection Angles

As a second quantity, we compare the deflection angles of the substructures $\boldsymbol{\alpha}_{\rm ss}$ with the noise on the deflection angles due to the particle noise in the N-body simulation, $\sigma_{\boldsymbol{\alpha}}$. Although the deflection angles are not directly observable, we will show in this section that they are a good measure of the effect of a substructure.

We have already seen in Sec. 2.4.5, that the additional deflection caused by small-scale fluctuations due to the particle noise can be approximated as a small correction on top of the deflection by the numerical cluster. Any additional deflection $\Delta\boldsymbol{\alpha}$ will result in a change in the observable surface brightness of the image $\Delta\boldsymbol{d}$. In a simplified model where the source gradient is varying slowly, the greater the additional deflection $\Delta\boldsymbol{\alpha}$, the greater the change in the image brightness at that point (see Eq. (2.9)). Therefore we compare the additional deflection by a substructure, $\Delta\boldsymbol{\alpha}_{\rm ss}$, with the fluctuations in the deflection angles, $\sigma_{\boldsymbol{\alpha}}$ caused by the particle noise. We could also use an integrated measure over all points of the image plane, where the additional deflection by the substructure exceeds the magnitude of the fluctuations from the particle noise. Since the results are the same, we use here for simplicity only the maximum value of the additional substructure deflection, $\max[\Delta\boldsymbol{\alpha}_{\rm ss}(\boldsymbol{x})]_{\boldsymbol{x}}$ and compare it to $\sigma_{\boldsymbol{\alpha}}(\boldsymbol{x})$ due to the particle noise at the same point on the lens plane.

Figure 2.9 shows the maximum of the additional deflection for a subsample of the 2597 substructures in the central $(92'')^2$. The subsample is chosen to include the most massive substructures with the greatest lens strength. Each substructure is shown as a red circle for the Level-2 resolution. As a comparison, the subhalos of a second, lower resolution of the simulation, Level-4, are also shown as blue squares. We use the fully numerical substructures to calculate the total mass and half mass radius for the lens strength on the x-axis. The y-axis is the maximum of the additional deflection calculated numerically by solving the Poisson equation for each substructure. All subhalos fall almost perfectly onto the linear relation $y = 0.2272x$, therefore the parameter $M_{\rm ss}/(\Sigma_{\rm crit}R_{\rm HMR})$ is suitable to quantify the strength of the numerical substructures and the subsample of 400 subhalos is sufficient to quantify the the effects of the subhalo popula-

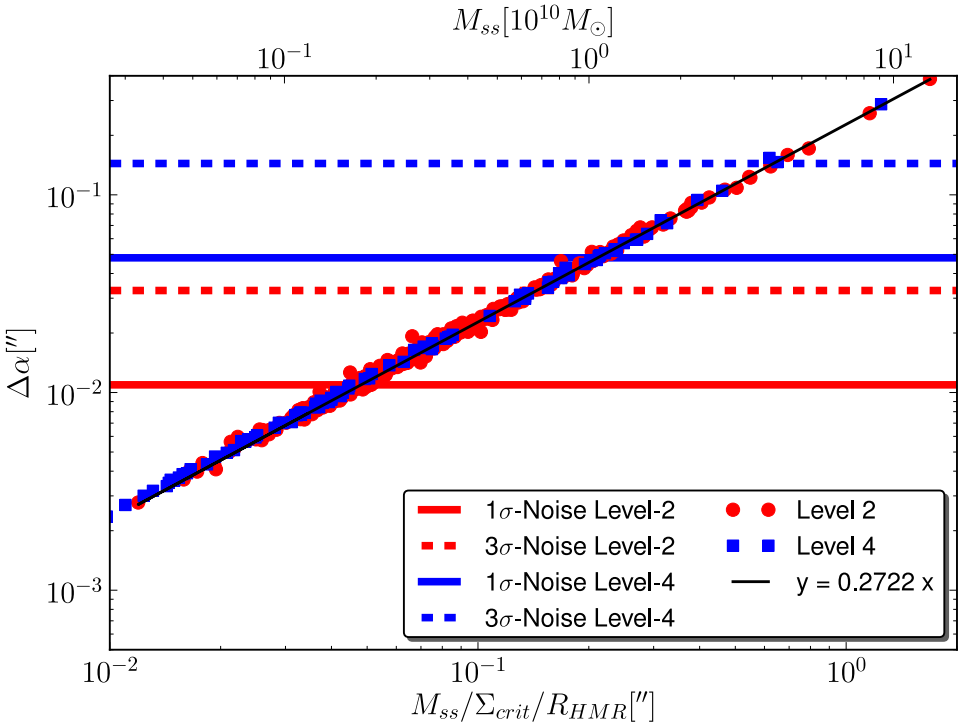

Figure 2.9: Maximum value of the additional deflection $\Delta\boldsymbol{\alpha}$ for substructures with positions within $(92'')^2$ from the centre for the populations Level-2 and Level-4 resolutions. Horizontal lines show the 1σ (solid lines) and the 3σ (dashed lines) noise at the position of the lowest image in the top left panel of Fig. 2.4 for Level-2 (red) and Level-4 (blue).

tion in Fig. 2.9. Now, we compare the maximum additional deflection caused by the individual substructures with the noise on the deflection angles from Sec. 2.4.3 as follows. We artificially place each of the substructures directly behind the lowest image at $(13'', -4'')$. Since the noise on $\boldsymbol{\alpha}$ is a very smooth function over the size of a typical image (see Fig. 2.2) we can use the same value $\sigma_{\boldsymbol{\alpha}}$ for all substructures. The noise on the deflection angles can therefore be represented by horizontal lines in Figure 2.9. A more rigorous approach would require to use the position of the respective maximum of the additional deflection for each substructure which varies slightly with the size of the substructure. Using the correct appropriate values of $\sigma_{\boldsymbol{\alpha}}$, however, does not alter the results. Under the assumption that a greater additional deflection by a substructure, $\Delta\boldsymbol{\alpha}_{\rm ss}$, also causes a more significant change in the image brightness, we define as visible substructure, those that are above the respective horizontal noise levels in Figure 2.9.

With this method we are able to constrain the 1σ 'visibility' of substructures to a substructure lens strengths of $0.048''$ $(1.7 \times 10^9 \mathrm{M}_\odot)$ for Level-2 and $0.21''$ $(1 \times 10^{10} \mathrm{M}_\odot)$ for Level-4 (solid lines). The respective 3σ limits are $0.14''$ $(6.5 \times 10^9 \mathrm{M}_\odot)$ and $0.62''$ $(3.9 \times 10^9 \mathrm{M}_\odot)$ (dashed lines). This simple comparison of the deflections by a substructure with the fluctuations in the deflection from the particle noise provides a fast measure of the detectability of a substructure. However, we

have to keep in mind that the deflection caused by substructures is only observable in combination with a lensed source. Moreover, only differences in the deflection can be measured through their effect on the shear, the magnification or the image brightness distribution. We show the effects on the inverse of the magnification in the next section. We will see in Sec. 2.6.4 that these results based on the deflection angles are almost identical to the analysis based on differences in the image brightness distribution.

2.6.3 Substructure Magnification

In this section, we compare the effect of mass substructure and particle noise on the inverse of the magnification μ^{-1} and on the critical lines. Both panels in Figure 2.10 show the particle noise on the inverse of the magnification $3\sigma_{\mu^{-1}}/|\mu^{-1}|$ as a grey scale background. The noise increases with the magnification and reaches its maximum at the critical lines. In order to indicate the width of the 3σ 'wiggles' in the critical line, values where the noise $3\sigma_{\mu^{-1}}$ exceeds $|\mu^{-1}|$ close to the critical curves are set to white. In the top panel, two critical lines, $\mu^{-1} \rightarrow 0$, are over plotted. The blue line is for the original N-body cluster E from the Level-2 Phoenix simulations. The red line is for the same cluster but with all subhalos identified by SUBFIND removed. The physical subhalos of the simulation are marked as coloured circles. The colour indicates the subhalo lens strength $\beta = M_{\rm ss}/R_{\rm HMR}/\Sigma_{\rm crit}$. The two critical lines are almost identical except for those few cases in which a subhalo lies directly on top of the critical line. The inset is showing an enlargement of three of these cases indicated by arrows. The masses of the three subhalos are 6.0 (green on the left), 2.9+0.7 (top middle, green+blue) and 8.4 (top right, light green) $\times 10^9 \mathrm{M}_\odot$. The influence of the two more massive subhalos in the inset with masses of 6.0 and 8.4 $\times 10^9 \mathrm{M}_\odot$, exceeds the 3σ noise of the critical line. It is evident from the critical line of the N-body cluster without any subhalos, that the curve still shows a lot of irregularities. Those wiggles are all a consequence of the particle noise due to the discrete N-body representation with finite size particles.

In order to study the influence of substructures of different sizes we could rotate the cluster, however, this would also change the overall shape of the critical lines and make the comparison between different substructure difficult to quantify. A better approach is then to artificially place additional substructures on top of the critical lines. In the bottom panel of Fig. 2.10 we quantify the effect of artificial substructures. We add the substructure particles of 11 substructures randomly chosen with decreasing lens strength on top of the particle distribution of the original N-body simulation at $(-15.6'', -2.6'')$. For each substructure we calculate the new critical lines and compare the deviation from the original critical line with the 3σ noise on the inverse of the magnification μ^{-1} in the lower panel of Fig. 2.10. Substructures smaller than $\beta \approx 0.1''$ are within the white band in the lower panel of Fig. 2.10. This limit corresponds to resolved minimum average subhalo mass of $\mathrm{M}_{\rm ss} \sim 4.3 \times 10^9 \mathrm{M}_\odot$. Any substructure bigger than this will cause a 'wiggle' in the critical line that is stronger than those caused by the numerical 3σ particle noise of the simulation.

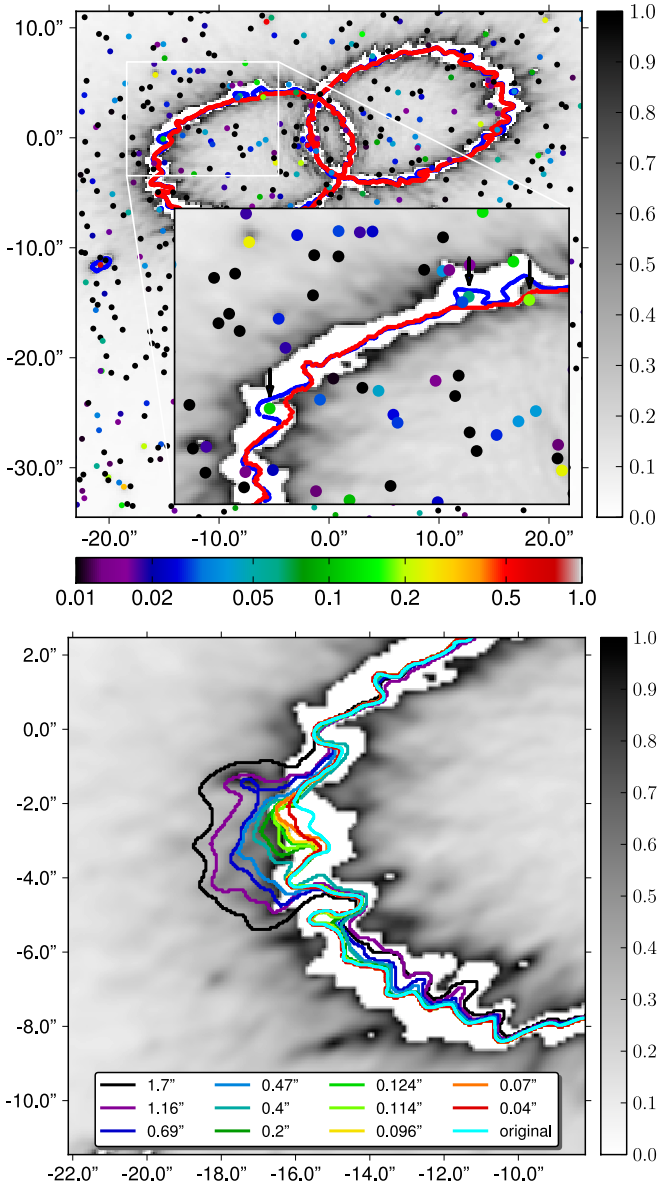

Figure 2.10: Top panel: Critical lines with (blue) and without (red) subhalos. Background in grey scale is the particle noise of the inverse of the magnification $3\sigma_{\mu^{-1}}/|\mu^{-1}|$. The noise on the inverse of the magnification is cut-off at $3\sigma_{\mu^{-1}} \sim |\mu^{-1}|$ (white band following the critical curves), this indicates the noise on the critical line. Coloured circles indicate substructures with masses in $10^{10}\mathrm{M}_{\odot}$. The inset shows an enlargement with the significant effect of three (four) subhalos directly on the critical line marked by arrows, for details see text. Bottom panel: 11 substructures of decreasing lens strength artificially added on top of the N-body cluster mass distribution at $-15.6'', -2.6''$. Substructures with a lens strength smaller than $\sim 0.1''$ are within the 3σ limits of the noise on μ^{-1} shown as a grey scale background.

2.6.4 Lensed images with Substructure of a Gaussian Source

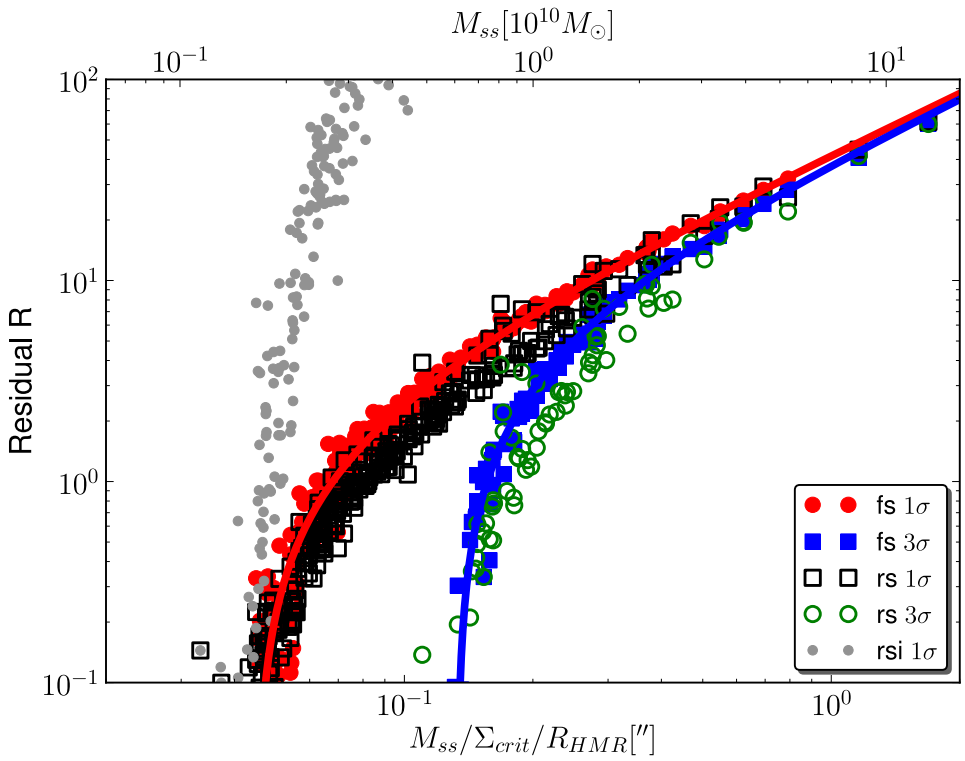

Figure 2.11: Residual R where $R = |\Delta \boldsymbol{d}| - n\sigma_{\boldsymbol{d}} > 0$, where the image brightness difference caused by adding a substructure is bigger than the particle noise induced brightness difference in the image. Shown is the maximum of R measured over all points on the lens plane. Points are for > 2500 substructures from the central $(92'')^2$ of the cluster artificially placed on top of the lowest image from the top left panel of Fig. 2.4. Filled symbols are for a fixed source brightness distribution (fs) red circles for 1σ and blue squares for 3σ noise, solid lines are a linear fit to the 1 and 3σ points. Open symbols are for a reconstructed source (rs) where the only assumption is the regularity of the source, black squares for 1σ and green circles for 3σ. Grey small filled circles are the integrated residual over the image plane with a reconstructed source (rsi) and 1σ noise. The lower limits of resolved substructure lens strengths derived from the linear fits are $0.045''(1\sigma)$ and $0.13''(3\sigma)$.

In this section we compare the effect of substructures within the N-body simulation with the particle noise based on the surface brightness distribution of the images. The gravitationally lensed images are the only directly observable quantities, therefore any observational detection of a substructure in the lens will be based on a reconstruction of the observed image positions or the image brightness distribution. If there is no small-scale structure in the lens, it is in theory possible to find a source surface brightness distribution that fits all of the multiply lensed images. The presence of a substructure in the lens close to one image of a multiply imaged system will

result in a local imprint of the substructure on the closest image. Therefore, no source brightness distribution exists, that, when lensed through a smooth large-scale lensing mass distribution, will be able to model all multiply lensed images simultaneously. Therefore, there has to be substructure in the lens.

Here, we are using a similar method to quantify the effect of a substructure. We artificially place a substructure on the lens and simulate an image with substructure. We then try and fail to reconstruct this lens with substructure with a smooth model. In our case, we know the underlying smooth model, which is the same lens without the substructure. We can therefore calculate the image for the idealised smooth model by lensing a source through the lens model without the added substructure. The difference between the image for a lens with substructure and for a lens without substructure is then a measure for the failure of the smooth model to reproduce the image with substructure.

Similarly to Sec. 2.4.5, we use two different approaches to evaluate the influence of substructure on an image brightness distribution. The first method uses a fixed source surface brightness distribution to create a reference image $\boldsymbol{d}_0$ using the N-body cluster lens without any substructures close to any of the lensed images. This reference image is shown in the top left panel of Fig. 2.4. We then use the 2597 substructures from the central $(92'')^2$ as a sample of numerically simulated substructures and artificially place each substructure on top of the cluster directly behind the lowest of the three images at $(13'', -4'')$. At this position on the lens plane the substructure will have the biggest effect. For each substructure we then lens the same source and obtain 2597 different images $\boldsymbol{d}_i$. For each of these images we calculate the image brightness difference $\boldsymbol{d}_i - \boldsymbol{d}_0 = \Delta\boldsymbol{d}_i$ at each point on the lens plane. This is the brightness difference due to the artificially added substructure. We then compare this brightness difference $\Delta\boldsymbol{d}_i$ with the discreteness noise on the image $\sigma_{\boldsymbol{d}}$ from Sec. 2.4.5. We calculate the residual, R_i, as a difference in the image brightness due to the substructure that is greater than the amplitude of the fluctuations in the image surface brightness distribution at that point due to the particle noise as

$$R_i(\boldsymbol{x}) = |\Delta\boldsymbol{d}_i(\boldsymbol{x})| - n\sigma_{\boldsymbol{d}}(\boldsymbol{x}) \geqq 0 \qquad n = \{1, 2, 3\}\,. \tag{2.24}$$

The results for a residual integrated over the lens plane are identical to the results from the comparison based on the maximum value $\max[R_i(\boldsymbol{x})]_{\boldsymbol{x}}$ shown as an example for the integrated 1σ residual (rsi) multiplied by a factor of 0.01 to enhance the contrast in Fig. 2.11. The maximum value of the residual, R_i, is shown as solid red circles (1σ) and solid blue squares (3σ) in Fig. 2.11 for the Level-2 resolution using a fixed source surface brightness distribution (fs). The y-axis is the maximum residual R_i and the x-axis is the lensing strength of the substructure. The solid lines are linear fits that constrain the visible substructures. We consider a substructure to be visible when $R_i > 0$. The limits are $0.045''$ (1σ), $0.09''$ (2σ) and $0.133''$ (3σ) corresponding to 1.6, 3.8 and 6 $\times 10^9 \mathrm{M}_\odot$ respectively for a fixed source brightness distribution. Any substructure with a lens strength greater than these lower limits placed on top of the lowest image will result in an image brightness difference that is greater than the fluctuations due to the particle noise. These limits are very close to the values derived from the deflection angles in the previous section.

We have seen in Sec. 2.4.5 that lensing one fixed source surface brightness distribution through different noise realisations of the lens results in an overestimation of the noise on the

image by a factor of ~ 2. This definition of the noise on the image also includes an artificial relative source-caustic shift (see Sec. 2.4.5 for details), we therefore expect that the assumption of a fixed source here also is an over simplification. We therefore use the method described in Sec. 2.4.5 to reconstruct the best possible source (and therefore also the closest image) using the deflection angles with substructure to match the same image without substructure. For each of the reconstructed substructure images we then calculate the residual Eq. (2.24) from the previous paragraph. The maximum of these residuals are shown in Fig. 2.11 with black open squares (1σ) and green open circles (3σ) for a reconstructed source (rs), as well as an integrated residual as an example (rsi 1σ). The points no longer follow a linear relation. But the lower limits derived with this method of $0.045''(1\sigma)$ and $0.13''(3\sigma)$ if we reconstruct the source for each substructure image are identical to the ones with a fixed source brightness distribution.

This nontrivial result shows that including the unobservable relative source-caustic shift in the noise increases the noise by about a factor of two, see Sec. 2.4.5. But at the same time it also increases the image brightness difference due to a substructure in the lens. Therefore the cut-off $R = 0$ which indicates the minimum size of the resolved substructures remains unchanged. This is very convenient, since it allows us to accurately calculate the limits with much simpler and faster methods without having to reconstruct the source for each of the substructures and bootstrapped particle noise realisations of the cluster. The limits for the smallest resolved substructures that we found in this section based on the image brightness distribution of the lensed images are very similar to the limits from simpler lensing properties such as the deflection angles in Sec. 2.6.2 or the surface mass density in Sec. 2.6.1.

Up to here we have used a Gaussian source surface brightness distribution. This simplified source allows for a systematic description of the the effect of the particle noise on the lensed images, however we expect real source galaxies, especially at $z = 2$, to be more structured. In the following, therefore, we simulate sources with different degrees of structure.

2.6.5 Lensed images with Substructure of a Realistic Source

In order to simulate various degrees of smoothness for the source surface brightness distribution, we use the very structured source surface brightness distribution of a true galaxy as observed with HST. We then smooth this source surface brightness distribution with a Gaussian kernel with increasing sizes denoted as 20, 40 and 100. As an example, the source brightness distributions for 100 and 20 are shown in the bottom panels of Fig. 2.7. For each different source we recalculate the noise on the image brightness distribution, σ_d, as described in Sec. 2.4.5. We show the residual above the particle noise on the image brightness, of Eq. (2.24) for $n = 3$, in Fig. 2.12. As the structure in the source is decreased, an increasingly smaller number of substructures can be resolved above the noise limit, and the cutoff where $R \to 0$ shifts to the right. The limit for resolved substructures for the smoothest source, 100, is almost identical to the limit calculated with a Gaussian source surface brightness distribution in the previous section. In Fig. 2.12 we additionally show the residual using two different sources with an increased maximum source surface brightness by factors of 10 and 100 and the original Gaussian brightness distribution. As an extreme and unphysical limit we also show the residual for a source surface brightness distribution that is decreasing linearly with increasing distance from the source centre. Size and

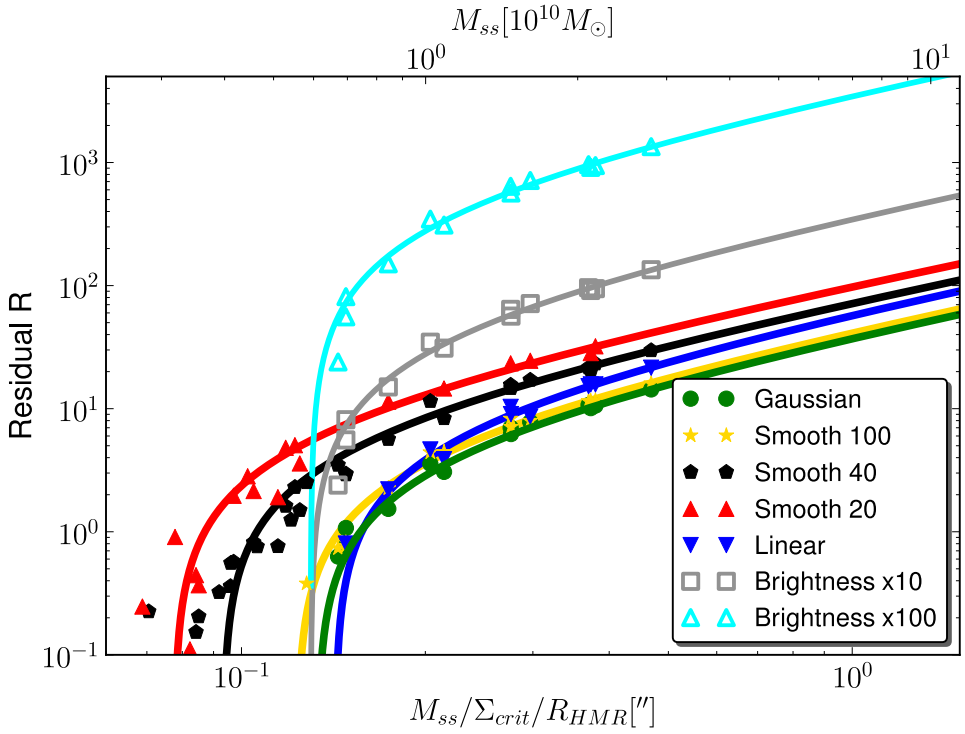

Figure 2.12: The same as in Fig. 2.11 but for different source brightness distributions and 3σ residuals. A very structured source brightness distribution is smoothed with a Gaussian kernel of sizes 20, 40 and 100, as a comparison, the Gaussian source surface brightness distribution from Fig. 2.11 and a linear source surface brightness distribution are also shown. A more structured source shifts the cutoff towards smaller substructures, while the overall residual is increased. Increasing the brightness of the source by a factor of 10 and 100 does not change the smallest resolved substructures, but increases the residual. For the sake of the clarity of the figure, only every 5th substructure is plotted for each line.

position of the source are kept constant for each of the seven curves. The behaviour of the curves can be qualitatively understood as follows.

Changing the brightness of the source while keeping the source size constant, increases the gradient of the source. Therefore, the same change in the deflection angles, $\Delta\boldsymbol{\alpha}$, due to either noise or substructure, will result in a greater change in image brightness, $\Delta\boldsymbol{d} \approx \Delta\boldsymbol{\alpha}\cdot\nabla s$, see also Eq. (2.9). This effect, however, affects the calculation of the noise on the images, $3\sigma_{\boldsymbol{d}}$, and the image brightness difference for each substructure, $\Delta\boldsymbol{d}_k$, in the same way. Therefore even though the residual Eq. (2.24) is increased, the lower limit of resolved substructures is unchanged. To understand the behaviour of the curves with increasing source structure, we consider a small substructure that is barely not resolved with a Gaussian source brightness distribution, for example a substructure with a lens strength of $0.12''$ which corresponds to a substructure mass of $\sim 5.4 \times 10^9\,\mathrm{M}_\odot$. Since the residual of this substructure is $R_{\max} \sim 0$, the image brightness

difference at any point due to this substructure, $\Delta \boldsymbol{d}_i$, is comparable to the noise on the image brightness, $3\sigma_{\boldsymbol{d}}$, which we calculated from the different particle noise realisations of the cluster, $\sigma_{\boldsymbol{d}} = 1/(N-1)\sum_k \Delta \boldsymbol{d}_k$. If we now increase and change the form of the source gradient with a more structured source on scales of $\Delta\boldsymbol{\alpha}_i$, the same change in the deflection angles due to the substructure, $\Delta\boldsymbol{\alpha}_i$, will result in an increased change in the image brightness, $\Delta \boldsymbol{d}_i$. In contrast to the increased source brightness, which only changes the amplitude of the source gradient, a more structured source additionally changes the shape of the gradient on scales smaller than $\Delta\boldsymbol{\alpha}_i$. Therefore and because the noise $\sigma_{\boldsymbol{d}}$ is a nonlinear combination of the effects of a field of positive and negative noise substructures it behaves differently than a more coherent single substructure. As we can see from Fig. 2.12 the net effect is more prominent for a single substructure. An increased source structure therefore allows the detection of smaller substructures above the particle noise limit.

Fig. 2.12 shows that a Gaussian source surface brightness distribution is a bad choice in terms of the lower limit of resolved substructures. The results are almost identical to the worse case, a linear source brightness distribution. The truly worst choice, however, would be a constant source brightness which is completely indifferent to changes in the deflection angles. A linear source gradient includes both, an increased gradient and at the same time less structure in the source brightness distribution with respect to a Gaussian source surface brightness distribution. Therefore, the overall residual is slightly higher and the cutoff is shifted to greater substructure lens strengths. The linear source surface brightness distribution is the extreme limit, a constant source gradient in Eq. (2.9). Therefore, the cutoff at $\beta = 0.14''$ ($6.5 \times 10^9 \mathrm{M}_\odot$) is identical to the lower limit derived from the substructure deflection angles in Sec. 2.6.2.

2.7 Scaling of the Resolution Limit

In the previous sections we derived different methods to compare the effect of a substructure on different lensing properties with the effect caused by the discrete representation of the N-body cluster with particles and we found lower limits on the substructure lens strength. Substructures with a weaker lens strength do not affect the lensing properties strong enough in order to be detectable above the particle noise limit.

This allows us to answer a very interesting question. If we plan to simulate gravitational lensing with a numerically simulated N-body mass distribution, what resolution do we need, in order to 'resolve' substructures of a given size?

The most advanced lower limits derived from the image brightness distribution with a reconstructing source method are very close to the simplified limits predicted from deflection angle differences, or even the simple comparison based on the surface mass density fluctuations in Sec. 2.6.1. We already derived scaling relations for the noise on the surface mass density in Sec. 2.5, therefore, we can now combine those results. If we approximate the noise as positive and negative Gaussian fluctuations, we can write the lens strength of one noise fluctuation as $\beta = \pi l \sigma_\kappa / (2 \ln 2)$, see Sec. 2.6.1. Here, l is the size of the smoothing kernel that is used to smooth the N-body particles on the lens plane, and σ_κ is the noise on the surface mass density. We can use this approximation to estimate the scaling of the equivalent lens strength of the noise

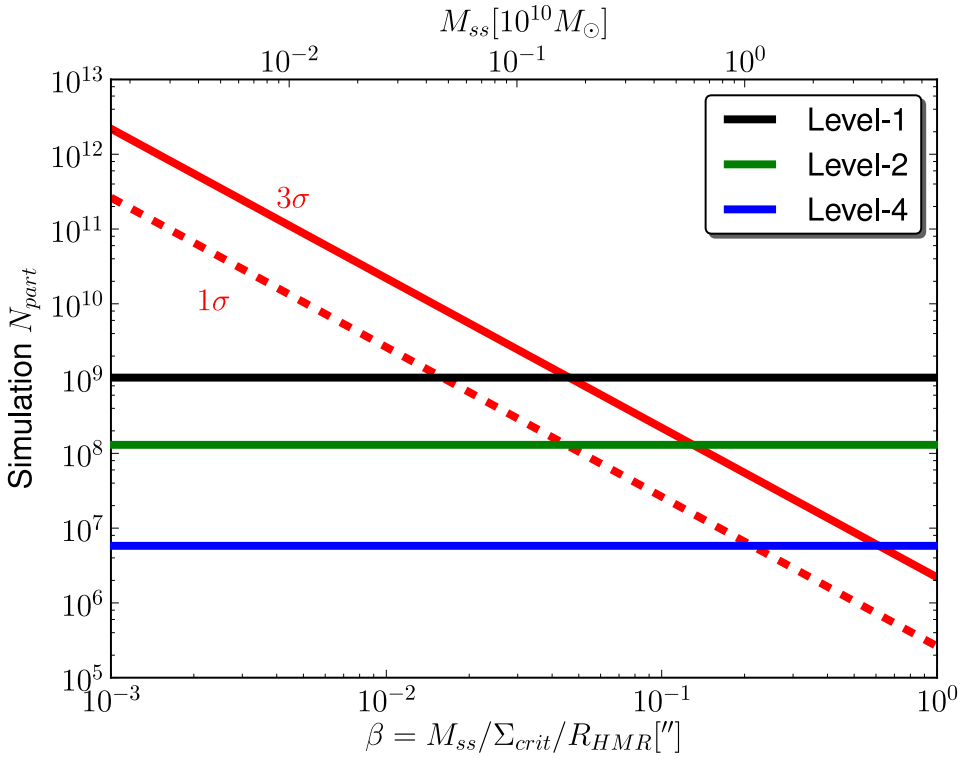

Figure 2.13: Required number of particles in a N-body simulation targeted to resolve substructures above 3σ of the noise with a given lens strength with strongly gravitational lensed images. The second x-axis converts the lens strength of the substructure to the average mass of a simulated substructure. The horizontal lines show three resolutions of the Phoenix simulations and their respective lower 3σ limits of $\beta_{\rm ss}^{\rm min} \sim 0.046''$ or $M_{\rm ss}^{\rm min} \sim 1.7 \times 10^9 {\rm M}_\odot$ for Level-1 and $\beta_{\rm ss}^{\rm min} \sim 0.135''$ or $M_{\rm ss}^{\rm min} \sim 5.8 \times 10^9 {\rm M}_\odot$ for Level-2 and $\beta_{\rm ss}^{\rm min} \sim 0.6''$ or $M_{\rm ss}^{\rm min} \sim 3.8 \times 10^{10} {\rm M}_\odot$ for Level-4.

fluctuations with $N_{\rm part}$ and $N_{\rm ngb}$. Using Eqs. (2.19) and (2.20), the relation scales as

$$\begin{aligned} \frac{\beta^j_{\rm crit}}{\beta^k_{\rm crit}} &\propto \frac{l^j}{l^k}\frac{\sigma^j_\Sigma}{\sigma^k_\Sigma} \\ &\propto \left(\frac{N^j_{\rm ngb}N^k_{\rm part}}{N^k_{\rm ngb}N^j_{\rm part}}\right)^{1/3}\left(\frac{N^k_{\rm part}}{N^j_{\rm part}}\right)^{1/6}\left(\frac{N^k_{\rm ngb}}{N^j_{\rm ngb}}\right)^{1/3} \\ &\propto \sqrt{\frac{N^j_{\rm part}}{N^k_{\rm part}}}. \end{aligned} \tag{2.25}$$

The limit for resolved substructures thus is independent of $N_{\rm ngb}$. This approximation holds, as long as the increase in smoothing does not smooth out any small-scale substructures and as long as the surface mass density remains reasonably smooth. To test Eq. (2.25), we repeated

the calculations in Sec. 2.6.4 which were done with a smoothing kernel with $N_{\rm ngb} = 64$, this time with a reduced number of neighbours $N_{\rm ngb} = 8$. This yields the same lower limit for the resolved substructures, however the noise on the individual lensing properties is substantially more prominent for a less smoothed N-body particle distribution. In Sec. 2.4 we quantified the noise individually for each lensing quantity. For example the critical lines and therefore the caustic will exhibit a great number of higher order singularities and swallowtails if the smoothing of the N-body particles is reduced. To simulate gravitational lensing, we have to smooth the N-body particles in order to obtain a reasonably smooth simulated image that is free from too much artificial numerical substructure.

From Sec. 2.6.4 we know that the Level-2 resolution resolves substructures as small as $\beta \sim 0.135''$. Inserting this result in Eq. (2.25), we can quantify the resolution requirement for a N-body simulation of gravitational lensing as a function of the smallest resolved substructures, which is shown in Fig. 2.13. For a given substructure that we want to resolve, we can estimate the size of the simulation we need to reduce the noise enough in order to see an effect of the chosen substructure above 3σ of the particle noise. Figure 2.13 is calculated from the noise in the surface mass density in Sec. 2.6.1, but the limits for the deflection angles in Sec. 2.6.2 and the lensed images with a linear source surface brightness distribution in Sec. 2.6.4 are identical. We have seen in Fig. 2.12 that the true lower resolution limits depend on the detailed source structure. However, we also know from Fig. 2.12 that a linear source surface brightness distribution is the worst case scenario. Therefore, these limits are valid, independent of the source used to simulate the gravitational lensing.

2.8 Summary

In the first part of this paper we investigated the effect of the discrete representation of a N-body simulation with particles on the simulation of gravitational lensing. We have used the currently highest-resolution simulations, the Phoenix simulations for our numerical lensing simulation. With the resolution of the Level-2 simulation we found the noise on the projected surface mass density to be $1-2\%$ and smaller than 5% even in high density regions at the centre of the cluster. We then used the noise on the inverse of the magnification to quantify the irregularities of the critical line. The noise in units of the inverse of the magnification increases with magnification and reaches its maximum at the critical lines where the magnification diverges. Due to the non-linearity of the lensing equation the noise plays a significant role in these high-magnification regions of strongly lensed images. In the surface brightness distribution of the lensed images, the particle noise causes fluctuations of the order of 10%. However, the assumption of a static source surface brightness distribution for the calculation of the noise fluctuations includes some unobservable effects such as a shift of the deflection angles relative to the source. Therefore, we also used a Bayesian source reconstruction argument in order to properly quantify the noise on the multiply lensed images. With this second method, the particle noise still has a considerable effect on the morphology of strongly magnified images. For the Level-2 resolution of the Phoenix simulations and a typical three image highly magnified giant arc, the noise on the image brightness is $\sim 5\%$. In Section 2.5 we derived useful scaling relations for the particle noise

on the surface mass density with the number of particles in the simulation and the number of smoothing neighbours.

In the second part of the paper we compared the influence of physical substructures in the N-body simulation with the particle noise we derived in the first part of the paper. We compared the projected surface mass density and the deviations of the critical lines. From the comparison of the lensed images we found that for substructures with a lens strength smaller than $0.13''$ there is no measurable effect in a simulation comparable to our Level-2 resolution above 3σ of the effect of the numerical particle noise. A typical substructure with a lens strength of $0.13''$ has a mass of $\sim 6 \times 10^9\,\mathrm{M}_\odot$ and therefore consists of $\sim 10^3$ particles with a mass of 6×10^6, see Table 2.1. These results were calculated with a fully adaptive source to avoid unobservable effects such as a shift in the effective source position. This measure of the importance of a substructure is motivated by observational reconstruction techniques. We found, that the results with the fully Bayesian source reconstruction measure are comparable to the much simpler results obtained from a non-adaptive, fixed source brightness distribution. In fact, the simpler comparisons based on the additional deflection caused by a substructure or the effective lens strength of the noise mass density fluctuations yield comparable results.

Therefore, finally, we combined in Sec. 2.7 the analysis of the scaling of the noise with the particle number of the simulation and the number of smoothing neighbours from the first part of the paper with the investigations of the effect of the simulated substructures from the second part of the paper. This allowed us to quantify the required resolution of a numerical N-body simulation if we want to detect substructures of a given size in our simulation of gravitational lensing.

2.9 Appendix: Variance of a Smoothed Particle Distribution

We calculate the variance of a smoothed distribution $\sigma_X^2\left(\boldsymbol{x}\right)$ from a known variance at each point $\sigma_Y^2\left(\boldsymbol{x}\right)$ under the assumption the latter is a slowly varying function with $\boldsymbol{x}$. The smoothing acts as a convolution with a normalized kernel function, which depends on one parameter, the smoothing length $l\left(\boldsymbol{x}\right) = l_x$. For a Gaussian smoothing kernel the value of the property we are interested in, X, at the point $\boldsymbol{x}$ can therefore be written as

$$X(\boldsymbol{x}, l_x) = \int \mathrm{d}^2\boldsymbol{x}'\, Y\left(\boldsymbol{x'}\right) \left\{ \frac{1}{2\pi l_{x'}^2} \exp\left[-\frac{\left(\boldsymbol{x} - \boldsymbol{x}'\right)^2}{2l_{x'}^2} \right] \right\}. \tag{2.26}$$

For random and uncorrelated variables $Y\left(\boldsymbol{x'}\right)$ we therefore get the variance

$$\sigma_X^2(\boldsymbol{x}, l_x) = \int \mathrm{d}^2\boldsymbol{x}'\, \sigma_Y^2(\boldsymbol{x'}, l_{x'}) \left\{ \frac{1}{2\pi l_{x'}^2} \exp\left[-\frac{\left(\boldsymbol{x} - \boldsymbol{x}'\right)^2}{2l_{x'}^2} \right] \right\}^2. \tag{2.27}$$

If we now assume that $\sigma_Y^2(\boldsymbol{x'}, l_{x'})$ is a slowly varying function with position $\boldsymbol{x'}$ or more precise we assume σ_Y^2 to be constant with respect to changing $\boldsymbol{x'}$ over sizes where the squared Gaussian

kernel is non-vanishing, which is approximately true for $|\boldsymbol{x}-\boldsymbol{x'}| > 3l$, we can simplify Eq. (2.27)

$$\begin{aligned}\sigma_X^2(\boldsymbol{x}, l_x) &= \sigma_Y^2(\boldsymbol{x}, l_x) \int \mathrm{d}^2\boldsymbol{x}' \left\{ \frac{1}{2\pi l_{x'}^2} \exp\left[-\frac{(\boldsymbol{x}-\boldsymbol{x}')^2}{2l_{x'}^2} \right] \right\}^2 \\ &= \frac{\sigma_Y^2(\boldsymbol{x}, l_x)}{4\pi l_x^2} = c\frac{\sigma_Y^2(\boldsymbol{x}, l_x)}{\pi l_x^2}. \end{aligned} \tag{2.28}$$

The exact value of the constant c, will depend on the form of the smoothing kernel, here for a Gaussian kernel $c = 1/4$. As described in Sec. 2.4.2 there are other smoothing kernels with a similar shape, for example the polynomial kernel in Eq. (2.4) with $c = 1030/343$. We are using the kernel $W_i(r) = 3/(\pi l_i^2)\left(1 - r^2/l_i^2\right)^2$ for $r \leq l_i$ with $c = 9/5$. When comparing the different numerical values, we have to keep in mind that the characteristic length of the Gaussian kernel should be decreased by $\sqrt{103/1120} \approx 0.303$ in order for a particle to cover approximately the same area compared to the other two kernels.

Acknowledgements

Phoenix is a project of the Virgo Consortium. Most simulations were carried out on the Lenova Deepcomp7000 supercomputer of the Supercomputing Center of Chinese Academy of Sciences, Beijing, China, and on the Cosmology Machine at the Institute for Computational Cosmology (ICC) at Durham. The Cosmology Machine is part of the DiRAC facility jointly founded by STFC, the large facilities capital fund of BIS, and Durham University.

Chapter 3

Lensing Model of MACS J1149+2223 I: Cluster Reconstruction

S. Rau,[1] S. Vegetti,[1] S. D. M. White[1]
in preparation for publication

ABSTRACT

Measurements of the total logarithmic central slope constrain the evolution and assembly history of galaxy clusters and their Brightest Cluster Galaxy. We report the first full surface brightness distribution modelling of the galaxy cluster MACS J1149+2223. We compare the results from the full surface brightness modelling with a position based modelling approach and we identify more than twice the previously known positional constraints. This is the first time, the detailed lensing image configuration of two cluster galaxies forming substructure Einstein rings in a galaxy cluster is mapped. We find a radially dependent ellipticity of the cluster mass distribution. Due to the continuous, extended radial coverage of the multiple images in this system, we accurately determine the total central slope $\partial \log \rho / \partial \log r = -1.32$ of the mass distribution within 8 to 80 kpc. This is within the cluster-to-cluster scatter and is therefore consistent with previous measurements in galaxy clusters. Under the assumption that the total mass of the BCG is only baryonic, this implies that the dark matter profile is shallower than what is predicted from N-body dark matter only simulations.

[1]Max-Planck Institute for Astrophysics, Karl-Schwarzschild Str. 1, D-85748, Garching, Germany

3.1 Introduction

Our current understanding of structure formation is based on a hierarchical picture where more massive Dark Matter (DM) structures form via progressive merging of smaller objects. Dark Matter only simulations over the last two decades have predicted remarkably self-similar DM mass profiles that are well fit by gradually steepening analytic profiles such as the Einasto profile (Einasto, 1965) or the Navarro Frenk and White (NFW) (Navarro et al., 1997) profile, with little modification for a large range of scales from galaxy clusters (Reed et al., 2005; Diemand et al., 2004; Springel et al., 2001, 2005; Merritt et al., 2006; Gao et al., 2012) to galaxies (Navarro et al., 2010). Although this general picture, a central slope $\gamma_1 = \partial \log \rho / \partial \log r = -1$ and a second, steeper outer slope $\gamma_2 = -3$ is generally accepted, the details are still being refined. On cluster scales Gao et al. (2012) found considerable (~ 20 percent) halo-to-halo scatter in a suite of nine high-resolution simulated N-body DM-only clusters. At galaxy scale, environmental and baryonic effects become increasingly important in shaping the DM mass distribution.

Galaxy clusters provide powerful tools to compare the predictions of cluster formation and assembly history from numerical simulations with observations. There has been considerable effort to get a coherent picture of the total cluster mass distribution on a large range of scales by combining stellar kinematics at the innermost radii ($r < 10$ kpc) with weak lensing measurements for radii $r > 100$ kpc and strong lensing on intermediate scales (Sand et al., 2004, 2008; Newman et al., 2013, 13b) . Clusters are very nonlinear systems where objects of different scales interact. For the study of cluster substructure such as cluster galaxies or DM subhalos, therefore detailed high resolution modelling is needed on an cluster-by-cluster basis.

There is no conclusive prediction from numerical simulations for the total central slope of the galaxy cluster mass distribution to date. On scales of a few kpc the baryonic component of the BCG and the dark matter halo both play a comparable role in shaping the total density, however, there are competing hypothesis about the relative importance and the relevant physical processes involved. The competing effects are the steepening due to adiabatic contraction (Gnedin et al., 2004; Sellwood & McGaugh, 2005; Sommer-Larsen & Limousin, 2010), the flattening of the central cusp mainly via the (repeated) ejection of gas by Active Galactic Nuclei (AGN) feedback (Martizzi et al., 2013) or via heating by dynamical friction (El-Zant et al., 2001, 2004). Even in simulations with dissipationless mergers (Laporte et al., 2012) a flattening of the DM halo can be achieved.

Sand et al. (2008) combined stellar velocity dispersion observations with strong lensing data for the cluster Abell 383 and found that the asymptotic inner slope of the dark matter is shallower ($\gamma_{\rm DM} = -0.45$) than the value predicted from purely DM simulations (-1). Recent observational constraints come from Newman et al. (2013) who performed a combined stellar kinematic, strong lensing and weak lensing mass reconstruction of seven massive ($0.4 < M_{200}/10^{15}/\mathrm{M}_\odot < 2$)[2] clusters with redshifts between 0.2 and 0.3. They find a 3D central logarithmic total mass density slope slightly steeper but consistent with NFW ($\gamma = -1.16$) with considerable scatter between clusters of $\sigma_\gamma = 0.13\,(68\%\mathrm{CL})$. This is the total density profile, where the central < 10 kpc are dominated by the BCG. Their separate analysis of the contributions of Baryons and

[2] M_{200} is the mass within a sphere with radius r_{200} and a mean density 200 times the critical density

DM in Newman et al. (13b) also indicates a flattening of the DM only profile with a logarithmic central DM slope of $\gamma_{\rm DM} = -0.5$.

In this paper we focus on building a high resolution lens model of MACS J1149+2223 and compare the slope inferred from the lensing reconstruction with the predictions for the total central mass density slope of galaxy clusters from cosmological structure formation simulations. The paper is organised as follows. We describe the observations, the image morphology of the main lensed image and the newly identified positional constraints in section 3.3. In section 3.5 we describe our analytic mass parametrization and in section 3.6 the two modelling methods. Section 3.7 contains the main results, the best lens models for the position modelling and the surface brighness modelling in sections 3.7.1 and 3.7.2 and the slope measurement of the total mass distribution in section 3.7.4. Throughout this paper, we assume the values $H_0 = 67.3$ and $\Omega_m = 0.315$ from Planck. At the redshift of the cluster, $z = 0.544$, one arcsec corresponds to 6.6 kpc. The source of system 1 is at $z = 1.52$. The source redshifts of systems 1-8 are listed in Tab. 3.1.

3.2 Models of the Cluster MACS J1149+2223

There are two previously published lens models for the cluster MACS J1149+2223. The first reported model is by Zitrin & Broadhurst (2009). They assume that mass approximately follows light and smooth a superposition of power law mass profiles for each galaxy for their mass model. The constraints are the multiple image positions from strong lensing, but many of the details especially for system 1 (see Sec. 3.3) are only reproduced in a general picture. They found a DM surface mass density close to uniform out to a large radius of 200 kpc under the assumption that the BCG consists only of stellar mass.

The second model by Smith et al. (2009), is also only based on multiple lensed image positions. However, they already identify a large number of bright source clumps in the main image system. Their best modelled image positions have a root mean square (rms) deviation of the observed positions of $0.5''$. Their preferred mass model includes a central component and three smaller group/galaxy scale halos. However, the mass distributions of *all* (including the central galaxies except the Brightest Cluster Galaxy) are tied to their light distributions. They rule out the previously found flat central profile.

In this work, we improve on those previous models mainly on three points. First we are using a more sophisticated model. We are modelling *all five* galaxies close to lensed images and close to the cluster centre as individual mass profiles. This is crucial in reproducing the morphology of the lensed image of the main system (see Sec. 3.3). Second, we identify twice as many constraints as previously known. This includes details of two substructure Einstein rings that form around two cluster galaxies and details of the nonlinear image configuration of the image covering the centre of the cluster, therefore putting tight constraints on the total mass density slope. Third, we use a more sophisticated method, originally developed and applied on galaxy scales (Koopmans, 2005; Suyu et al., 2006; Vegetti & Koopmans, 2009) and recently also on cluster scales by Eichner et al. (2013), where we use not only the information of the positions of the multiply lensed images, but the full image surface brightness distribution.

3.3 Observations and Constraints

The galaxy cluster MACS J1149+2223 at redshift $z = 0.54$ was observed as part of the CLASH program with the Advanced Camera for Surveys (ACS) on board the Hubble Space Telescope (HST). For details on the observations, the available filters and the imaging pipeline, we refer the reader to Postman et al. (2012). The photometric redshifts for both, the lensed sources and the galaxy cluster were calculated by the CLASH image pipeline.

Since our lens modelling technique makes use of both the lensed image surface brightness distribution and position, it is very important to minimise any light contamination from the lensing galaxies (see Sec. 3.4 for details on the lens galaxies surface brightness subtraction); this is particularly true for those images that lie close to bright cluster member galaxies. In this paper, we therefore focus on the lens modelling of the F555W filter of the ACS, this being a compromise between a high signal-to-noise ratio and the least light contamination from the cluster galaxies.

For the position modelling in Sec. 3.6.1, the robust and correct identification of many corresponding multiply lensed source clumps is crucial. Note, that the surface brightness reconstruction in Sec. 3.6.2 does *not* depend on single somewhat arbitrarily chosen points on the image plane since it uses the full image brightness distribution of the lensed images. We identify seven different sources lensed by the cluster MACS J1149+2223 in as many as 21 images. Figure 3.1 shows an overview of these sets of images. We follow the nomenclature of Smith et al. (2009) and Zitrin & Broadhurst (2009) to label the multiple images. The central, main image 1 of MACS J1149+2223 consists of three very large multiply lensed images of a spiral source galaxy. Three bright clumps of the same source have been measured by CLASH within image 1.1 with redshifts of 1.47, 1.57 and 1.8. Similarly to what assumed by Smith et al. (2009) and Zitrin & Broadhurst (2009), we place the source at a redshift of $z = 1.52$.

Image system 1 consists of at least triple lensed images of a spatially resolved spiral background galaxy and it is one of the largest known gravitationally lensed images systems to date. For an overview of this main system 1 as well as the other multiple image systems and the cluster we refer to Fig. 3.1. For a detailed view of each of the three main images 1.1, 1.2 and 1.3 without the critical curves overlaid we refer to Fig. 3.2. In blue we show the constraints identified by Smith et al. (2009), in red the multiply imaged source knots that we additionally identify and use in this work.

The farthest of the three main images is 1.1 at $-16.2'', 14''$ is located at a distance of about $20''$ from the BCG. There are no massive cluster member galaxies nearby and the two smaller close-by galaxies have no measurable lensing effect on the image surface brightness distribution. This image therefore gives a good impression of the almost unlensed source morphology. For the first time, we are able to constrain the lower left part of the source, consisting of the triple imaged clumps 26 and 24 (Fig. 3.2).

A second image 1.2 is lensed at $5.1'', -9.1''$ at a distance of 11 arcseconds. If we compare the surface brightness distribution of images 1.2 and 1.1 in Fig. 3.2 it is evident that the lower left spiral arm of the source in image 1.2 is additionally lensed. Galaxy G2 acts as an additional strong lens and deflects the two source clumps 50 and 52 to a 'secondary Einstein ring' with Einstein radius of about $1.3''$. Due to the additional deflection of the galaxy G2, clump 52 is lensed a total of seven times. Since the fifth image in image 1.2 is lensed very close to the subtracted lens

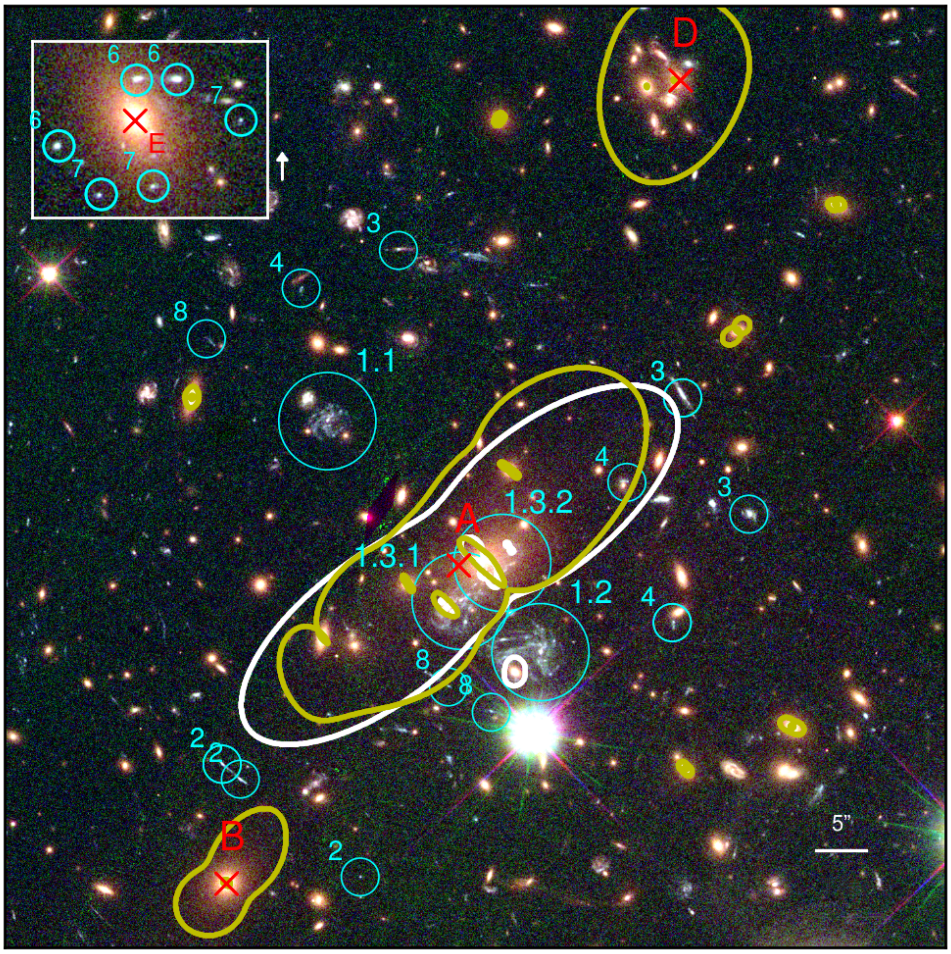

Figure 3.1: HST F814W/F606W/F555W RGB colour image of the Cluster Lensing And Supernova survey with Hubble (CLASH) observation of MACS J1149+2223. Overlaid in white is the critical curve for a source redshift of $z_s = 1.52$ and a cluster redshift of $z_l = 0.544$ for our central model, in yellow the critical curve for our outer model. The centre of the reconstructed DM halo is $\approx 1''$ left of the BCG. There are three separate main images labelled 1. The detailed morphology of the central image, 1.3, is more complicated, parts have a seven fold image configuration. Additional multiple images are labelled 2-8, for details see Sec. 3.3. The lower left corner of the inset is located at $-22.6, +95.8''$ from the BCG, the inset scale is that of the main figure.

Image No.	1	2	3	4	6	7	8
z_s	1.52	2.1	3.25	3.0	1.5	1.5	2.9

Table 3.1: Source redshifts of the multiple image systems identified in MACS J1149+2223 in Fig. 3.1.

galaxy surface brightness distribution and since the corresponding multiple images in the main images 1.1 and 1.3 are not uniquely identifiable, we use, as constraints, only four of the seven multiple images. The high additional magnification from the galaxy G2 increases the visibility of the source clump 52 in image 1.2.

The third lensed image, 1.3, is lensed at a distance of $4.5''$ from the BCG at $-2.9'', -4''$ and has a significantly more complicated morphology. In Fig. 3.2 we split this central image in two. Image 1.3.1 is a full multiple image of the source galaxy. Note the cluster galaxy G1 that lies on top of the lensed image. This galaxy is responsible for additional strong lensing in image 1.3 similar to galaxy G2 in image 1.2. The newly identified clumps 15 and 21 are additional multiple images deflected by galaxy G1. Together with the positions of the new constraints 24 and 26, the mass distribution of the galaxy G1 is now tightly constrained over a large range of radii from $r = 0.4''$ $(2.6\ \mathrm{kpc})$ the galaxy centre to $r = 23.0''$ $(150\ \mathrm{kpc})$

Finally, the most important and critical image is image 1.3.2. All multiple source clumps in this image are in the high magnification region close to the cluster centre where there are three galaxies, the brightest cluster galaxy BCG, and the galaxies G3 and G4. Image 1.3.2 consists of multiple images of only a few source clumps and was previously not constrained well. Here, we add the multiple source clumps 192, 8 and 6 as well as the 5th image of clump 19 between images $1.3.1$ and $1.3.2$ to our list of constraints. In total we identified as many of 77 image positions in system 1 that we use to constrain the central regions of the cluster mass distribution.

At large scales the mass distribution of the cluster is constrained by the triple image systems 2, 3, 4, 6, 7 and 8. In total, these 'outer' constraints add up to 18 images rising from lensed sources located at redshifts spanning from $z = 1.5$ to $z = 3.25$. Table 3.1 summarises the source redshifts for all multiple images in MACS J1149+2223. Two of the lower images of systems 8 and 4 provide constraints at distances of 13 and 19 arcsec. Most constraints of systems 2, 3, 4 and 8, however, are in the range $30 - 32$ arcsec from the BCG. The farthest strong lensing multiple images form a ring, three on either side of a massive galaxy located at $-17.2'', +101.1''$ from the BCG.

3.4 Galaxy Surface Brightness Subtraction

The surface brightness distribution of the seven galaxies, the BCG and a Star close to the three main lensed images are modelled using the publicly available programm galfit (Peng et al., 2002). The positions of all modelled galaxies are summarised in Tab. 3.2. All light distributions are modelled as a Sersic profile. This step is only needed for the full surface brightness information of the lensed images for modelling in Sec. 3.6.2.

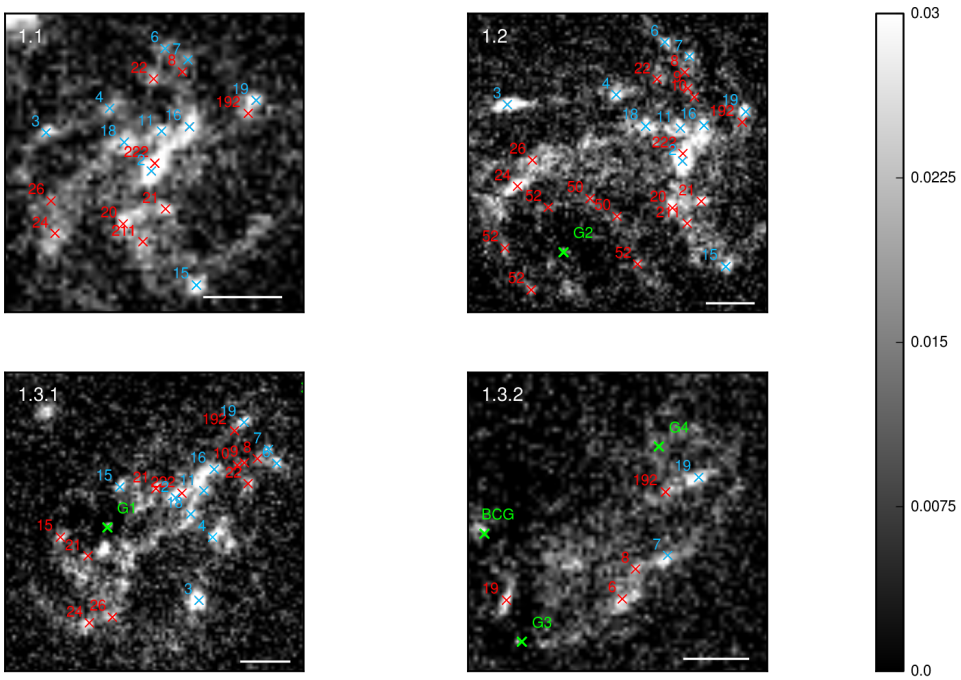

Figure 3.2: Constraints used for the image position modelling. Top left: Relatively undistorted source image. Top right: Second image with a distinct signature of an additional Einstein ring, around the satellite galaxy G2 (galaxy surface brightness subtracted). Bottom row: Strongly distorted image system 3 close to the central galaxies. Green crosses indicate galaxies G1, G2, G3, G4 and the BCG, whose surface brightness distribution we subtracted in preparation for the surface brightness modelling. Blue constraints are from Smith et al. (2009), Red constraints are newly identified in this work. White line at the bottom indicates 1 arcsec scale.

	$x\,[''] $	$y\,[''] $
BCG	0	0
G1	-3.6	-4.6
G2	3.2	-11.1
G3	0.5	-1.6
G4	2.6	1.4
G5	-17.6	12.9
G6	-13.8	12.5
G7	-7.6	-2.3
Star	5.1	-17.2

Table 3.2: Positions relative to the BCG of those galaxies and the stellar component whose surface brightness distribution was modelled with a Sersic profile and subtracted for the full surface brightness modelling of the lensed image system 1 in Sec. 3.6.2.

3.5 The Mass Model

In this section we describe the analytical mass model and free parameters used for the lens modelling. The same model is used for both, the image position (Sec. 3.6.1) and the surface brightness distribution modelling (Sec. 3.6.2).

Following the CDM paradigm, the parametric mass model considered in this paper includes: a central dark matter halo for the cluster A, five central mass components for the BCG and the galaxies G1,G2, G3 and G4, three outer mass components for two massive galaxies at B = (-25.7", -32.3"), and E = (-17.2", 101.1") and a group of smaller galaxies at D = (19.2", 48.1") from the BCG, one mass component for each of the remaining identified cluster member galaxies and finally the contribution of external shear. In previous analysis of this cluster (Zitrin & Broadhurst (2009) and Smith et al. (2009)) the masses of *all* galaxies, apart from the BCG, were tied to one fiducial galaxy via the following scaling relations

$$\begin{aligned} \sigma &= \sigma^* \left(\tfrac{L}{L^*}\right)^{1/4} \\ r_{\rm core} &= r^*_{\rm core} \left(\tfrac{L}{L^*}\right)^{1/2} \\ r_{\rm cut} &= r^*_{\rm cut} \left(\tfrac{L}{L^*}\right)^{1/2}, \end{aligned} \tag{3.1}$$

while their position, ellipticity and position angle were fixed to those of their respective surface brightness distributions. In this work, instead, all five central galaxies and the three outer mass components are independently modelled. This represents a major improvement in the model, since the details of the lensing reconstruction crucially depend on the central mass distribution. In particular, we assume that all the considered mass components have a total mass density distribution that follows a dual softened Power-law Elliptical Mass Distribution (dSPEMD) (Barkana, 1998; Kassiola & Kovner, 1993), with projected surface mass density in units of the critical density $\kappa = \Sigma/\Sigma_c$ given by

$$\kappa\left(R\right) = n\left[(R^2+c^2)^{-\gamma} - (R^2+t^2)^{-\gamma}\right]. \tag{3.2}$$

This corresponds to a 3D density

$$\begin{aligned} \rho(r) &= \tilde{n}\left[\left(r^2+c^2\right)^{-\gamma_{\rm 3D}/2} - \left(r^2+t^2\right)^{-\gamma_{\rm 3D}/2}\right] \\ \text{where} \quad \tilde{n} &= n\frac{\Sigma_{\rm c}\Gamma\left[\gamma_{\rm 3D}/2\right]}{\sqrt{\pi}\Gamma\left[\left(\gamma_{\rm 3D}-1\right)/2\right]}. \end{aligned} \tag{3.3}$$

Here, the 2D slope γ is related to the 3D slope via $\gamma = \left(\gamma_{\rm 3D}-1\right)/2$, R denotes the projected, elliptical radius where $R^2 = x^2 + y^2/q^2$ with the ellipticity q, the core c and the truncation radius t. The dSPEMD profile has a total of seven free parameters $(x, y, n, c, t, \gamma, q)$.

Since tests with variable slope always converge to a value close to $\gamma = 0.5$ (isothermal), we keep the slope of the cluster halo A fixed for the final modelling. For the galaxies G1 and G2, we assume a spherically symmetric ($q \equiv 1$) density distribution with vanishing core radius ($r_c \equiv 0$) centred at the light distribution, while we leave the slope, the normalisation, and the truncation radius as free parameters. This is different from previous analysis of galaxy truncations,

where the slope is generally kept fixed at isothermal (Suyu & Halkola (2010),Donnarumma et al. (2011) or Eichner et al. (2013)). This simplifying assumption is often necessary to avoid degeneracies between the slope, the normalisation and the truncation radius. In most cases of *isolated* galaxy-scale lensing there are not enough constraints on different radii to break those degeneracies since there is only information at the scale of the Einstein radius. The unique case of MACS J1149+2223 provides enough constraints over a large range of radii to measure both the slope and the truncation radius for both the galaxies G1 and G2. We refer the reader to chapter 4 for a detailed comparison of different mass models for G1 and G2. In this chapter, we restrict ourselves to the best parametrization inferred in chapter 4. For the galaxies G3 and G4 we also fix the position, the slope to isothermal and the truncation radius to $1''$ and $7''$ respectively, while the galaxies B and D and the galaxy group E have an isothermal slope but a truncation radius which is free to vary. We did tests during which we allowed all the parameters to vary in order to identify those parameters that are not not constrained by the data or that do not influence the quality of the model and that could be therefore kept fixed during the final modelling.

At larger radii we include *all galaxies with* $(\mathrm{I}_{814} < 20.5)$ as spherical, isothermal dSPEMD with position, ellipticity, and rotation angle fixed to the best fit parameters of their light distribution while the mass normalisation, the core radius and the truncation radius are scaled with the galaxy luminosity via Eq. (3.1) as previously done by Smith et al. (2009), Jullo et al. (2007) and Eichner et al. (2013). We adopt the best-fit parameters for a L^* galaxy from Smith et al. (2009), $\sigma = 180\mathrm{km/s}$, $r_{\mathrm{core}} = 0.2\mathrm{kpc}$ and $r_{\mathrm{cut}} = 30\mathrm{kpc}$.
Finally, the external shear is described by a shear strength γ_s and a position angle θ_γ, both free parameters of the mass model. For a detailed list of the galaxy positions and our best model parameters see Tab. 3.3 or Fig. 3.2.

3.6 Modelling Methods

We model the mass distribution of MACS J1149+2223 with two different methods. In particular, we first build a model using the lensed image positions and the constraints introduced in Sec. 3.3 as described in the next section, we then refine this model with a full image surface brightness distribution modelling.

3.6.1 Modelling of the Image Positions

For the image position modelling, a Markov Chain Monte Carlo (MCMC) is used to optimise the posterior

$$P\left(\boldsymbol{\eta}|\boldsymbol{d}\right) \propto P(\boldsymbol{d}|\boldsymbol{\eta})P(\boldsymbol{\eta}) \tag{3.4}$$

where $\boldsymbol{\eta}$ is a vector containing the model parameters which depends on the parametrization of the mass distribution in Eq. 3.2,

$$\boldsymbol{\eta} = (x_i, y_i, \theta_i, n_i, \gamma_i, c_i, \epsilon_i, t_i) \quad i \text{ in } \{1, ..., N\}\,, \tag{3.5}$$

and $\boldsymbol{d}$ is the data vector containing all of the image position constraints. The likelihood,

$$P(\boldsymbol{d}|\boldsymbol{\eta}) = \frac{1}{Z}\exp\left(-\frac{1}{2}\sum_{i}^{N_i}\delta\boldsymbol{u}_i^T\boldsymbol{\mu}_i^T\boldsymbol{C}^{-1}\boldsymbol{\mu}_i\delta\boldsymbol{u}_i\right) \quad (3.6)$$
$$\text{where} \quad \delta\boldsymbol{u}_i = \boldsymbol{u}_i^{\rm obs} - \boldsymbol{u}_i^{\rm mod}$$

is defined on the source plane, which is a good and fast approximation for the true distance on the image plane (see for example Halkola et al. (2006); Suyu & Halkola (2010)). Here the source plane positions are denoted $\boldsymbol{u}_i$ and the sum is over the $N_i = 3(4, 5, 7)$ images of MACS J1149+2223 . The entries of the vectors $\boldsymbol{u}_i$ for the source positions and $\boldsymbol{\mu}_i$ for magnification contain the different constraints for each image.

The speed and the success of this method depend on the number of correctly identified source clumps that are multiply lensed. Compared to the modelling of the full image brightness distribution described in the next section, the position modelling only uses a very small fraction of the available constraints resulting in greater parameter uncertainties and correlations as shown in Figs. 3.7 and 3.8. However, since the evaluation of Eqs. (3.4) to (3.6) is very fast, we can use the position based modelling to rule out a big portion of the full parameter space. In practice, we include this method also in the surface brightness modelling, by disfavouring models that predict respective lensed image points that are separated by more than the size of the source. This is a significant speedup for the full image brightness modelling.

3.6.2 Modelling of the Image Surface Brightness Distribution

The full modelling of the image surface brightness information is based on the technique introduced by Vegetti & Koopmans (2009) and Suyu et al. (2006). In the following, we summarize the most important aspects of this method. At each step of the modelling, we find the best source surface brightness distribution $\boldsymbol{s}$ for an observed lensed image $\boldsymbol{d}$, source regularisation strength λ_s and form $\boldsymbol{R}$. For each set of lens model parameters $\boldsymbol{\eta}$, we find the source surface brightness distribution $\boldsymbol{s}$ that maximises the following probability density function

$$P\left(\boldsymbol{s}|\boldsymbol{d},\boldsymbol{\eta},\boldsymbol{R}\right) = \frac{P\left(\boldsymbol{d}|\boldsymbol{s},\boldsymbol{\eta},\boldsymbol{R}\right)P\left(\boldsymbol{s}\right)}{P\left(\boldsymbol{d}|\lambda_s,\boldsymbol{\eta},\boldsymbol{R}\right)}. \quad (3.7)$$

The likelihood is a measure how well the model fits the data,

$$P\left(\boldsymbol{d}|\boldsymbol{s},\boldsymbol{\eta},\boldsymbol{R}\right) = \frac{1}{Z}\exp\left[-\frac{1}{2}\left(\boldsymbol{M}\boldsymbol{s}-\boldsymbol{d}\right)^T\boldsymbol{C}^{-1}\left(\boldsymbol{M}\boldsymbol{s}-\boldsymbol{d}\right)\right]. \quad (3.8)$$

Z is the normalisation, $\boldsymbol{M}$ is the lensing operator relating the source plane positions to the lens plane positions via the lens equation. $\boldsymbol{M}$ is calculated in each step as a lensing matrix for a set of parameters $\boldsymbol{\eta}$. In Eq. (3.8), $\boldsymbol{C}$ denotes the covariance of the observed image on the image plane. For the modelling of the F555W data of MACS J1149+2223 we assume uncorrelated noise on the observed images that follows a Gaussian distribution with a RMS of $\sigma = 0.0065$. We choose a quadratic prior for the source, $P\left(\boldsymbol{s}\right) \propto \exp\left(-0.5||\boldsymbol{R}\boldsymbol{s}||^2\right)$, favouring a flat source brightness

Parameter	Bright. Model	Pos. Model
x_h	$312.06^{+0.10}_{-0.22}$	$315.0^{+4.4}_{-3.6}$
y_h	$206.18^{+0.10}_{-0.23}$	$208.9^{+5.0}_{-3.7}$
ϕ_h	$0.64610^{+0.00076}_{-0.00167}$	$0.646^{+0.032}_{-0.025}$
n_h	$20.515^{+0.062}_{-0.131}$	$20.57^{+1.16}_{-0.90}$
c_h	$187.23^{+0.71}_{-1.58}$	191^{+18}_{-14}
ϵ_h	$0.3933^{+0.0032}_{-0.0018}$	$0.392^{+0.039}_{-0.033}$
n_{BCG}	$1.0572^{+0.0073}_{-0.0046}$	$1.10^{+0.11}_{-0.14}$
n_{G3}	$0.3240^{+0.0028}_{-0.0043}$	$0.353^{+0.117}_{-0.096}$
n_{G1}	$0.0579^{+0.0075}_{-0.0065}$	$0.145^{+0.184}_{-0.083}$
γ_{G1}	$0.942^{+0.011}_{-0.013}$	$0.80^{+0.13}_{-0.20}$
t_{G1}	$11.3^{+1.5}_{-1.5}$	51^{+42}_{-39}
n_{G2}	$0.3193^{+0.0041}_{-0.0034}$	$0.32^{+0.18}_{-0.11}$
γ_{G2}	$0.7601^{+0.0026}_{-0.0024}$	$0.762^{+0.087}_{-0.113}$
t_{G2}	152^{+18}_{-15}	105^{+79}_{-69}
n_{G4}	$0.3019^{+0.0141}_{-0.0038}$	$0.25^{+0.11}_{-0.14}$
$\|\gamma\|$	$0.0536^{+0.0027}_{-0.0013}$	$0.056^{+0.015}_{-0.019}$
ϕ_γ	$2.731^{+0.016}_{-0.024}$	$2.70^{+0.14}_{-0.13}$

Table 3.3: Modelled lens parameters and 95% CL errors for the central model from image position modelling and from the full brightness modelling of MACS J1149+2223.

distribution. In order to accommodate the very high dynamic range of the surface brightness distribution of MACS J1149+2223 we use a gradient source regularisation. Since the lensed image system 1 is very large, we only consider a subset of the image plane pixels (by a factor of 5) which are lensed back to the source plane. Those points on the source plane then define the base of a Delaunay triangulation which is used to interpolate to the full data set. Implicitly finding the best source via Eq. (3.7) in each step, we then optimise for the best model parameters using the posterior,

$$P\left(\lambda_s, \boldsymbol{\eta} | \boldsymbol{d}, \boldsymbol{R}\right) = \frac{P\left(\boldsymbol{d} | \lambda_s, \boldsymbol{\eta}, \boldsymbol{R}\right) P\left(\lambda_s, \boldsymbol{\eta}\right)}{P\left(\boldsymbol{d} | \boldsymbol{R}\right)}. \tag{3.9}$$

3.7 Results

We present the results from the image position modelling first in the next section and refine this result later using the full surface brightness information of the extended lensed images in Sec. 3.7.2.

3.7.1 Results from Image Position modelling

Due to a radius-dependent ellipticity in the mass distribution, we did not find any simple and physically motivated mass model that simultaneously satisfies both, the outer constraints $2-8$

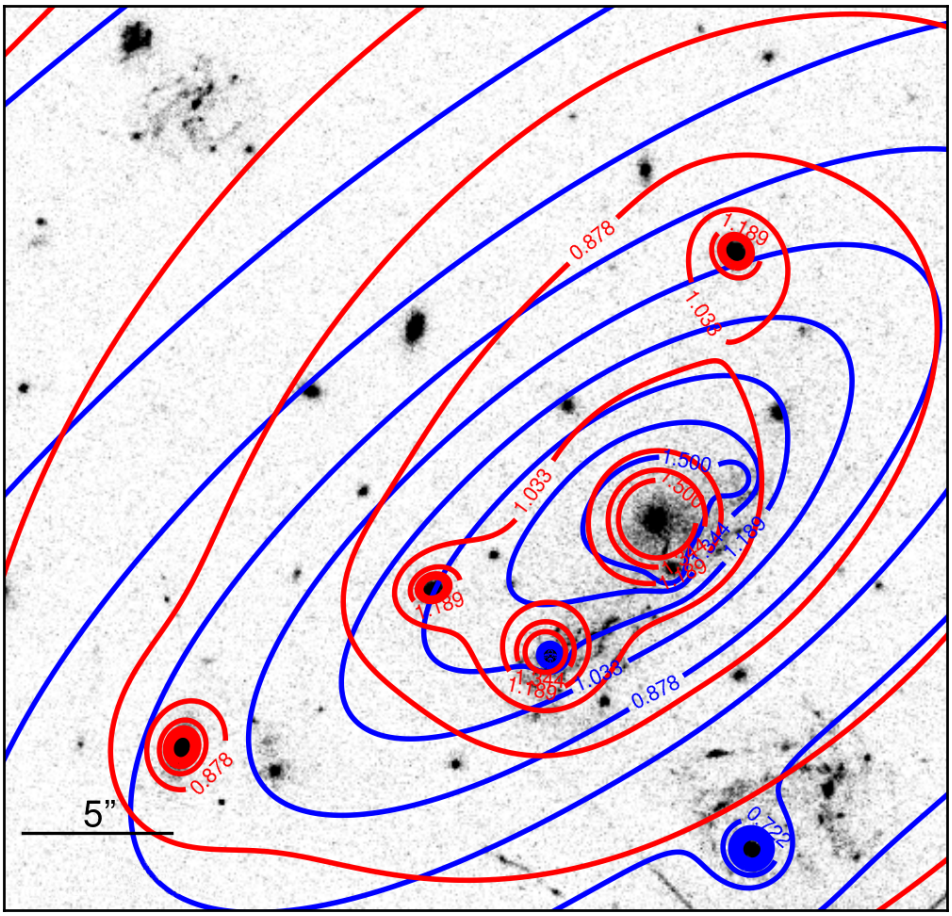

Figure 3.3: Contours of the mass distribution from the position modelling for the outer model including scaled cluster galaxies and three additional dark halos (red), and for the central model (blue). As an orientation, the grey background shows the CLASH observation of the cluster in the F555W filter.

shown in Fig. 3.1 and all 77 constraints in images 1.1-3 shown in Fig. 3.2. We therefore present a central and an outer model, spanning different regimes and different constraints.

Figure 3.3 shows the contours of the projected scaled surface mass density κ for these two models. As a comparison, the HST F555W image is shown as a grey scale background in Fig. 3.3. The blue contours are for the best-fit model using all 77 constraints of the central images 1.1-3 in Fig. 3.2. This model, our best fit 'central model', has an image plane RMS of $\sigma = 0.069''$, this is very close to the observational resolution limit of the 65 marcs CLASH data.

The red contours in Fig. 3.3 are for the best fit model for the outer constraints of systems 2-8 including only the blue constraints in systems 1.1-3 in Fig. 3.2. The best model parameters of this 'outer' model are equivalent to the model from Smith et al. (2009). Our outer model reproduces all constraints 2-8 in Fig. 3.1, but there might be additional and better constraints at larger radii from weak lensing. The image plane positional uncertainty of the 'outer' model is $\sigma = 0.45$ arcsec, which is comparable to the result by Smith et al. (2009).

However, these two models are not compatible with each other. In fact, the ellipticity of the two best-fit models is different; while the outer model (red) has a modest flattening of the central dark matter component of $\epsilon = b/a = 0.64$, the added constraints in system 1 force the central model (blue) to be more elliptic ($\epsilon = 0.39$). Due to the higher ellipticity, the central model then fails to reproduce the respective upper image of the triple systems 8, 3 and 4 (compare Fig. 3.1 for system numbers). System 2 is not reproduced by the central model, since it is almost entirely dominated by the mass component B which we do not include in the central model. The same holds for the uppermost constraints 6 and 7, which are dominated by the mass component E. To test this hypothesis, we included the latter two dark mass clumps, B and E in our central model. By doing so, we succeed in finding a somewhat acceptable fit for the constraints 2, 6 and 7. However, it is still not possible to reproduce the upper images for systems 3, 4 and 8 while keeping all 77 constraints for system 1.

Since we are interested in an accurate model for the main image 1, in the remaining of this paper, we restrict ourselves to the central model. For our best central model we find a 2D projected mass of $4.0 \times 10^{13} \mathrm{M}_{\odot}$ within the critical lines of the main image system 1. The critical lines at $z = 1.52$ cover an area of $672''^2$ that is equivalent to an effective radius of $14.6''$ $(96\,\mathrm{kpc})$. The mass is integrated within the central critical curve of the main dark matter halo and central galaxies and does *not* include any contribution from by the mass components B,D or E.

In Figure 3.4 we show the inverted positions of all the three (or more depending on multiplicity) images on the source plane and the respective predicted best source position as cyan stars. Since the RMS σ of the source plane positions is comparable to the line width of the triangles in Fig. 3.4, only in a few cases the cast-back source points of the three (or five/seven) different images can be resolved. Most constraints will appear as slightly extended cyan points in Fig. 3.4. As background we show contours of the source surface brightness distribution from the surface brightness modelling. Overlaid in green are the caustics. Seven times lensed parts of the source are clearly visible inside the caustic of the Einstein ring on the lower left of Fig. 3.4.

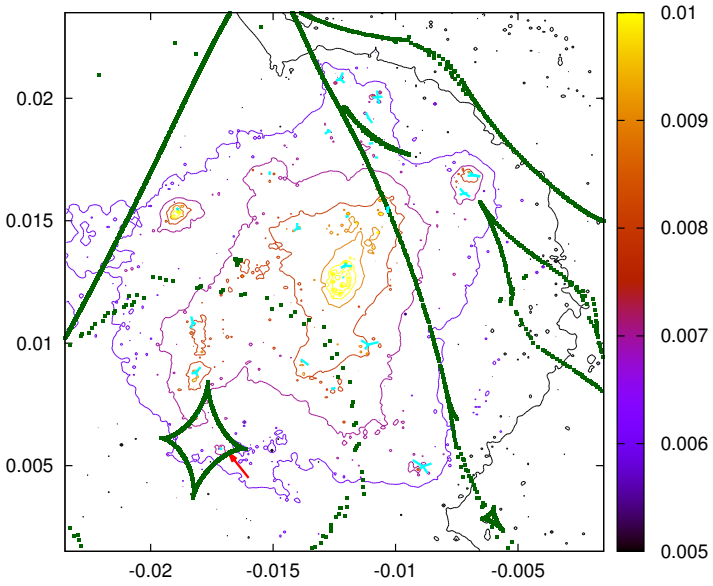

Figure 3.4: Source plane reconstruction from the position modelling. Contours show the full brightness reconstruction of the source from Sec. 3.7.2 for comparison. The critical lines split different parts of the source into different multiplicities. Lower left part of the figure shows the caustic of the substructure galaxy G1 causing the Einstein ring in image 1.2 and the 7-fold imaged source position labelled 52 in Fig. 3.2, which is here marked by a red arrow.

3.7.2 Results from Brightness Distribution modelling

The modelling of the full image surface brightness distribution uses a significantly large number of constraints. As a part of the modelling, it also provides an accurate source reconstruction on a nonuniform grid. Fig. 3.5 shows our best model of the lensed images. Each column contains one of the four main images of system 1; 1.1, 1.2, 1.3.1 and 1.3.2. In rows from top to bottom are the modelled images $\boldsymbol{m}$, the observed data $\boldsymbol{d}$ and the residual $\boldsymbol{r} = \boldsymbol{m} - \boldsymbol{d}$ in the bottom row. In the first column, image 1.1 is almost unlensed and closely resembles the original source surface brightness distribution. As a comparison, the best modelled source is shown in Fig. 3.6. The second image in the second column is distorted more significantly.

The aforementioned Einstein ring in image 1.2 is very accurately reproduced by our model. Note also the additional multiple images 15 and 21 (for nomenclature see Fig. 3.2) in image 1.3.1 and all of the morphological details of image 1.3.2 are perfectly reproduced to the noise limit of the CLASH observations. There are minimal increased residuals at the positions of the brightest source clumps $2, 3, 15$ and 19. Those are a consequence of the constant strength of the regularisation of the source surface brightness, λ_s, used throughout modelling. The brightness distribution of the source in Fig. 3.6 is very nonuniform and at the edges of the brightest source clumps the gradient increases significantly, approaching infinity. This simply means that in those regions the resolution provided by CLASH is insufficient to capture the brightness distribution in detail. In this case, any form of regularisation enforces a smoothing of those regions.

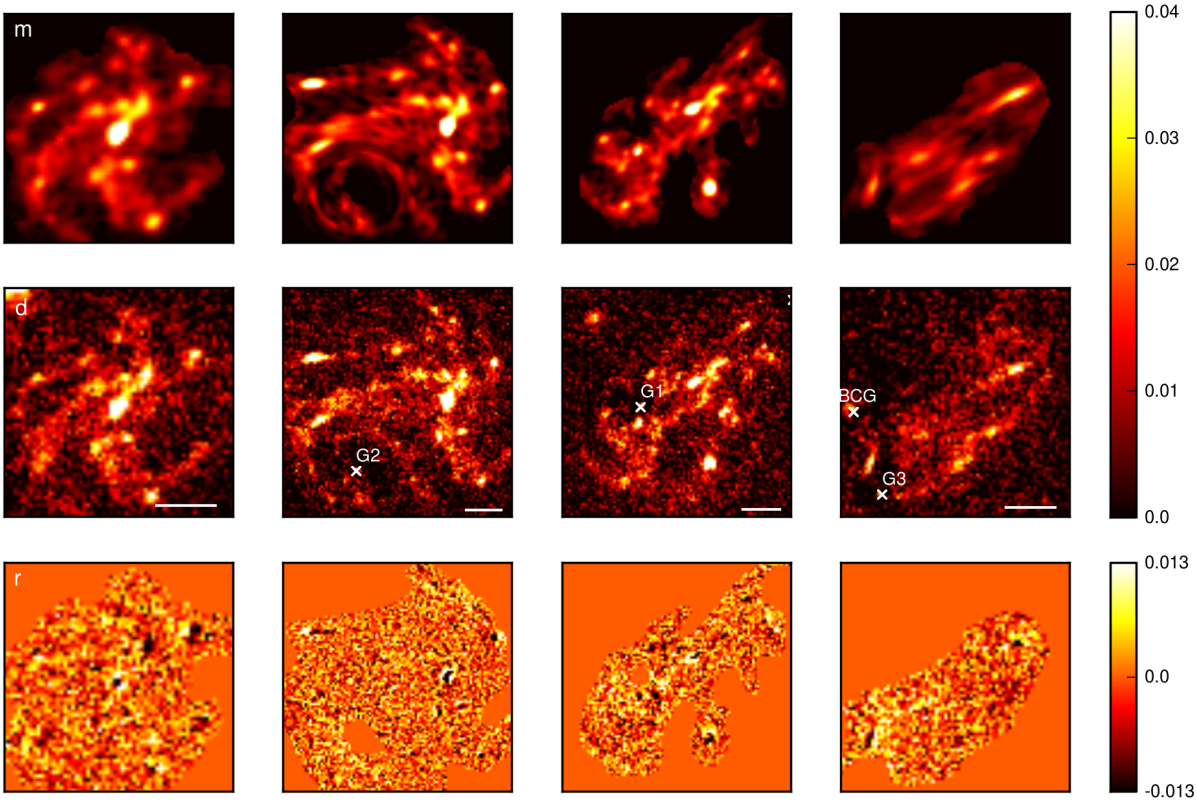

Figure 3.5: Results from the surface brightness modelling. Upper row is the model $\boldsymbol{m}$, middle row the observed data $\boldsymbol{d}$, lower row the residual $\boldsymbol{r} = \boldsymbol{d} - \boldsymbol{m}$. Columns from left to right are the main images 1.1, 1.2, 1.3.1 and 1.3.2. Colorscale of the residual is 2σ of the pixel noise on the image plane. Due to the high dynamic range of the source brightness distribution we use a gradient regularisation for the source brightness distribution during modelling. All features of the images are reproduced by our model down to the noise level except where the resolution of the data $\boldsymbol{d}$ is insufficient to capture the high dynamic range at the edges of the very bright source clumps. In each column, the scale of one arcsec is indicated by a white line.

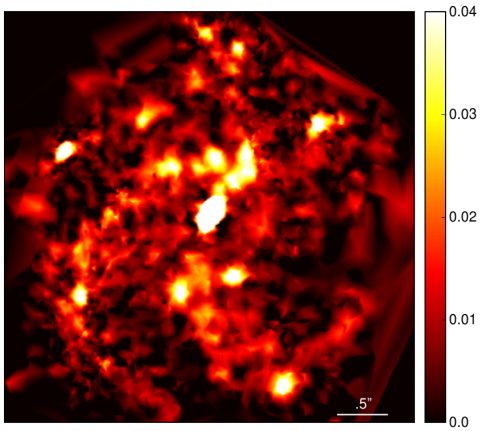

Figure 3.6: Reconstructed source brightness distribution. Colorscale is the same as in Fig. 3.5.

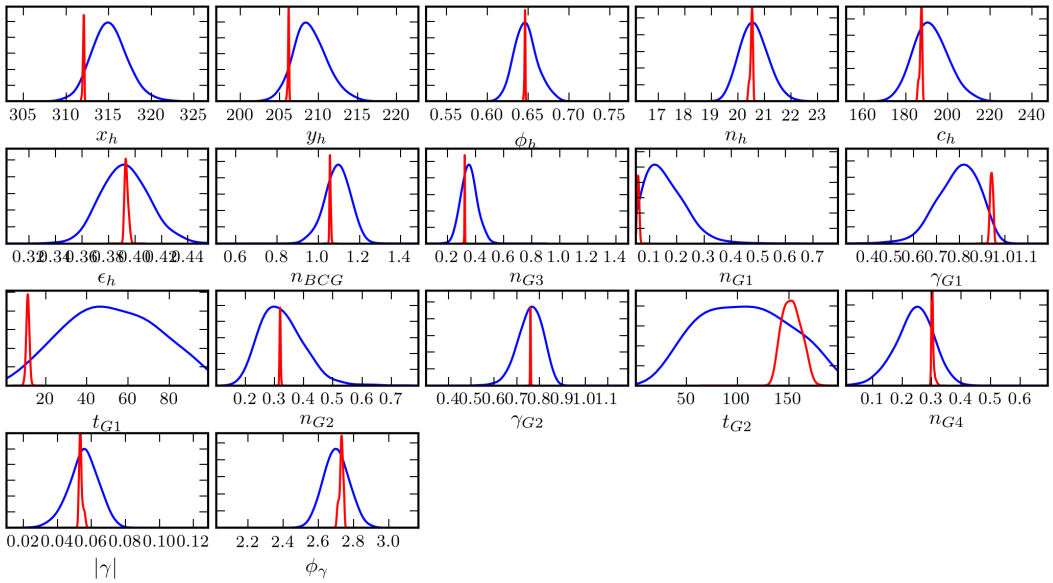

Figure 3.7: Marginalised likelihood for the model parameters from the position modelling in red, for the full surface brightness modelling in blue. Maximum likelihood parameters are consistent within the errors.

It is evident from the comparison of the brightness modelling with the position modelling in Fig. 3.7 and Tab. 3.3 that the best parameters agree within the error bars. The coordinates of the halo (x_h, y_h) are in pixel where one pixel corresponds to $65\mathrm{marcs}$ and the BCG is at $348.2, 213.7$. We focus on the modelling of the truncation and slope of two galaxies in more detail, G1 and G2, since for those galaxies there are constraints on a huge range of radii. For some parameters as for example for the truncation of galaxies G1 and G2, t_{G1} and t_{G2} position modelling is not sufficient to constrain the model values. Only the modelling of the full brightness distribution provides a detailed model.

3.7.3 Parameter Degeneracies

Our best model has 17 free parameters, 6 for the main DM halo, nine for the cluster galaxies and two for the external shear. In order to quantify the degeneracies among all parameters, we perform a full exploration of the parameter space with a Markov Chain Monte Carlo sampling. As an example we show in Fig. 3.8 the degeneracies for a selection of eight of those parameters. The most correlated pair of parameters of the main DM halo is the normalisation, n_h, and the core, c_h. Additionally we include the normalisation, the slope and the truncation radius for the lower substructure galaxy G2, see also Fig. 3.2. Note that we choose a flat prior between $1\mathrm{px} < t_{\mathrm{G2}} < 200\mathrm{px}$ $(0.065'' \text{ to } 13'')$ for the truncation of the substructure galaxy G2 spanning the whole range to the central images 1.3.1 and 1.3.2. In Fig. 3.8, we compare the confidence limits from brightness modelling (shaded contours) with the modelling based on bright image clump positions (green lines). For both models, we show the 68, 95 and 99.7 confidence levels (CL). The position based modelling works well for most parameters and gives a comparable best model. However, the improvement provided by the surface brightness modelling has a huge effect on the size of the confidence regions.

The most noticeable example is the truncation radius of the substructure galaxy, t_{G2} in the bottom row. Similarly to what was found by Suyu & Halkola (2010), the position modelling provides almost no constraints on the truncation radius. Therefore, the surface brightness modelling is crucial in order to constrain the truncation radius. Tight constraints on all galaxy parameters such as the normalisation, the slope and the truncation radius allow to constrain the total galaxy profile and therefore its size in detail. We find similar results for the modelling of galaxy G1. We have to keep in mind, however, that the confidence limits in Fig. 3.8 do *not* include systematic errors. Even though we get a very well constrained result from the surface brightness modelling, this result might be biased by the analytic form of the mass parametrization that we assume in Eq. (3.2). We refer to chapter 4 for a more thorough investigation of those effects.

3.7.4 Central Slope of the Total Mass Distribution

The upper panel of Fig. 3.9 shows our best central model of the the radial distribution of the mass density $\langle\rho\rangle$, averaged on circles centred on the BCG. The grey shaded areas indicate the radial coverage of the main images 1.1 1.2 and 1.3. Note, that the radial extent of images 1.1 and 1.2 overlaps. The three main images cover almost the entire range from $0.8'' - 22''$ $(5.3 - 145\ \mathrm{kpc})$. The top panel of Fig. 3.9 differentiates the contributions of the main dark matter halo, the BCG

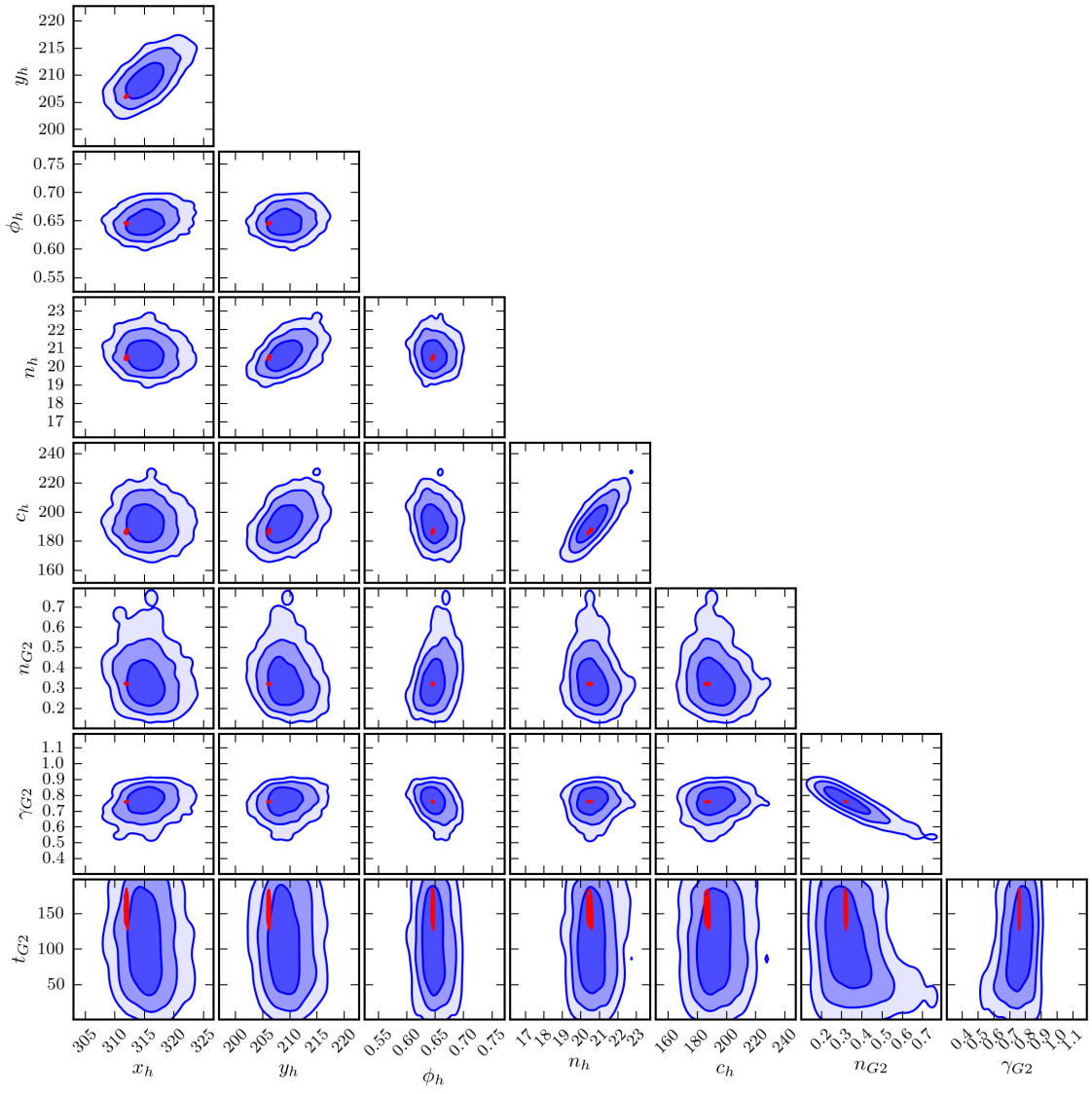

Figure 3.8: Improvement of the parameter estimation for the full surface brightness modelling compared to the position modelling for a selection of eight parameters. Brightness modelling tightly constrains all model parameters, even the truncation radius of the substructure galaxy G2 in the last row, which is not constraint by position modelling only.

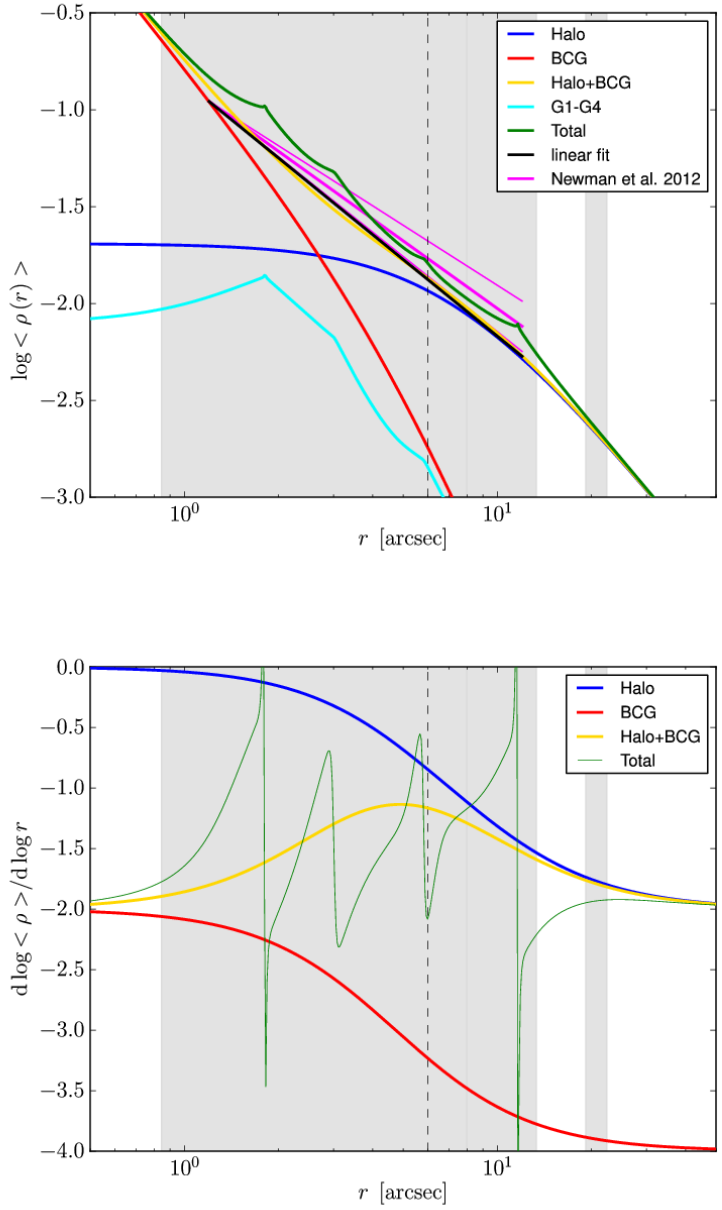

Figure 3.9: Top panel: radial distribution of the mass density $\rho(r)$. The constituents of the total mass profile are the main DM halo (blue), the BCG total mass (red) and smaller cluster galaxies (cyan). The DM halo has a large core of ~ 12 arcsec. Grey shaded areas show the radial coverage of the main image system 1. The black line is a linear fit in log-log space to DM halo+BCG mass density, for details see text. Vertical dashed line is the virial radius of the BCG. Bottom panel: non-averaged logarithmic slope of all components as a function of the distance from the BCG.

and the other cluster members, namely the galaxies G1 to G4. The central cusp of the total mass distribution for $r < 2.7''$ $(17.8\ \mathrm{kpc})$ is dominated by the profile of the BCG. The dark matter component of halo A has a large core and is flat out to $\sim 12''$ $(\sim 80\ \mathrm{kpc})$. Due to the unique mass distribution of MACS J1149+2223, the contribution of the other cluster galaxies G1 to G4 to the innermost radial mass distribution is also non negligible but does not significantly affect the inferred slope (see below).

We measure the 3D logarithmic slope $\gamma_{\mathrm{tot}} = \partial \log < \rho > / \partial \log r$ of the total mass distribution in the range from 1.2 to 12 arcsec (8 to $80\ \mathrm{kpc}$). For a half light radius of $\sim 6''$ of the BCG this corresponds to 0.2 to $2R_e$ which is the same range used by Newman et al. (2013). Note, that our surface brightness reconstruction of the cluster's main image system covers that whole range, therefore the reconstructed mass distribution is very well constrained. The straight black line in the upper panel of Fig. 3.9 is a linear fit in $\log \rho - \log r$ space (equally spaced in $\log r$) to the DM halo+BCG mass density distribution. Our model predicts a 3D logarithmic slope $\gamma_{\mathrm{tot}} \approx -1.32$. Our 2D total logarithmic mass density slope of $\gamma_{\mathrm{tot,2D}} \approx -0.3$ is between the values from two independent measurements by Smith et al. (2009) and Zitrin & Broadhurst (2009), (-0.36 and -0.24 respectively) and therefore confirms their calculations.

Newman et al. (2013) measure the total slope of the mass distribution (DM halo + BCG) for 7 massive clusters and find a mean central circularly averaged logarithmic slope $< \gamma_{\mathrm{tot}} >= -1.16$ with intrinsic scatter $\sigma_{\gamma,\mathrm{tot}} = 0.13\ (68\%\mathrm{CL})$. Those values are shown as a comparison in Fig. 3.9 as magenta lines. The extent of the lines is the region over which the radial slope is fitted, the y-offset is adapted to our best linear fit. Our total density slope is consistent (within $1.2\sigma_\gamma$ but slightly steeper than what Newman et al. (2013) found.

A certain difference is to be expected considering there are differences between MACS J1149+2223 and the cluster sample from Newman et al. (2013): MACS J1149+2223 with a mass of $M_{200} \sim 5 \times 10^{14}\mathrm{M}_\odot$ is at the lower end of the mass range $0.4 < M_{200}/10^{15}/\mathrm{M}_\odot < 2$. The cluster is at higher redshift z = 0.54 compared to their sample ($0.2 < z < 0.3$) and Newman et al. (2013) choose relaxed clusters. In contrast, there are several indications that MACS J1149+2223 is not yet fully relaxed. The main indications are: a) the offset between the BCG and the cluster centre, b) the high ellipticity of the cluster mass distribution, c) close-by massive galaxies or groups of galaxies, B, D and E in Fig. 3.1 and d) a non relaxed X-ray emission (see for example Fig. 3 in Smith et al. (2009)).

The green line in the top panel of Fig. 3.9 additionally includes the mass distributions of the four central galaxies G1 to G4. In the radial range from $1.2''$ to $12''$ where we measure the DM halo+BCG mass density slope, the galaxies considerably contribute to the total mass distribution. The DM halo+BCG+Galaxies density slope $\gamma_{tot+G} = -1.41$ is steeper than that of the DM halo + BCG alone ($\gamma_{tot} = -1.32$). However, the four galaxies G1 to G4 are arranged in a way that even though the contribution to the total mass density is important, the total density slope is still within 2σ of the DM halo+BCG measurement of Newman et al. (2013). In order to estimate the scatter in the slope measurement due to the galaxy subhalo population, we exclude some of the galaxies. If for example only the innermost galaxies G3 (G3+G4) were included, the averaged total density slope would be increased -1.44 (-1.48). Equivalently, including only the more distant galaxies G2 and G1, the total density slope would become more shallow (-1.24).

Our main goal was to constrain the evolution of the BCG and its interaction with the DM halo

during cluster formation by measuring the total density slope of the cluster. If there are cluster galaxies very close to the cluster centre, their contribution to the total potential in which the stars of the BCG form is non-negligible. It is therefore important to accurately model and to include the mass distribution of cluster member galaxies, in order to tightly constrain on the total mass distribution.

The lower panel of Fig. 3.9 shows the non-averaged logarithmic slope for each of the mass components of the cluster. Without BCG velocity dispersion measurements for MACS J1149+2223 it is not straightforward to separate DM and stellar mass content of the BCG. However, Zitrin & Broadhurst (2009) find a total BCG mass of $\sim 1 \times 10^{12} \mathrm{M}_{\odot}$ which is identical to what we find. They claim that the mass to light radius of $M/L_B = 4.5$ can be explained by the stellar content of a single burst stellar population formed at redshift $z = 3$ and a mean half solar metallicity. Under this assumption, the central logarithmic slope of the dark matter content of MACS J1149+2223 , the blue line in the lower panel of Fig. 3.9 is shallower than the NFW profile. In fact the central DM density ist flat for $r < 20\ \mathrm{kpc}$. This is a strong indication that in the case of MACS J1149+2223 the baryons at the cluster centre flatten the dark matter with respect to what is expected for galaxy clusters ($\gamma_{\mathrm{DM}} \sim -1$) from purely dark matter simulations (Diemand et al. (2004); Springel et al. (2001, 2005); Merritt et al. (2006); Gao et al. (2012)).

3.8 Conclusions

We presented a new and detailed model for the centre of the galaxy cluster MACS J1149+2223. The central image system 1 is one of the largest known lensed images to date. A source with unprecedented contrast of starforming regions in the spiral arms is lensed in a unique triple image configuration. The first image is an almost undisturbed magnified image of the source. The second image would be almost uniformly stretched as well, but the cluster galaxy G2 on top of the image lenses the lower spiral arm of the source into a 'substructure' Einstein ring. The central image of MACS J1149+2223 covers all of the cluster centre where parts of the source are split again by the cluster galaxy G1.

- In this paper we identify more than twice the constraints in the main system 1 than those previously known. Due to these new constraints, we are able to constrain three important details of the mass distribution, the mass distributions of two cluster galaxies G1 and G2 and due to the analysis of the detailed morphology of image 1.3.2, the total mass distribution of the cluster at the innermost radii.

- We find two models with different ellipticity, one for the central region of the cluster and one at larger radii.

- Our best central model from position modelling improves the image plane RMS of the multiply lensed images to $0.069\ \mathrm{arcsec}$.

- We perform the first ever detailed brightness reconstruction of system 1 in this galaxy cluster. Our residuals of the surface brightness modelling are close to the noise level of the HST CLASH observations.

- The confidence regions of the full surface brightness reconstruction are significantly improved compared to the simpler position modelling.
- The unique constraints of MACS J1149+2223 allow to measure the substructure galaxy profile in detail. Two Galaxies, G1 and G2, are modelled with a variable slope profile. We recover the central 2D logarithmic slopes $\gamma' = \partial \log(\kappa) / \partial \log R = -1.88$ and -1.52 for G1 and G2 respectively.
- Our mass model predicts a central DM halo with a large ~ 12 arcsec core while the total mass profile at the very centre of the cluster is dominated by the BCG. We find a central logarithmic slope of the 3D total mass distribution $\gamma'_{\rm tot} = \partial \log(\rho) / \partial \log r = -1.32$ for the DM halo+BCG and -1.41 for the DM halo+BCG+Galaxies mass distribution.

Chapter 4

Lensing Model of MACS J1149+2223 II: The Profiles of Cluster Galaxies

S. Rau,[1] S. Vegetti,[1] S. D. M. White [1]
in preparation for publication

ABSTRACT

In groups or clusters of galaxies, galaxies are expected to be tidally truncated compared to isolated field galaxies. We therefore measure the mass distribution of two galaxies in the strong lensing cluster MACS J1149+2223. The constraints on the galaxy mass distribution from the main multiple image system of MACS J1149+2223 cover almost the entire range from $0.4''$ to $23.4''$ ($0.5''$ to $32.6''$) from the centre of the galaxies G1 and G2 respectively. By comparing their Bayesian evidence, we rank three analytic galaxy profiles for each substructure galaxy, a Pseudo Jaffe, a NFW and a power law profile with a variable slope. Both galaxies are best described by the latter profile, however the differences in evidence between the models are small. From the three profiles we robustly measure the mass within the Einstein radius, 7.3 ± 0.02 and $15.9 \pm 0.2 \times 10^{10}\mathrm{M}_{\odot}$ for G1 and G2 respectively, while we determine a relatively large systematic error for the the measurement of the total galaxy mass due to uncertainties at large radii. The total slope of the projected galaxy mass distribution for all models is found to be significantly steeper than isothermal. We find a projected logarithmic slope at the Einstein radius of $\partial \log(\kappa) / \partial \log R = -3.2$ and -1.8 for the galaxies G1 and G2 respectively. This clearly indicates a truncation of the mass distribution of both galaxies. The mass distribution of galaxy G1 which is located very close ($\sim 4.2''$) in projection to the cluster centre in particular is extremely truncated and more than 95% of the galaxy mass is within the Einstein radius.

[1]Max-Planck Institute for Astrophysics, Karl-Schwarzschild Str. 1, D-85748, Garching, Germany

4.1 Introduction

The results from recent studies of *isolated field* gravitational lens galaxies agree on a more or less isothermal mass density slope. Koopmans et al. (2006) found a total density slope for the SLACS lenses of $\langle\gamma'\rangle = 2.01^{+0.02}_{-0.03}$ (68 % CL) where $\rho_{\rm tot} \propto r^{-\gamma'}$ within an average Einstein radius of $4.2\,\mathrm{kpc}$. They analysed a sample of 15 massive early type galaxies and included stellar velocity dispersion measurements. Sonnenfeld et al. (2013) model the lensing measurements and the stellar kinematics of the lenses in the SL2S sample with a power law mass distribution. Combined with LSD and SLACS lenses, they found an average density slope of $\gamma' = 2$, with weak dependencies both on the surface stellar mass density $\partial\gamma'/\partial\Sigma_* = 0.38$ where $\Sigma_* = M_*/2R^2_{\rm eff}$ and on redshift with $\partial\gamma'/\partial z = -0.31$. Including those dependencies, they find a scatter of $\sigma_{\gamma'} = 0.12$ for the slope of the power law of the galaxy mass distributions. The small scatter in the observations might indicate a coupling of dark matter and baryonic matter during the formation of the galaxy halos. The measurements of the galaxy mass distributions in these studies of isolated field galaxies are limited to radii where the observations provide reliable constraints, that is, on scales of the Einstein radius and the Effective radius of the galaxies.

During the formation of more massive structures, satellite galaxies merge with groups or clusters of galaxies. Due to the tidal interaction during the process of merging, the mass of galaxies gets stripped (Merritt, 1983, 1984, 1985). Early N-body simulations that follow the assembly of structure found that this effect depends on the local mass density of the galaxy's environment (Ghigna et al., 1998). This might also be related to the fact that subhalos at the centre of a cluster typically were accreted earlier (Gao et al., 2004) and therefore spent longer time in a denser environment. Diemand et al. (2007) use the Via Lactea simulation of a Milky Way size galaxy and find an outside-in removal of subhalo mass and therefore find strongly increased subhalo concentrations close to the centre of the host. In two high-resolution hydrodynamical simulations of COMA and VIRGO size clusters, Limousin et al. (2009) find that the stripping preferentially affects the more extended DM galaxy mass component, whereas the stellar component remains more ore less intact. This is supported by Gao et al. (2012) who resimulate nine clusters in high resolution taken from the Millennium simulation (Springel et al., 2005). The peak circular velocity of the subhalo population remains almost unchanged while the radius at which it is reached shifts to the subhalo centre compared to more isolated subhalos in the same simulations.

The truncation of galaxy halos in observed cluster lenses has first been studied with weak galaxy-galaxy lensing (Natarajan et al., 2002, 02b; Limousin et al., 2007; Natarajan et al., 2009). This statistical method describes the properties of a fiducial galaxy substructure halo, assuming scaling relations with galaxy luminosity for all cluster galaxies. Limousin et al. (2007) find an upper limit on the truncation radius of the galaxies in Abell 383 of $50\,\mathrm{kpc}$ for a pseudo isothermal mass distribution (compare Eq. (4.2)) while they infer the truncation radius to be larger than 'a few hundreds of kpc' for field galaxies. In order to study the dependence of galaxy truncation with radius, Natarajan et al. (2009) divide the galaxies in the cluster Cl 0024+16 in three radial bins and use galaxy-galaxy lensing to derive parameters for a fiducial substructure galaxy in each bin. They find an increasing mass of a typical $L*$ early type galaxy host with increasing radius, indicating an increased truncation of galaxies closer to the cluster centre.

The reconstruction of the mass distribution in galaxy clusters relies on a high quality cluster

model. Halkola et al. (2007) use their *strong lensing* mass reconstruction of Abell 1689 based on image positions (Halkola et al., 2006) and find strong evidence for the truncation of the scaled galaxy cluster halos. Additional measurements of galaxy truncation were reported from Richard et al. (2010) who individually modelled the velocity dispersion and the truncation of a single galaxy in Abell 370 and from Donnarumma et al. (2011) who model six galaxies individually in Abell 611, however, both analysis are based on multiple image positions. For the detailed mass reconstruction of a cluster galaxy it is necessary to use many constraints on different radii. Suyu & Halkola (2010) therefore used the full surface brightness distribution in a group scale halo to measure the truncation radius of a satellite galaxy. Only due to the position of this satellite on top of the Einstein ring and due to the fact that the truncation radius is smaller than the length of the Einstein ring, Suyu & Halkola (2010) were able to constrain the satellite mass distribution in detail. Recently, Eichner et al. (2013) used the full surface brightness information of the giant arc in MACS 1206 to constrain the mass distribution of five galaxies that lie close to the arc. However, due to the increased difficulty in modelling the full surface brightness information in a cluster and since each of the galaxies is only constrained on a small scale, they enforce scaling relations for the truncation of the five galaxies. During modelling of the five galaxies and surface brightness optimisation they fix the other cluster parameters. They derive a scaling of the truncation with velocity dispersion according to $r_t = (35 \pm 8)\mathrm{kpc} \times (\sigma/186\mathrm{kms}^{-1})^{4/3}$.

In our full surface brightness reconstruction of the multiple images in the cluster MACS J1149+2223 in chapter 3, we have seen that there are two cluster galaxies located on top of the extended main lensed system 1. Due to this fortunate position, the main multiple image system in MACS J1149+2223 provides constraints on the galaxy mass distribution on a large range of radii. They almost continuously cover the range from $0.4''$ to $23.4''$ ($0.5''$ to $32.6''$) from the centres of the galaxies G1 and G2 respectively. This allows us to tightly constrain the mass distribution of those two galaxies. For galaxy lensing mass reconstructions, the most widespread assumption is a Pseudo-Isothermal profile (e.g. Suyu & Halkola (2010); Donnarumma et al. (2011); Eichner et al. (2013)) for the galaxy mass distribution. However, depending on the severity of the truncation, this profile might not accurately reflect the true mass distribution. In order to test for systematic effects involved by choosing an analytic mass profile, we test in this chapter three different analytic mass profiles for each galaxy.

This chapter is ordered as follows. We first give a short overview of the cluster MACS J1149+2223 and explain the different analytic galaxy models in Sec. 4.4.2. We then describe the Bayesian method for ranking those models in Sec. 4.3. We rank the different galaxy models in 4.4.1 and analyse the mass distributions and the projected slope of the mass distributions of the galaxies in Secs. 4.4.2 and 4.4.3.

We assume a Planck cosmology, $H_0 = 67.3$ and $\Omega_m = 0.315$ throughout the paper. The cluster is at, $z = 0.544$ where one arcsec corresponds to 6.6 kpc. The redshift of the source of the multiple images in this chapter is $z = 1.52$.

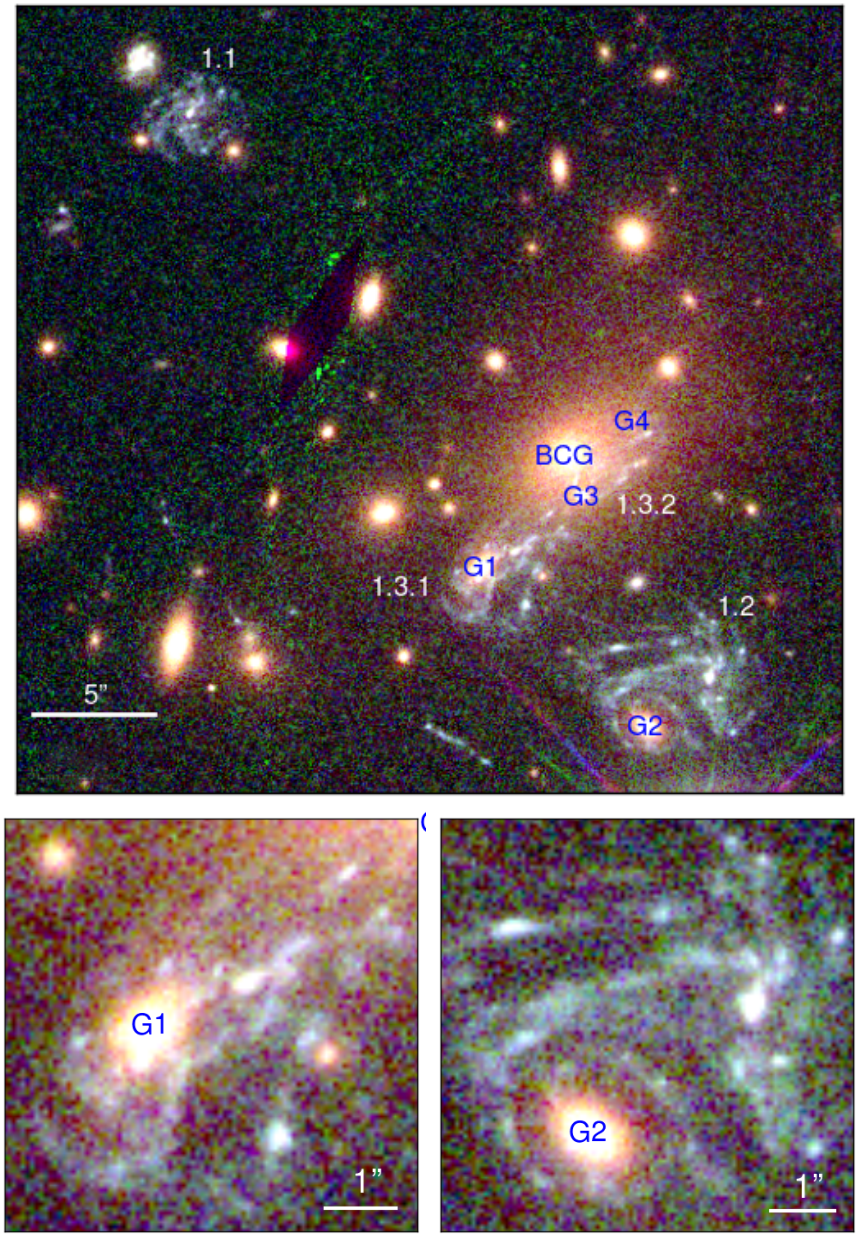

Figure 4.1: RGB colour image of the HST F814W/F606W/F555W 65 marcs observation of the triple imaged spiral source galaxy at the centre of the cluster MACS J1149+2223. The cluster centre of our best model is at $(-2.34'', +0.49'')$ from the BCG. We focus on two cluster galaxies, G1 additionally multiply lenses bright source clumps close to the centre of the cluster and G2 at the centre of an substructure Einstein ring with distinctly separated images.

4.2 The Mass Model

MACS J1149+2223 is a galaxy cluster situated at redshift $z = 0.54$. The main image system consists of three images of a large spiral source galaxy situated at redshift $z = 1.52$, images 1.1, 1.2 and 1.3 in Fig. 4.1. In chapter 3 we presented a detailed lens model of the mass distribution of the cluster and its galaxies and we refer to that chapter for details on the lens modelling. In this chapter we extend the analysis of the cluster mass distribution. In chapter 3, we found a parametric model that not only accurately reproduces the multitude of strong lensing positional constraints of the main lensed image system, we also performed a full surface brightness reconstruction.

In this chapter, we focus in particular on two member galaxies, G1 and G2. Both galaxies are strongly lensing several bright source clumps of the grand spiral galaxy in two highly magnified and distorted Einstein rings shown in the lower panels of Fig. 4.1. Due to their position close to the cluster centre, both galaxies strongly affect the total cluster mass distribution and therefore the morphology of lensed images. This particular lensing configuration provides tight constraints on the galaxy mass profile from the respective Einstein radii out to distances as large as $23(32)''$ $(150\ (215)\ \mathrm{kpc})$ from the respective centre of galaxy G1 and G2. Since we are interested in quantifying the robustness of galaxy size measurement obtained via strong lensing modelling, we consider here three different models for the mass density distribution of each of the two galaxies and compare five models in terms of their Bayesian evidence in Sec. 4.4.1.

All three profiles are smoothly truncated and extend to infinity. However, they all have a finite total mass. As a measure of the size of the two cluster galaxies, we use the 2D logarithmic slope of the mass density profiles,

$$\gamma'(R) = \frac{\partial \log[\kappa(R)]}{\partial \log R}. \tag{4.1}$$

This measure is independent of the analytic galaxy profile and is therefore ideal to compare the results of the three different models.

One of the most widely used mass density parametrization (e.g. Suyu & Halkola (2010); Donnarumma et al. (2011); Eichner et al. (2013)) is the so-called Pseudo-Jaffe (hereafter PJ) profile. It is a spherical smoothly truncated version of the isothermal profile and is defined by the following dimensionless surface mass density,

$$\kappa(R) = n\left(\frac{1}{R} - \frac{1}{\sqrt{R^2 + t^2}}\right), \tag{4.2}$$

here n is the normalisation, R the 2D projected radius and t the truncation radius. This model has a central 2D logarithmic mass density slope of $\gamma' = -1$ for $R << t$ and steepens due to the smooth truncation to $\gamma' = -3$ at large radii $R >> t$.

Another profile which is commonly used in strong lens modelling is a softened elliptical power-law model, that we here modify to explicitly include the effect of truncation. In detail, we

use the following 3D profile,

$$\begin{aligned} \rho(r) &= \tilde{n}\left[\left(r^2+c^2\right)^{-\gamma-1/2}-\left(r^2+t^2\right)^{-\gamma-1/2}\right] \\ \text{where} \quad \tilde{n} &= n\frac{\Sigma_{\rm c}\Gamma\left[\gamma+1/2\right]}{\sqrt{\pi}\Gamma\left[\gamma\right]}. \end{aligned} \tag{4.3}$$

Here, c is the core radius, we choose $c = 6.5 \times 10^{-6}$ arcsec, t denotes the truncation radius and γ the variable 2D slope of the mass distribution. This profile is equivalent to the projected 2D density profile (hereafter SL),

$$\kappa\left(R\right) = n\left[(R^2+c^2)^{-\gamma}-(R^2+t^2)^{-\gamma}\right]. \tag{4.4}$$

The extra parameter of the SL model allows to vary the central slope γ' where $\gamma' = -2\gamma$ for $c << R << t$. At *very* small radii $R << c$ the core takes over, $\gamma' = 0$, while at large radii $R >> t$ the profile falls off as $\gamma' = -2\gamma + 2$.

Finally, a truncated version of the the NFW (Navarro et al., 1997) profile was recently introduced by Baltz et al. (2009) with the following 3D mass density distribution

$$\rho(r) = \frac{M_0}{4\pi}\frac{1}{r\left(r+r_s\right)^2}\left(\frac{t^2}{r^2+t^2}\right)^n, \tag{4.5}$$

where r_s is the scale radius and and the truncation radius r_t is a factor t larger than the scale radius, $t = r_t/r_s$. For this profile, the sharpness of the truncation can be controlled with the parameter n. We choose $n = 1$ for our purposes which falls off as sharp as r^{-5} for $r > r_t$. The 2D logarithmic slope of the projected NFW model varies between $\gamma' = 0$ for $R << r_s$ and $\gamma' = -2$ for $r_s < R < r_t$ and is strongly truncated for $R >> r_t$ with a slope $\gamma' = -4$. For details of the model, the comparison with the original NFW profile and the expression for the projected mass, we refer to Baltz et al. (2009).

We performed tests to identify the parameters that influence the modelling result and that are constrained by the data. In the final modelling, we therefore kept the centroids of the two galaxy mass distributions for galaxies G1 and G2 fixed at the centre of the respective light distribution, and we assume a circular symmetric mass distribution for both substructure galaxies.

4.3 Method

In this section we extend the method described in chapter 3. Here, we do not only want to find the best model parameters, but we also want to compare different substructure models. We therefore calculate the evidence

$$P\left(\boldsymbol{M}|\boldsymbol{d},\boldsymbol{R}\right) \propto P\left(\boldsymbol{d}|\boldsymbol{M},\boldsymbol{R}\right)P\left(\boldsymbol{M}|\boldsymbol{R}\right). \tag{4.6}$$

Here $\boldsymbol{M}$ is the lensing model, that is the analytic cluster mass parametrization, $\boldsymbol{R}$ is the gradient source regularisation and $\boldsymbol{d}$ is the observed data. Since we do not prefer any model we choose

G2 Parameter	PJ	SL	NFW
$n_{\rm G2}$	0.98	0.32	3.34
$\gamma_{\rm G2}$	-	0.76	-
$r_{s,\rm G2}$ [$''$]	-	-	0.13
$t_{\rm G2}$	$1.35''$	$9.02''$	139.4
$M_{\rm tot,G2}$ [10^{10} M$_\odot$]	27.7	40.2	35.8
$M^{\rm 2D}_{\rm G2}\,(<\theta_e)$ [10^{10} M$_\odot$]	16.1	15.6	16.0
$\log\,({\rm EV})$	-22629	-22611	-22612
$\Delta\log\,({\rm EV})$	-18	0	-1
P	56758	56764	56760
ΔP	-6	0	-4

Table 4.1: Best model parameters, total masses and masses within the Einstein radius for the three models for substructure galaxy G2. The size of each galaxy model can *not* directly be inferred from the numerical values of t (see Eqs. 4.2 to 4.5). The last four columns contain the absolute and relative-to-best evidence values (EV) and a relative and absolute goodness-of-fit parameter (P) for the three models. Best model for galaxy G2 is the SL model.

a flat prior $P\,(\boldsymbol{M}|\boldsymbol{R})$. We compare the five different models via the marginalisation of the likelihood $P\,(\boldsymbol{d}|\lambda_s,\boldsymbol{\eta},\boldsymbol{M},\boldsymbol{R})$ over the full parameter space of the model parameters $\boldsymbol{\eta}$,

$$P\,(\boldsymbol{M}|\boldsymbol{d},\boldsymbol{R}) \propto \int {\rm d}\boldsymbol{\eta}\, P\,(\boldsymbol{d}|\boldsymbol{\eta},\boldsymbol{M},\boldsymbol{R})\, P\,(\boldsymbol{\eta})\,. \tag{4.7}$$

We use flat priors for the model parameters $\boldsymbol{\eta}$. Note, that in this formulation those models are preferred that give acceptable results over bigger parameter volumes. Additionally, Occam's Razor is already included. Between two models that fit equally well, the more complicated one is disfavoured. For a detailed derivation of the method see Vegetti & Koopmans (2009) or Suyu et al. (2006).

4.4 Results

The best modelling parameters for the main cluster do not vary significantly for the different galaxy models. We therefore refer to chapter 3 for a detailed description of our best model and of the main cluster parameters. Our best reconstructed cluster has a flattening of $\epsilon = b/a \sim 0.4$ and the central DM halo has a $\sim 12\,''$ core. We find a 2D slope of $\gamma' = \partial\,\langle\kappa_{\rm tot}\rangle\,/\partial R = -0.32$ for the circularly averaged *total* cluster mass distribution in the range from 1.2 to 12 arcsec. The best model parameters for the cluster galaxies G1 and G2 are summarised in Tab. 4.2 and Tab. 4.1 respectively. In the next section we compare the different galaxy models via their evidence values. The evidence in Eq. (4.7) is calculated by a nested sampling integration over the parameter space of $\boldsymbol{\eta}$. This method estimates the integral by randomly sampling equal likelihood shells (Skilling, 2004). For the evidence evaluation, we use the parallel, publicly available library MultiNest (Feroz & Hobson, 2008; Feroz et al., 2009, 2013).

G1 Parameter	PJ	SL	NFW
$n_{\rm G1}$	2.88	0.063	108.04
$\gamma_{\rm G1}$	-	0.934	-
$r_{s,\rm G1}$ [$''$]	-	-	0.00051
$t_{\rm G1}$	$0.13''$	$0.72''$	1943.45
$M_{\rm tot,G1}$ [10^{10} M$_\odot$]	7.8	7.55	7.54
$M^{\rm 2D}_{\rm G1}$ ($<\theta_e$) [10^{10} M$_\odot$]	7.35	7.32	7.31
$\log(\rm EV)$	-22612	-22611	-22613
$\Delta\log(\rm EV)$	-1	0	-2
P	56756	56764	56759
ΔP	-8	0	-5

Table 4.2: Same as Tab. 4.1 but for galaxy G1.

Parameter	G2	G1
$\theta_{\rm E,cl}$	1.3" (8.6 kpc)	1.17" (7.7 kpc)
$\theta_{\rm E}$	0.75" (5 kpc)	0.52" (3.4 kpc)
$R_{\rm eff,V}$	0.4" (2.6 kpc)	0.26" (1.75 kpc)
$M(<\theta_e)$	15.9 $\pm$ 0.2	7.3$\pm$0.02
$M_{\rm tot}$	34.6 $\pm$ 5.2	7.6$\pm$0.12
M_*	4.7	5.0
$M_*/M_{\rm tot}$	0.14	0.66
$\gamma'(\theta_E)$ (2D)	-1.8	-3.2

Table 4.3: Einstein radius as boosted by the cluster, and Einstein radius for the same galaxies without the cluster, effective radii of the galaxies, masses within the Einstein radius, total masses, stellar masses and central slopes as calculated from the parametric models. Masses are in 10^{10}M$_\odot$. Systematic uncertainties are derived from the three different models.

4.4.1 Model Ranking

Tables 4.1 and 4.2 contain the logarithmic evidence values, $\log(\rm EV)$, for the different analytic cluster galaxy models. The best model for both galaxies, G1 and G2, is a smoothly truncated power law model with variable slope, Eq. (4.4). The eighth row in both tables, $\Delta\log(\rm EV)$, contains the logarithmic evidence values of all other models relative to this best model. The last two rows contain an absolute and a relative goodness-of-fit parameter, the posterior P calculated from Eq. (3.9).

In the case of galaxy G2, all three different analytic models perform almost equally well in modelling the galaxy mass distribution, in terms of the evidence values in Tab. 4.1. There is a slight preference for the two models with one additional free parameter, the SL and NFW models. Analysing the last two rows that contain the absolute and relative goodness-of-fit parameter, we come to the same conclusion. Therefore the model ranks remain if we consider the goodness-of-

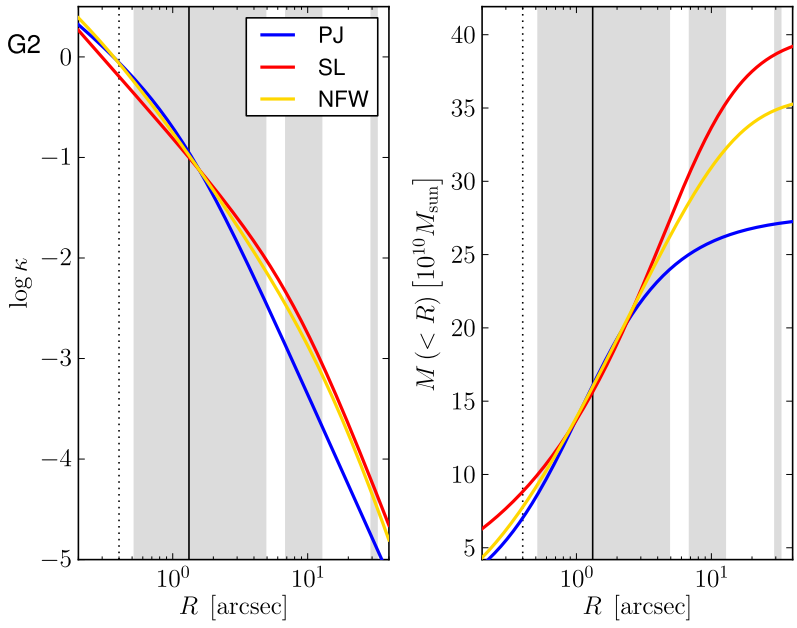

Figure 4.2: The three substructure mass models for galaxy G2. Blue solid line is the isothermal model, red the variable slope model and gold the NFW profile. Radial distribution of the scaled projected surface mass density, κ, in the left panel and the 2D integrated mass in the right panel. The critical line measured as the average separation of the additional multiple images forming the substructure Einstein ring lensed by G2 is shown as a vertical black line. This Einstein radius is boosted due to the lensing signal by the cluster. Grey shaded background regions show the position of the main multiple images in MACS J1149+2223, indicating the position of the constraints.

fit and neglect different number of freedoms or respective prior volumes.

All three models also perform equally well in modelling the galaxy G1, see Tab. 4.2. In the case of G1, the evidence for the PJ model is almost identical to the SL model ($\Delta \log(\mathrm{EV}) = -1$), even though the goodness-of-fit is slightly worse ($\Delta \mathrm{P} = -8$). This is an indication that the model ranking prefers the simpler PJ model, even though the fit is not as good.

4.4.2 The Mass Distribution of the Galaxies G2 and G1

In this section we investigate the mass density profiles of the three models (PJ, SL, NFW) for the galaxies G1 and G2. Table 4.3 summarises the Einstein radii, the effective radii, the galaxy masses, the total mass, the estimated stellar mass and the slope of the mass distribution at the Einstein radius. The stellar mass was estimated (Jing Wang, private comm.) from the magnitudes from a fit to the galaxy luminosity distributions with galfit (Peng et al., 2002) to the CLASH

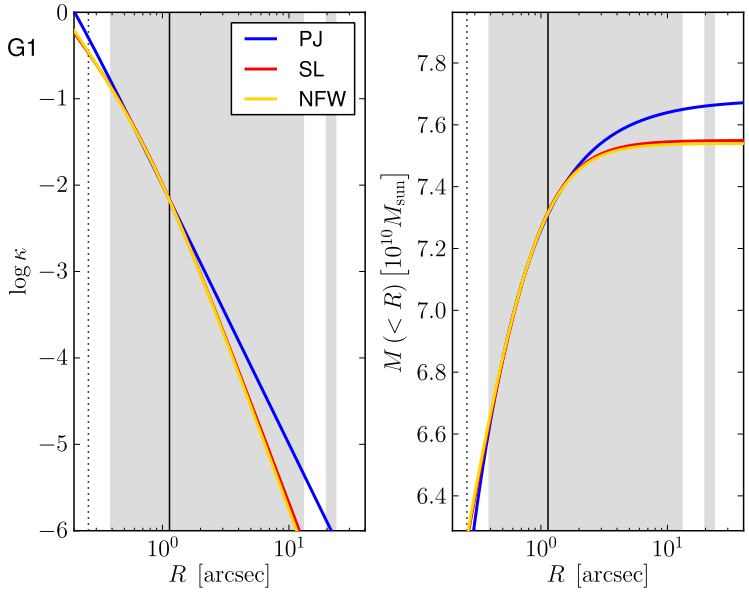

Figure 4.3: Same as Fig. 4.2 but for galaxy G1.

observations, assuming a Kroupa initial mass function, the SDSS g and r bands were used to calculate the M^* following Bell et al. (2003).

Figure 4.2 shows the radial projected mass density profile $\log \kappa(R)$ of galaxy G2 in the left panel and the integrated mass $M\,(< R)$ as a function of radius in the right panel. We also show the effective radius as a vertical dotted line and the Einstein radius of galaxy G2 as a vertical solid black line. This is the apparent Einstein radius of the Einstein ring in the bottom right panel of Fig. 4.1. Note, that this 'effective Einstein radius' $(\approx 1.3\,\mathrm{arcsec})$ is boosted by the cluster lensing signal and it is not the Einstein radius the galaxy G2 would have $(\approx 0.75\,\mathrm{arcsec})$ without the proximity to the massive cluster. The grey shaded regions in Fig. 4.2 show the radial extent of the multiple images of system 1 measured from the centre of galaxy G2. At radii $0.5'' < r < 32.6''$ $(\approx 3.4 - 215\,\mathrm{kpc})$ our strong lensing modelling is constrained. There is no information for radii smaller than $\approx 0.5\,\mathrm{arcsec}$ since there are no lensed images within the Einstein radius and there are some uncertainties and residuals from the subtraction of the light distribution of the galaxy itself at these innermost radii.

The lower image 1.2 of the main multiple image system of MACS J1149+2223 in Fig. 4.1 covers the radial range from 0.5 to $5\,\mathrm{arcsec}$ distance from G2. Over this range, both, the projected surface mass density κ and the integrated mass are almost identical for all three profiles for galaxy G2 in Fig. 4.2. We find a mass of galaxy G2 of $15.9 \pm 0.2 \times 10^{10}\mathrm{M}_\odot$ within the Einstein radius. The error corresponds to the results from the three analytic mass profiles. The asymptotic total masses in the rightmost panel are 27.7, 35.8 and $40.2 \times 10^{10}\mathrm{M}_\odot$ for the PJ, the NFW and the SL model respectively (see also Tab. 4.3). They differ by up to $1.2 \times 10^{11}\mathrm{M}_\odot$ (45 %) for the

three profiles. We have seen that despite these large differences in the total masses of the models, the lensing reconstruction is equally good (Sec. 4.4.1). The explanation is found in the way the reconstruction algorithm weights the different modes of the mass distribution, the profile, the integrated mass and the slope. Close to the galaxy, the effect on the image morphology due to the galaxy lensing signal is high and there are more constraints densely close-by. At radii $r > 5''$ the effect of the difference in total mass $\Delta M \sim 1.2 \times 10^{11} \mathrm{M}_{\odot}$ is spread out over a large area and therefore does not affect the deflection angles and therefore the modelling measurably. In other words, the data is not able to distinguish the three models by their different the total masses.

Being less conservative, we *can* use the small differences in evidence in Tab. 4.1 to discriminate between the three models. Since SL and NFW model perform equally well we determine a systematic error of $(40.2 - 35.8) \times 10^{10} \mathrm{M}_{\odot}$. We therefore find a total mass of galaxy G2 of $38 \pm 4 \times 10^{10} \mathrm{M}_{\odot}$.

Figure 4.3 shows the mass density profile and the integrated mass for Galaxy G1. The qualitative behaviour is the same as for galaxy G2. The profile, the slope and the mass within the Einstein radius $(1.13'')$ agree for all models $M(< \theta_e) = 7.3 \pm 0.02 \times 10^{10} \mathrm{M}_{\odot}$. However for a total mass of $7.6 \pm 0.12 \times 10^{10} \mathrm{M}_{\odot}$ we find that the mass contained within the Einstein radius is $7.3 \pm 0.02 \times 10^{10} \mathrm{M}_{\odot}$. Therefore, a fraction of 95% of the mass of galaxy G1 is within the Einstein radius. This is found independently from all three galaxy mass profiles. The total mass of the galaxy again is not perfectly constrained, see also Tab 4.2, however the differences between the models here are small. As discussed above, this does not affect the overall performance of the model in terms of the total evidence. We robustly find a very compact mass distribution of the galaxy G2.

4.4.3 The Slope of the Galaxies G2 and G1

All three analytical galaxy models, PJ, SL and NFW in Eqs. (4.2-4.5) allow a varying slope of the mass distribution with radius during modelling. In this section we extend the analysis of the projected galaxy mass distribution from the last section to the logarithmic slope of the different parametrizations in Eq. (4.1).

Figure 4.4 shows the logarithmic 2D slope for our three best models for galaxy G2. Grey rectangles show the radial range constraint by multiple image data, compare with Fig. 4.2. As a guide, we also show the 2D slope of a non-truncated isothermal profile with $\kappa \propto 1/r$ as a horizontal green line. Our PJ model for galaxy G2 is a truncated isothermal profile with a truncation radius of $t \approx 1.5''$. Due to this truncation, the mass distribution of the PJ model is steeper than an isothermal mass distribution on scales comparable to the Einstein radius (black vertical line). Equivalently the NFW model adjusts during modelling the scale radius r_s to very small values $r_s \approx 0.2''$ in order to get a sufficiently steep mass distribution. The third profile, our preferred SL model, can easily accommodate the steep central mass distribution of galaxy G2 by choosing a relatively steep central slope of $\gamma = 0.93$ in Eq. (4.4). Since all three models have similar evidence values, we combine the slope measurements to estimate the systematic uncertainty in the slope measurement as a function of radius. This allowed range for the 2D mass density slope for galaxy G2 is shown as a shaded magenta area in Fig. 4.4. In the range where the mass and the integrated mass of all profiles is almost identical, from 0.5 to $5''$ ($\sim 0.4\theta_e$

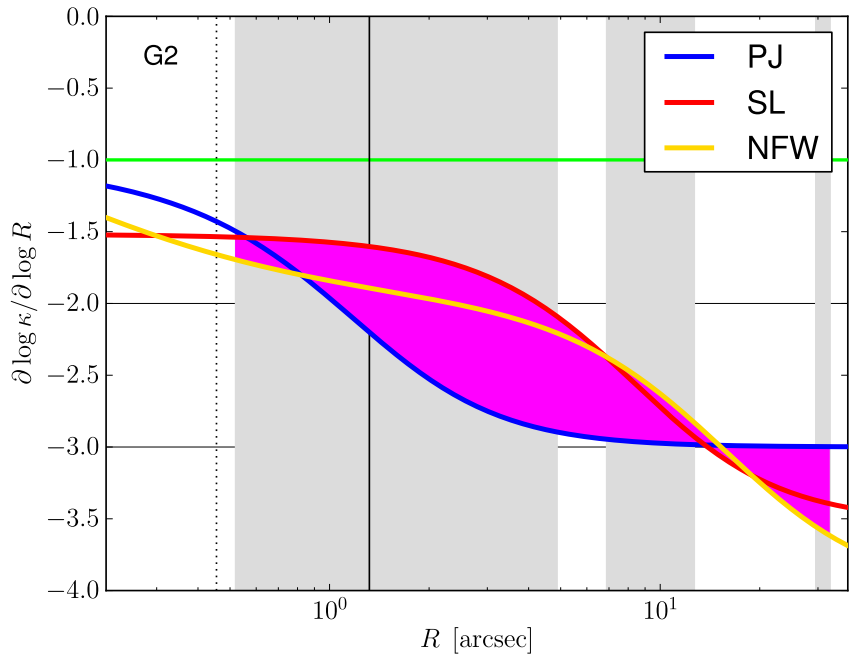

Figure 4.4: Logarithmic (2D) slope of the total modelled mass distribution of galaxy G2. Coloured lines are the slopes of the three analytical mass parametrizations, Pseudo-Jaffe (PJ), truncated power law with variable slope (SL) and NFW profile. Shaded pink area between the curves shows the conservative estimate for the allowed range of the slope due to the three equally well performing models. Grey shaded background indicates the radial regions that are constrained by multiple images, the vertical solid black line is the radius of the Einstein ring, the vertical dotted line is the effective radius of the galaxy G2. Green horizontal line indicates the slope of a projected isothermal mass distribution without truncation.

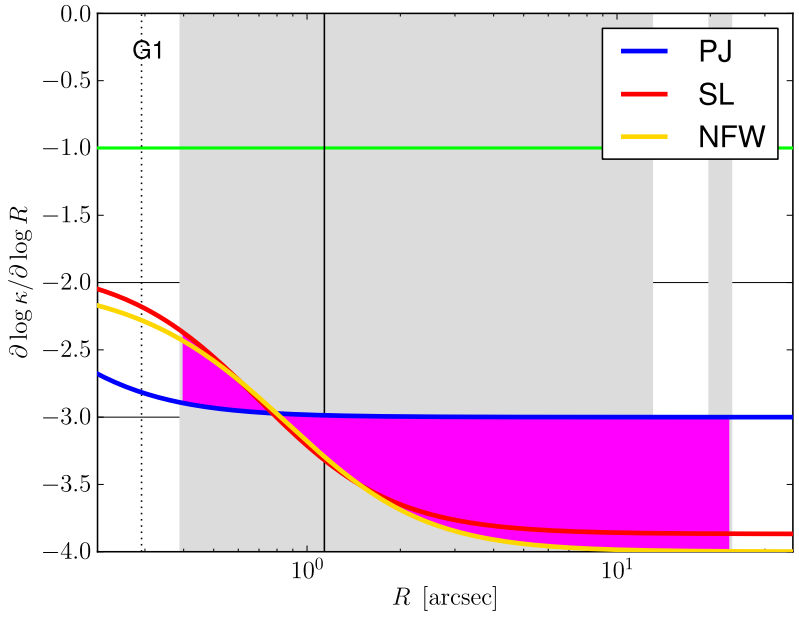

Figure 4.5: Same as Fig. 4.4 but for galaxy G1.

to $3.8\theta_e$), where θ_e is the Einstein radius, the logarithmic 2D slope steepens from $\gamma' \sim -1.5$ to $\gamma' \sim -2.5$. Independent of the substructure galaxy model, this is steeper than the previously measured values of $\gamma' \sim -1$ in field galaxies Koopmans et al. (2006); Sonnenfeld et al. (2013). This result is a strong indication for the truncation of the total mass distribution of the galaxy G2 in the dense environment of the galaxy cluster MACS J1149+2223.

We have seen in Sec. 4.4.2 that $\sim 95\%$ of the mass of galaxy G1 is contained within the Einstein radius, $r < 1.17''$ (7.7 kpc). This is also evident from the logarithmic projected slope of the mass distribution of G1 in Fig. 4.5. All three profiles have a slope $\gamma < -3$ at the Einstein radius. Since there are no constraints for radii smaller than $r < 0.4''$, there is no information on the mass distribution at the innermost radii. However, we know that the mass distribution has to be extremely steep ($\gamma' < -2.5$) at the radius of our first radial constraint ($r \sim 0.4''$) and we know the mass within that radius is $M(< 0.4'') \sim 6.6 \times 10^{10} \mathrm{M}_\odot$. The inferred mass distribution of galaxy G1 from this lensing reconstruction is therefore extremely truncated.

4.5 Conclusions

Due to the large multiply lensed images at the centre of the cluster MACS J1149+2223 the total mass distribution of two cluster galaxies, G1 and G2, can be accurately reconstructed. The two cluster galaxies additionally multiply lens bright source clumps of the large spiral source galaxy

of the triple main image system into two 'substructure Einstein rings'.

In this chapter, we extended the analysis of the mass reconstruction of the cluster MACS J1149+2223 in chapter 3 and compared different analytic galaxy parametrizations. We found an overall similar performance, however, for galaxy G2 the two profiles with one more parameter perform slightly better. We robustly measure the mass within the Einstein radius of galaxies G1 and G2, $M\,(<\theta_E) = 15.9 \pm 0.2$ and $7.3 \pm 0.02 \times 10^{10}\mathrm{M}_{\odot}$ respectively. The total masses of both galaxies $M_{\mathrm{tot}} = 34.6 \pm 5.2$ and 7.6 ± 0.12 are not as good constrained by the data. We quantify the extend of both galaxies in terms of the total slope of the galaxy mass distribution, and find that the slope for all three profiles is significantly steeper than compared to observed field galaxies. We find a total projected density slope of galaxy G2 at the Einstein radius of $\gamma' = -1.8$. As might be expected, the galaxy very close to the centre of cluster MACS J1149+2223, galaxy G1, is more truncated. In fact, galaxy G1 is very severely truncated with a slope of $\gamma' = -3.2$ and $> 95\%$ of the galaxy mass is contained within the Einstein radius.

4.6 Outlook

We found a similar performance of the three substructure models. This indicates that even though the analytic parametrization of the models is different, they are capable to approximate the 'true' solution within the sensitivity of our method. All three models feature an adaptive slope and therefore even were able to fit the extremely steep mass distribution of galaxy G1.

Future work will elaborate on the following points:

- There might be more suitable analytic parametrizations of the galaxy mass distribution. Since lensing is sensitive to the mass distribution, the slope and the integrated mass within a certain radius, one could choose the mass within two, three or even more different radii and a suitable interpolation in between to define the mass distribution. However, there are several challenges to overcome. It is necessary to choose suitable radii that are well constrained by the data, one has to find an interpolation in between those radii and a mass distribution at very large radii. One would have to show that the chosen radii do not influence the physical interpretation of the results. This method might enable us to gradually constrain the mass of the galaxies, constraining the general distribution first, and by adding more and more parameters, finally probing the limit of the data and the method.

- The mass distribution of galaxy G1 is *very* steep. Most of the mass is in the innermost region within the Einstein radius. Further investigations have to be done on the reliability of the stellar mass estimate and on the comparison of the compact mass distribution as inferred from the lensing reconstruction with the observable galaxy surface brightness distribution.

- The mass distribution of galaxy G1 might be even steeper than what is expected from simulations of subhalos at the centre of galaxy clusters. Therefore a more thorough comparison with results from numerical simulations is needed. Predictions from simulations

can be incorporated in the evidence calculation presented in chapter 4 by using priors on the concentration and the truncation of the NFW profile that are motivated by simulations. Comparing the evidence for a model with priors with the best model we found in this chapter then shows how probable such a strong truncation is.

- A similar analysis might be performed for other, smaller cluster galaxies for example G3 in Fig. 3.2.
- Improved observational data will become available in 2014/2015 with the HST Frontier Fields observations of MACS J1149+2223. With the improved image quality we are then able to apply our model to repeat the lensing reconstruction of the surface brightness, in order to analyse even smaller cluster substructures. However any increase in pixel number or the number of model parameters will challenge current computational resources.

Chapter 5

Summary and Conclusions

Comparing the predictions from numerical N-body simulations of cosmological structure formation with observations is a powerful test for the current cosmological $\Lambda\mathrm{CDM}$ model. In this thesis we focused on the simulation and the observational reconstruction of the strong gravitational lensing effect on galaxy cluster scales. High resolution lensing simulations are performed via the tracing of light rays through the mass distribution of the simulated N-body clusters. Simulations of the effects of the simulated subhalo population on gravitational lensing are limited by the resolution of the simulations. In N-body simulations, the mass distribution is inherently noisy due to the particle nature of the simulation. This particle noise mimics the effect of physical subhalos and introduces spurious effects. In the first part of this thesis, we focused on this particle noise and investigated the effect of the particle noise on different lensing quantities and quantify the limitations of N-body simulations in resolving the effect of physical subhalos through gravitational imaging. In the second part of this thesis we performed a high-resolution reconstruction of Hubble Space Telescope observations of the galaxy cluster MACS J1149+2223. The image configuration of the multiply lensed spiral source galaxy is unique in that the images are very large and they cover the centre of the cluster. These observational constraints allowed a detailed lensing reconstruction of the projected mass density of the cluster centre and of two cluster galaxies in particular.

5.1 Particle Noise in N-body Simulations of Gravitational Lensing

In Chapter 2 we quantified the effect of particle noise in N-body simulations of gravitational lensing. We presented a formalism based on the bootstrap method and gave analytic expressions to quantify the effects due to the Poissonian noise of the particles of a N-body simulation for the gravitational lensing properties. This is the first work that systematically investigates the effect of particle noise on the major lensing quantities such as the surface mass density, the deflection angles, the magnification and the lensed images and compares the particle noise to physical substructures in the simulation. We applied the technique to the high-resolution Phoenix N-body simulations by Gao et al. (2012) and found that the noise on the projected surface mass density is

of the order of a few (< 5) percent. Due to the nonlinearity of gravitational lensing equation, the effect on higher order lensing quantities is significantly amplified. We investigated the magnitude of the irregularities in the simulated critical lines where the magnification diverges. This is the physical relevant region where strongly magnified images are observed, the so called giant arcs. In order to properly quantify the noise on the only directly with observations comparable quantities, the simulated lensed images, we presented a Bayesian argument. We reconstructed the source surface brightness distribution in each step of the noise calculation in order to avoid including unobservable effects such as a shift of the source position in the noise.

In the second part of Chapter 2, we compared the noise on the different lensing quantities with the effect of small physical subhalos. For each of the lensing quantities we presented a resolution limit, where the effect of a substructure can no longer be resolved by the gravitational lensing simulations. For the Level-2 resolution of the Phoenix simulations, the highest resolution cluster simulations to-date, we found a minimum subhalo mass of $6 \times 10^9 \mathrm{M}_\odot$ consisting of $\sim 10^3$ particles. We found a dependence of the resolution limit on the structure of the source surface brightness distribution, where the Gaussian limit quoted above is a conservative estimate. Finally we presented analytical scaling relations for the required resolution of a N-body simulation in order to resolve subhalos of a particular size in gravitational lensing simulations.

5.2 Lensing Model of MACS J1149+2223 I: Cluster Reconstruction

In Chapter 3 we presented a mass reconstruction of the gravitational lensing cluster MACS J1149+2223. We focused on the accurate modelling of the central extended lensed images that cover a large fraction of the inner radial $20''$ $(\sim 130\ \mathrm{kpc})$. For a lensing reconstruction based on image positions, we newly identified twice the number of previously known constraints in the main image system. Those newly identified multiple imaged source clumps constrain in particular the innermost region of the cluster and the Einstein rings around two cluster galaxies. Due to the radially dependent ellipticity of the cluster mass distribution, we presented two mass models. Our best central model has a image plane uncertainty of the lensed multiple image positions of $\sigma = 0.07''$. For the first time we also presented a full surface brightness reconstruction of the main image system of MACS J1149+2223 with greatly reduced degeneracies between the mass parameters compared to the position based model. The full surface brightness reconstruction reproduces all of the morphological features of the lensed images with residuals comparable to the noise level of the Hubble Space Telescope observations. The central total logarithmic slope of the mass distribution is $\partial \log \rho / \partial \log r = -1.32$, this is consistent with previous observations. We found that the mass distribution of the central cluster galaxies is non-negligible for the total mass distribution and the measurement of the total slope. The inferred slope of the dark matter is shallower than what is found in purely dark matter simulations. The results therefore support the theory of a flattening of the central dark matter cusp due to baryonic processes such as feedback or dynamical heating during cluster formation.

5.3 Lensing Model of MACS J1149+2223 II: The Profiles of Cluster Galaxies

In Chaper 4 we extended the analysis of the mass distribution of MACS J1149+2223. We compared three different parametric galaxy models for two cluster galaxies through their Bayesian evidence values. The strongly lensed images in the main system of the cluster MACS J1149+2223 constrain the mass distribution of both galaxies out to large distances from the galaxy centre. The three galaxy models, a Pseudo-Jaffe model, a truncated NFW model and a truncated power law model with variable slope, were chosen to have finite total mass and a variable slope. The latter two profiles are more complicated with one additional parameter. All models perform equally well in reproducing the mass within the Einstein radius and the slope at the Einstein radius. For galaxy G2 we found a slight preference of the two more complicated models. For both galaxies, we found strong indications for the truncation of the galaxy mass distribution. The 2D logarithmic projected total slope of G2 at the Einstein radius is $\gamma'_{\rm tot,2D} = \partial \log \kappa / \partial \log R = -1.8$. The galaxy closer in projection to the cluster centre appears to be extremely truncated with a slope of $\gamma' = -3.2$ and almost all ($> 95\%$) of its mass is within the Einstein radius. Due to the large extended lensed images, we were able to robustly constrain the non-averaged slope of the mass distribution over a large range of scales for $0.4'' < r < 23.4''$ for galaxy G1 and from $0.5'' < r < 32.6''$ for galaxy G2.

5.4 Outlook

The modelling of the full surface brightness distribution of strong gravitationally lensed images is an important observational tool to constrain small-scale structure in galaxy clusters. Careful modelling has to be done for each cluster individually. Our new strong lensing mass model for MACS J1149+2223 provides a valuable starting point for future, more detailed investigations of the cluster mass distribution (see outlook in Sec. 4.6). Only one additional CLASH cluster has yet been reconstructed to a level comparable to the one presented in this work. Due to the scatter in the properties of individual objects, however, a large number of reliable mass reconstructions is needed. Additionally, the HST Frontier Fields will provide the deepest observations of galaxy clusters in the next two years and will be a challenge for any mass reconstruction method. The improved resolution will constrain the mass distribution of even smaller cluster galaxies to a level currently not possible from the CLASH observations. On the other hand, the inclusion of baryons in cosmological N-body simulations to date is also challenging. Ultimately, more detailed and statistical comparisons of observations with numerical simulations will then have to identify the important physical processes involved in shaping the central profile of clusters and galaxies.

Bibliography

Amara A., Metcalf R. B., Cox T. J., Ostriker J. P., 2006, MNRAS, 367, 1367

Amorisco N. C., Agnello A., Evans N. W., 2013, MNRAS, 429, L89

Aubert D., Amara A., Metcalf R. B., 2007, MNRAS, 376, 113

Baltz E. A., Marshall P., Oguri M., 2009, J. Cosmology Astropart. Phys., 1, 15

Barkana R., 1998, ApJ, 502, 531

Bartelmann M., 2003, ArXiv Astrophysics e-prints

Bartelmann M., Huss A., Colberg J. M., Jenkins A., Pearce F. R., 1998, A&A, 330, 1

Bayliss M. B., Gladders M. D., Oguri M., Hennawi J. F., Sharon K., Koester B. P., Dahle H., 2011, ApJ, 727, L26

Bell E. F., McIntosh D. H., Katz N., Weinberg M. D., 2003, ApJS, 149, 289

Belokurov V. et al., 2007, ApJ, 654, 897

Bradač M., Schneider P., Lombardi M., Steinmetz M., Koopmans L. V. E., Navarro J. F., 2004, A&A, 423, 797

Bradač M., Schneider P., Steinmetz M., Lombardi M., King L. J., Porcas R., 2002, A&A, 388, 373

Broadhurst T. et al., 2005, ApJ, 621, 53

Comerford J. M., Natarajan P., 2007, MNRAS, 379, 190

Dalal N., Kochanek C. S., 2002, ApJ, 572, 25

Diemand J., Kuhlen M., Madau P., 2007, ApJ, 667, 859

Diemand J., Moore B., Stadel J., 2004, MNRAS, 353, 624

Donnarumma A. et al., 2011, A&A, 528, A73

Ebeling H., Ma C. J., Kneib J.-P., Jullo E., Courtney N. J. D., Barrett E., Edge A. C., Le Borgne J.-F., 2009, MNRAS, 395, 1213

Eichner T. et al., 2013, ArXiv e-prints

Einasto J., 1965, Trudy Astrofizicheskogo Instituta Alma-Ata, 5, 87

El-Zant A., Shlosman I., Hoffman Y., 2001, ApJ, 560, 636

El-Zant A. A., Hoffman Y., Primack J., Combes F., Shlosman I., 2004, ApJ, 607, L75

Ettori S., Donnarumma A., Pointecouteau E., Reiprich T. H., Giodini S., Lovisari L., Schmidt R. W., 2013, Space Sci. Rev., 177, 119

Fadely R., Keeton C. R., 2012, MNRAS, 419, 936

Feroz F., Hobson M. P., 2008, MNRAS, 384, 449

Feroz F., Hobson M. P., Bridges M., 2009, MNRAS, 398, 1601

Feroz F., Hobson M. P., Cameron E., Pettitt A. N., 2013, ArXiv e-prints

Frenk C. S., White S. D. M., Efstathiou G., Davis M., 1985, Nature, 317, 595

Gao L., Navarro J. F., Frenk C. S., Jenkins A., Springel V., White S. D. M., 2012, MNRAS, 425, 2169

Gao L., White S. D. M., Jenkins A., Stoehr F., Springel V., 2004, MNRAS, 355, 819

Gaudi B. S., 2012, ARA&A, 50, 411

Gavazzi R., Treu T., Koopmans L. V. E., Bolton A. S., Moustakas L. A., Burles S., Marshall P. J., 2008, ApJ, 677, 1046

Ghigna S., Moore B., Governato F., Lake G., Quinn T., Stadel J., 1998, MNRAS, 300, 146

Gnedin O. Y., Kravtsov A. V., Klypin A. A., Nagai D., 2004, ApJ, 616, 16

Governato F. et al., 2012, MNRAS, 422, 1231

Halkola A., Seitz S., Pannella M., 2006, MNRAS, 372, 1425

Halkola A., Seitz S., Pannella M., 2007, ApJ, 656, 739

Heymans C. et al., 2012, MNRAS, 427, 146

Jullo E., Kneib J.-P., Limousin M., Elíasdóttir Á., Marshall P. J., Verdugo T., 2007, New Journal of Physics, 9, 447

Kaiser N., Squires G., 1993, ApJ, 404, 441

Kassiola A., Kovner I., 1993, ApJ, 417, 450

Kaufmann T., Wheeler C., Bullock J. S., 2007, MNRAS, 382, 1187

Klypin A., Kravtsov A. V., Valenzuela O., Prada F., 1999, ApJ, 522, 82

Kochanek C. S., Dalal N., 2004, ApJ, 610, 69

Koopmans L. V. E., 2005, MNRAS, 363, 1136

Koopmans L. V. E., Treu T., Bolton A. S., Burles S., Moustakas L. A., 2006, ApJ, 649, 599

Kravtsov A., 2010, Advances in Astronomy, 2010

Laporte C. F. P., White S. D. M., Naab T., Ruszkowski M., Springel V., 2012, MNRAS, 424, 747

Li G.-L., Mao S., Jing Y. P., Bartelmann M., Kang X., Meneghetti M., 2005, ApJ, 635, 795

Li G.-L., Mao S., Jing Y. P., Kang X., Bartelmann M., 2006, ApJ, 652, 43

Limousin M., Kneib J. P., Bardeau S., Natarajan P., Czoske O., Smail I., Ebeling H., Smith G. P., 2007, A&A, 461, 881

Limousin M., Sommer-Larsen J., Natarajan P., Milvang-Jensen B., 2009, ApJ, 696, 1771

Lombardi M., Schneider P., 2001, A&A, 373, 359

Lombardi M., Schneider P., 2002, A&A, 392, 1153

Lombardi M., Schneider P., 2003, A&A, 407, 385

Macciò A. V., Moore B., Stadel J., Diemand J., 2006, MNRAS, 366, 1529

Mao S., Schneider P., 1998, MNRAS, 295, 587

Marriage T. A. et al., 2011, ApJ, 737, 61

Martizzi D., Teyssier R., Moore B., 2013, MNRAS, 432, 1947

Meneghetti M., Fedeli C., Zitrin A., Bartelmann M., Broadhurst T., Gottlöber S., Moscardini L., Yepes G., 2011, A&A, 530, A17

Merritt D., 1983, ApJ, 264, 24

Merritt D., 1984, ApJ, 276, 26

Merritt D., 1985, ApJ, 289, 18

Merritt D., Graham A. W., Moore B., Diemand J., Terzić B., 2006, AJ, 132, 2685

Metcalf R. B., Zhao H., 2002, ApJ, 567, L5

Monaghan J. J., 1992, ARA&A, 30, 543

Natarajan P., Kneib J.-P., Smail I., 2002, ApJ, 580, L11

Natarajan P., Kneib J.-P., Smail I., Treu T., Ellis R., Moran S., Limousin M., Czoske O., 2009, ApJ, 693, 970

Natarajan P., Loeb A., Kneib J.-P., Smail I., 02b, ApJ, 580, L17

Navarro J. F., Frenk C. S., White S. D. M., 1997, ApJ, 490, 493

Navarro J. F. et al., 2010, MNRAS, 402, 21

Newman A. B., Treu T., Ellis R. S., Sand D. J., 13b, ApJ, 765, 25

Newman A. B., Treu T., Ellis R. S., Sand D. J., 2011, ApJ, 728, L39

Newman A. B., Treu T., Ellis R. S., Sand D. J., Nipoti C., Richard J., Jullo E., 2013, ApJ, 765, 24

Newman A. B., Treu T., Ellis R. S., Sand D. J., Richard J., Marshall P. J., Capak P., Miyazaki S., 2009, ApJ, 706, 1078

Oguri M., Bayliss M. B., Dahle H., Sharon K., Gladders M. D., Natarajan P., Hennawi J. F., Koester B. P., 2012, MNRAS, 420, 3213

Oguri M. et al., 2009, ApJ, 699, 1038

Okabe N., Takada M., Umetsu K., Futamase T., Smith G. P., 2010, PASJ, 62, 811

Onions J. et al., 2012, MNRAS, 423, 1200

Paczynski B., 1996, ARA&A, 34, 419

Peng C. Y., Ho L. C., Impey C. D., Rix H.-W., 2002, AJ, 124, 266

Petters A. O., Levine H., Wambsganss J., 2001, Singularity theory and gravitational lensing

Planck Collaboration et al., 2013, ArXiv e-prints

Pontzen A., Governato F., 2012, MNRAS, 421, 3464

Postman M. et al., 2012, ApJS, 199, 25

Rau S., Vegetti S., White S. D. M., 2013, MNRAS, 430, 2232

Reed D., Governato F., Verde L., Gardner J., Quinn T., Stadel J., Merritt D., Lake G., 2005, MNRAS, 357, 82

Richard J., Kneib J.-P., Limousin M., Edge A., Jullo E., 2010, MNRAS, 402, L44

Sand D. J., Treu T., Ellis R. S., 2002, ApJ, 574, L129

Sand D. J., Treu T., Ellis R. S., Smith G. P., Kneib J.-P., 2008, ApJ, 674, 711

Sand D. J., Treu T., Smith G. P., Ellis R. S., 2004, ApJ, 604, 88

Schaap W. E., van de Weygaert R., 2000, A&A, 363, L29

Schneider P., Ehlers J., Falco E. E., 1992, Gravitational Lenses

Schneider P., Weiss A., 1992, A&A, 260, 1

Sellwood J. A., McGaugh S. S., 2005, ApJ, 634, 70

Sereno M., Jetzer P., Lubini M., 2010, MNRAS, 403, 2077

Skilling J., 2004, in Fischer R., Preuss R., Toussaint U. V., eds, AIP Conf. Series Vol. 735, AIP Conf. Series. pp 395–405

Smith G. P. et al., 2009, ApJ, 707, L163

Sommer-Larsen J., Limousin M., 2010, MNRAS, 408, 1998

Sonnenfeld A., Treu T., Gavazzi R., Suyu S. H., Marshall P. J., Auger M. W., Nipoti C., 2013, ArXiv e-prints

Springel V., 2005, MNRAS, 364, 1105

Springel V. et al., 2008, MNRAS, 391, 1685

Springel V. et al., 2005, Nature, 435, 629

Springel V., White S. D. M., Tormen G., Kauffmann G., 2001, MNRAS, 328, 726

Suyu S. H., Halkola A., 2010, A&A, 524, A94

Suyu S. H., Marshall P. J., Hobson M. P., Blandford R. D., 2006, MNRAS, 371, 983

Umetsu K., Broadhurst T., Zitrin A., Medezinski E., Coe D., Postman M., 2011, ApJ, 738, 41

Umetsu K. et al., 2012, ApJ, 755, 56

Vegetti S., Koopmans L. V. E., 2009, MNRAS, 392, 945

Vegetti S., Koopmans L. V. E., Bolton A., Treu T., Gavazzi R., 2010, MNRAS, 408, 1969

Vegetti S., Lagattuta D. J., McKean J. P., Auger M. W., Fassnacht C. D., Koopmans L. V. E., 2012, Nature, 481, 341

von der Linden A. et al., 2012, ArXiv e-prints: 1208.0597

Walker M. G., Peñarrubia J., 2011, ApJ, 742, 20

Williamson R. et al., 2011, ApJ, 738, 139

Yuan T.-T., Kewley L. J., Swinbank A. M., Richard J., Livermore R. C., 2011, ApJ, 732, L14

Zheng W. et al., 2012, Nature, 489, 406

Zitrin A., Broadhurst T., 2009, ApJ, 703, L132

Zitrin A., Broadhurst T., Barkana R., Rephaeli Y., Benítez N., 2011, MNRAS, 410, 1939

Acknowledgements

I like to thank Simon White for the possibility to write this thesis at the Max Planck Institute for Astrophysics, for support and guidance during the the PhD. I like to thank Simona Vegetti for countless discussions, insight and guidance. I thank Stefan Hilbert for useful discussions on any lensing related topic and my colleagues Andrew Chung, Thomas Ertl, Tyrone Woods and Chervin Laporte. I thank my family for support and help and finally Lena for her kindness, for encouraging, helping and supporting me.

Erklärung

Hiermit versichere ich, dass ich die Arbeit selbständig vefasst und keine anderen als die angegebenen Quellen und Hilfsmittel benutzt habe.

München, den 25. November 2013